The First Galaxies in the Hubble Frontier Fields

Rachana Ajey Bhatawdekar



The University of Nottingham

UNITED KINGDOM · CHINA · MALAYSIA

Thesis submitted to The University of Nottingham
for the degree of Doctor of Philosophy, February 2019

"Our Universe is a sorry little affair unless it has in it something for every age to investigate."

– **Lucius Annaeus Seneca**

"Man must cling to the belief that the incomprehensible is comprehensible. Otherwise he would give up investigating."

– **Goethe, Maxims and reflections, 1829**

Supervisor:	Prof. Christopher J. Conselice
Examiners:	Prof. Omar Almaini
	Dr. Stephen Wilkins
Submitted:	26$^{\text{th}}$ February 2019
Examined:	8$^{\text{th}}$ April 2019
Resubmitted:	23$^{\text{rd}}$ May 2019

Contents

Abstract **4**

Published Work **6**

List of Figures **7**

List of Tables **14**

Acknowledgements **16**

1 Introduction **17**

1.1 Epoch of Reionization 17

1.2 High-redshift galaxies 19

1.3 Luminosity functions and Mass functions 23

1.4 Probing the Epoch of Reionization with lensing 27

1.5 Thesis Outline 30

2 Data and methods **32**

2.1 Introduction 32

2.1.1 Hubble Frontier Fields 33

2.2 The Data 35

2.2.1 HST data 35

2.2.2 VLT data 35

2.2.3 Spitzer data 36

2.3 Methods 38

2.3.1 Divide and conquer 38

2.3.2 Subtraction of brightest cluster galaxies 40

2.3.2.1 Creating postage stamps and obtaining initial guess of model parameters 40

2.3.2.2 Modelling brightest cluster galaxies using GALFIT 40

2.3.2.3 Subtracting models from the original image 44

2.3.3 Multiwavelength photometry 46

2.3.3.1 HST images 46

2.3.3.2 K_s band and Spitzer images . . . 49
2.3.4 Photometric redshifts and source selection . . . 53
2.3.4.1 Photometric redshifts . . . 53
2.3.4.2 Sample selection criteria . . . 55
2.3.4.3 Comparison of $8.5 \leq z \leq 9.5$ sample with previous work . . . 58
2.3.5 Completeness simulations . . . 60
2.3.5.1 Detection completeness . . . 61
2.3.5.2 Selection function . . . 62
2.3.6 Stellar masses, rest-frame magnitudes and star formation rates 66
2.3.6.1 Stellar masses and rest-frame magnitudes . . . 66
2.3.6.2 Star formation rates . . . 67
2.3.7 Lensing magnification . . . 68
2.3.8 Number densities . . . 69
2.3.8.1 Effective volume estimation . . . 69
2.3.8.2 Errors on number densities . . . 70
2.4 Summary . . . 71

3 Evolution of the UV LF and GSMF 73
3.1 Introduction . . . 73
3.2 Ultra-Violet luminosity function . . . 76
3.2.1 Best fit Schechter parameters and their uncertainties for the UV LF . . . 76
3.2.2 Comparison with previous work . . . 82
3.2.3 Comparison with theoretical predictions . . . 83
3.3 Galaxy stellar mass function . . . 86
3.3.1 Best fit Schechter parameters and their uncertainties for the GSMF . . . 86
3.3.2 Comparison with previous work . . . 94
3.3.3 Comparison with theoretical predictions . . . 95
3.4 $M_* - M_{UV}$ relation . . . 98
3.5 Stellar mass density . . . 101
3.6 Specific star formation rates . . . 104
3.7 UV luminosity density . . . 106
3.8 Summary . . . 108

4 Evolution of the Galaxy Rest-frame UV Colours 110
4.1 Introduction . . . 110

4.2 Method 112
4.2.1 Estimating β 112
4.2.2 Testing the method 116
4.3 Results 118
4.3.1 Correlation of β with M_{1500} 118
4.3.2 Evolution of β with redshift 118
4.3.3 β of faint galaxies 120
4.3.4 Correlation of β with stellar mass 120
4.3.5 Correlation of β with SFR 125
4.3.6 Physical interpretation of β 128
4.4 Summary 130

5 Conclusions and Future Work **132**
5.1 Exploring high redshift galaxies 132
5.2 Evolution of the GSMF and UV LF 133
5.3 Evolution of the rest-frame UV colours 134
5.4 Future work 135

A Catalogs **138**

Bibliography **141**

Abstract

In this thesis we have exploited the power of gravitational lensing of massive clusters to probe galaxy evolution with the galaxy stellar mass functions (GSMF) and UV luminosity functions (UV LF) at $z = 6 - 9$. Throughout the thesis the data utilized is from the Hubble Frontier Fields (HFF) program.

We present new measurements of the evolution of the GSMF and UV LF for galaxies from $z = 6 - 9$ within the HFF cluster MACSJ0416.1-2403 and its parallel field. To obtain these results, we have developed a novel method to subtract the massive foreground galaxies that lie close to the critical line from the MACSJ0416.1-2403 cluster, allowing for a deeper and cleaner detection of the faintest systems at $z \geq 6$.

We derive the stellar masses of our sample by fitting synthetic stellar population models to their observed spectral energy distribution (SED) with the inclusion of nebular emission lines. This is the deepest and most distant mass function measured to date and probes down to a level of $\mathrm{M}_* = 10^{6.8} M_\odot$. The main result of this study is that the low-mass end of our stellar mass functions to these limits and redshifts are measured to be $\alpha = -1.98^{+0.07}_{-0.07}$ at $z = 6$ and $\alpha = -2.38^{+0.72}_{-0.88}$ at $z = 9$ and we find no evidence of any turnover in the mass range probed. The faint end slope of the UV LF for these system are also measured to be $\alpha = -2.03^{+0.12}_{-0.10}$ at $z = 6$ and $\alpha = -2.20^{+0.51}_{-0.47}$ at $z = 9$, without any evidence of a turnover in the luminosity range probed. Our $M_{\mathrm{UV}} - M_*$ relation exhibit shallower slopes than previously observed and are in accordance with a constant mass-to-light ratio.

Integrating our GSMF, we find that the stellar mass density increases from $\log_{10}\rho_* = 5.61^{+0.92}_{-0.90}\ \mathrm{M}_\odot\mathrm{Mpc}^{-3}$ at $z = 9$ to $\log_{10}\rho_* = 6.79^{+0.13}_{-0.12}\ \mathrm{M}_\odot\mathrm{Mpc}^{-3}$ at $z = 6$. We also find that there is a surprisingly high amount of stellar mass density for galaxies in the early universe up to $z \sim 9$. We estimate the dust-corrected star formation rates (SFRs) to calculate the specific star formation rates ($\mathrm{sSFR} = \mathrm{SFR}/\mathrm{M}_*$) of our sample, and find that for a fixed stellar mass of $5 \times 10^9 M_\odot$, $\mathrm{sSFR} \propto (1+z)^{2.01 \pm 0.16}$. From our new measurements, we also estimate the UV luminosity density (ρ_{UV}) and find that our results support a smooth decline of ρ_{UV} towards high redshifts.

Finally, we use the same dataset to investigate the evolution of the galaxy rest-frame UV colours (UV spectral slope β) for our sample of high redshift galaxies at $z = 6 - 9$. We measure the UV spectral slope β by fitting the observed spectral energy distribution to a set of synthetic stellar population models and estimate the value of β from the best-fit model spectrum. With this method, we find no correlation between β and rest-frame UV magnitude M_{1500} at all redshifts probed in this work. However, a possible weak evolution of the median β values (from $\beta = -2.24$ at $z \sim 6$ to $\beta = -2.52$ at $z \sim 9$) for galaxies at all luminosities from $z = 6 - 9$ is observed, likely due to increased dust extinction.

Furthermore, we find that at $z = 7$, the bluest value of our sample is $\beta = -2.31 \pm 0.31$, which is redder than previously reported values at this redshift in the literature. Similarly, with the help of our SED fitting method, we determine the UV slopes for the first time at $z \sim 9$ and find that our bluest data point has a value of $\beta = -2.63 \pm 0.21$, indicating no evidence as yet for extreme stellar populations at $z > 6$.

Examining the β to stellar mass relation, we find a strong correlation between β with stellar mass, in that lower mass galaxies exhibit bluer UV slopes. We also find that low mass galaxies at $\log M/M_{\odot} < 9$ appear to become bluer with increasing redshift, whereas the massive galaxies at $\log M/M_{\odot} > 9$ appear to exhibit a nearly constant β at each redshift. We also investigate, for the first time, the correlation between β and SFR and find that there is a strong correlation between β and SFR, in that galaxies with low SFRs exhibit bluer slopes, and they also appear to get bluer with increasing redshift.

Published Work

The vast majority of the work presented in this thesis is carried out by the author and has been presented in the following publications:

I **Rachana Bhatawdekar**., Christopher J. Conselice., Berta Margalef-Bentabol., Kenneth Duncan., 2018 "*Evolution of the galaxy stellar mass functions and UV luminosity functions at* $z = 6-9$ *in the Hubble Frontier Fields*", Monthly Notices of the Royal Astronomical Society, Volume 486, Issue 3, p.3805-3830.

II **Rachana Bhatawdekar**., Christopher J. Conselice., "*Evolution of the galaxy rest-frame UV colours at* $z = 6-9$ *in the Hubble Frontier Fields*", In preparation.

Paper I and Paper II both utilize the observations, data and methods discussed in Chapter 2. Paper I contains the work described in Chapter 2 and Chapter 3. Paper II is currently in preparation and contains the work discussed in Chapter 4.

List of Figures

1.1 The timeline showing the evolution of the Universe, from the Big Bang to the present day.(Credit: NAOJ.) 18

1.2 Discovery of Gunn-Peterson trough in a $z = 6.28$ quasar. The absence of the trough in quasars at redshifts $z = 5.80$, $z = 5.82$ and $z = 5.99$ demonstrated strong evidence for the completion of reionization around $z = 6$. Figure from Becker *et al.* (2001). 20

1.3 An example of a redshifted spectral energy distribution (SED) from a galaxy at $z \simeq 7$. A sharp drop in the spectrum is seen at 1216 Angstrom due to the Gunn-Peterson absorption.(Credit: S. Rogers.) 21

1.4 Rest-frame UV LF at $z \sim 8$ from Finkelstein *et al.* (2015). The solid red line shows their best-fitting Schechter function, with the best-fit values given by the inset text, revealing a steep faint-end slope that indicates a significant contribution from faint galaxies. 25

1.5 The GSMF at $z \sim 8$ from Song *et al.* (2016). The solid red line shows their best-fitting Schechter function, with the best-fit values given by the inset text, revealing a steep low mass end slope. 26

1.6 Massive objects such as galaxy clusters distort the space around them in such a way that the light from sources behind them is magnified. This gravitational lensing effect can result in magnifications of up to a factor of $\sim 100\times$, allowing us to directly observe the faintest galaxies beyond *HST*'s limit. (Credit: ALMA (ESO/NRAO/NAOJ), L. Calada (ESO), Y. Hezaveh et al.) 29

2.1 Names and locations of the six Frontier Fields cluster + parallel field pairs. Also shown are HDF-N, HDF-S, UDF, COSMOS, EGS, and UDS fields for reference (Figure from Lotz *et al.* (2017)). 34

2.2 F160W image of MACSJ0416 cluster. The critical line at $z = 7$ from the CATS model (Jauzac *et al.*, 2014) is shown in cyan. 39

2.3 Illustration of our divide and conquer method 43

2.4 Results of our subtraction procedure on the MACSJ0416 cluster . . 45

2.5 Photometric errors from SExtractor with photometry on the H-band image, dispersion of the difference between recovered magnitudes and input magnitudes with simulations, and photometric errors from SExtractor with the corrected rms map in bins of $\Delta m = 0.5$. 47
2.6 Comparison of detections in the original H-band image and the subtracted H-band image for the MACSJ0416 cluster 48
2.7 Results of our simulations, showing the mean difference between the input magnitude and recovered MAG_AUTO magnitude as a function of input magnitude in bins of $\Delta m = 0.5$. 50
2.8 IRAC 3.4 μm and 4.5 μm imaging of the MACSJ0416 cluster 51
2.9 Covariance index c_i as a function of measured fluxes from T-PHOT for the MACSJ0416 cluster 54
2.10 MACSJ0416 cluster and parallel field detections 57
2.11 Photometric redshift and spectroscopic redshift comparison for the MACSJ0416 cluster 59
2.12 Recovery fraction as a function of H-band input magnitude for unresolved point-like (blue and red dashed lines for cluster and field respectively) and disc-like sources (solid blue and solid red line for cluster and field respectively) in the MACSJ0416 cluster and the parallel field. 63
2.13 Selection efficiencies for the MACSJ0416 cluster, showing recovery fraction as a function of redshift and input magnitude. The solid line is for objects with $H_{160} = 25$ and the dashed line is for $H_{160} = 27$, finding very similar results. 65

3.1 The UV LF at $z = 6 - 9$ in the MACSJ0416 cluster and its parallel field. The solid green line is our best fit Schechter function derived from the MCMC analysis to the green circles, using disc-like galaxies in completeness simulations. The dashed green line is our best fit Schechter function from the MCMC analysis to the open green circles, using point sources. The error bars on our data points take into account the errors on photometric redshifts, errors on magnitudes, Poisson errors and uncertainties due to lensing maps, but does not include the errors due to cosmic variance. The representative error bar in the bottom right corner of each plot shows the measured error on number densities for galaxies of $M_{UV} \approx -19$ due to cosmic variance. 80

3.2 The UV LF at $z = 6 - 9$ in the MACSJ0416 cluster and its parallel field estimated using the lensing models of CATS, Sharon, Bradac and Merten using disc-like galaxies in completeness simulations. There is scatter between the different LFs, which is a result of different magnification factors estimated from the lensing models. But in all the cases a steeply increasing faint-end slope is observed without any evidence of a turn over. The solid green line is our best fit Schechter function to our fiducial luminosity function estimated from MCMC analysis using the median magnification factor, with disc-like galaxies in completeness simulations. The error bars on our data points take into account the errors on photometric redshifts, errors on magnitudes and Poisson errors. 81

3.3 Comparison of the observed UV LF at $z = 6 - 9$ in the MACSJ0416 cluster and its parallel field estimated using disc-like galaxies and point sources in completeness simulations with theoretical predictions. We show the results from the cosmological hydrodyamics simulations of the IllustrisTNG project (Vogelsberger *et al.*, 2019), FirstLight project (Ceverino, Glover & Klessen, 2017), CROC project (Gnedin, 2016) and the simulations results from Finlator, Oppenheimer & Davé (2011). 85

3.4 Distribution of 100 random samples drawn from the chain at $z \sim 6$ from our MCMC analysis and projected into the space of the observed data. 87

3.5 Corner plots showing the two dimensional posterior probability distributions of characteristic stellar mass M^* and faint end slope α at $z = 6, 7$ and 8 with contours shown at 0.5, 1, 1.5, and 2 sigma. Top left: Posterior probability distribution at $z \sim 6$. Top right: Posterior probability distribution at $z \sim 7$. Bottom: Posterior probability distribution at $z \sim 8$. The marginalized distribution for each parameter is shown independently in the histograms, with the dashed line being the median value of the distribution. 88

3.6 The GSMF at $z = 6 - 9$ in the MACSJ0416 cluster and its parallel field. The solid green line is our best fit Schechter function from our MCMC analysis to the green circles, considering disc-like galaxies in completeness simulations. The dashed green line is our best fit Schechter function from MCMC analysis to the open green circles, using point sources. The error bars on our data points take into account errors on photometric redshifts, errors on stellar mass, Poisson errors and uncertainties due to lensing maps, but does not include errors due to cosmic variance. The representative error bar in the bottom left corner of each plot shows the measured error on number densities for galaxies of $10^{8.5}M_{\odot}$ due to cosmic variance. 90

3.7 The GSMF at $z = 6 - 9$ in the MACSJ0416 cluster and its parallel field estimated using the lensing models of CATS, Sharon, Bradac and Merten using disc-like galaxies in completeness simulations. There is scatter between the different MFs, which is a result of different magnification factors estimated from the lensing models. But in all the cases a steeply increasing low-mass end slope is observed without any evidence of a turn over. The solid green line is our best fit Schechter function to our fiducial mass function estimated from MCMC analysis using the median magnification factor, with disc-like galaxies in completeness simulations. The error bars on our data points take into account the errors on photometric redshifts, errors on magnitudes and Poisson errors. 91

3.8 Redshift evolution of best fit Schechter function parameters for our stellar mass functions. The solid orange circles represent the best fit Schechter parameters considering disc-like galaxies in our completeness simulations, whereas the open circles are our results considering point sources. The low mass end slope α steepens with increasing redshift, number density Φ^* decreases with increasing redshift, whereas no evolution in the characteristic mass M^* is observed. **Note:** The error bars on characteristic mass M^* at $z \sim 9$ are not shown since we keep the value of M^* fix to the value estimated at $z \sim 8$. 93

3.9 Comparison of the observed GSMF at $z = 6 - 8$ in the MACSJ0416 cluster and its parallel field estimated using disc-like galaxies and point sources in completeness simulations with theoretical predictions. We show the results from the SAMs of Croton, Somerville and Lu with stellar mass uncertainties convolved as described in Lu *et al.* (2014), along with the results from cosmological hydrodyamics simulations of Illustris project, FirstLight project, Choi & Nagamine (2012) and Dayal *et al.* (2014). 97

3.10 Stellar mass as a function of rest-frame absolute UV magnitude at 1500 Angstrom at $z = 6 - 9$. Grey filled circles represent sources with a S/N ratio $> 3\sigma$ at $3.6\mu m$ in IRAC, whereas grey open circles are those with a S/N ratio $\leq 3\sigma$. Filled yellow circles represent the median stellar masses in each rest-frame absolute UV magnitude bin of 0.5 mag, and the yellow error bars represent the standard deviation in stellar mass in each UV magnitude bin. The best-fit $\log_{10}(\mathrm{M}_*/\mathrm{M}\odot) - \mathrm{M}_{\mathrm{UV}}$ relation is shown by solid yellow line in each redshift bin. The best-fit $\log_{10}(\mathrm{M}_*/\mathrm{M}\odot) - \mathrm{M}_{\mathrm{UV}}$ lines of González *et al.* (2011), Stark *et al.* (2013), Duncan *et al.* (2014) and Song *et al.* (2016) are also shown by green, blue, red and magenta dashed lines, respectively, for comparison. 100

3.11 Evolution of total SMD as a function of redshift. We calculate the total SMD by integrating the best fit Schechter function from $M_* = 10^8$ to $10^{13} M_\odot$ for our GSMFs. The quoted 1σ error bars represent the minimum and maximum range of stellar mass densities within the 1σ contours of Schechter parameters obtained from our MCMC analysis. Our results are shown as solid orange points when disc-like galaxies are considered in our completeness simulations, and as open grey circles considering point sources. Shown also are the values from the literature converted to a Chabrier IMF, where necessary. . . . 105

3.12 Biweight mean sSFR and error on the mean for galaxies in a fixed stellar mass bin of $\log_{10}(M/M_\odot) = 9.7 \pm 0.3$ as a function of redshift. The dashed yellow line is the best-fitting power law to the observed values of sSFR from $z \sim 6 - 9$. The theoretical model of Dekel *et al.* (2013) in which the specific accretion rate follows the form sSFR $\propto (1 + z)^{2.5}$ is shown by dashed grey line. 106

3.13 Evolution of UV luminosity density as a function of redshift. $\rho_{\rm UV}$ values calculated with a $M_{\rm UV} = -13.5$ limit are shown in orange filled circles and $\rho_{\rm UV}$ calculated using a $M_{\rm UV} = -17$ limit are shown in orange filled triangles. Also shown are the $\rho_{\rm UV}$ estimates considering point sources in our completeness simulations with open grey circles and open grey triangles for $M_{\rm UV} = -13.5$ and $M_{\rm UV} = -17$ respectively. The dashed yellow line is the power-law fit to the data points at $z \sim 6 - 9$, such that $\rho_{\rm UV} \propto (1+z)^{-2.63}$. Fitting a power-law at $z \geq 8$ values results in $\rho_{\rm UV} \propto (1+z)^{-4.61}$ (not shown). 107

4.1 The estimated UV slope β vs absolute magnitude at 1500 Angstrom at $z = 6 - 9$. The filled yellow circles show the results for individual galaxies, whereas the black circles show the median value of β measured in three different bins separated by the dashed lines, denoting the evolving values of 0.25 L^* and 0.75 L^*, similar to Finkelstein *et al.* (2012), with the uncertainties being the errors on the median. 114

4.2 Results of our simulations at $z = 6 - 9$, showing the difference between the input value of the UV spectral slope β and that recovered from SED fitting as a function of input H_{160} magnitude. The orange circles represent the mean difference between simulated and observed values of β as well as the scatter in bins of $\Delta m = 1$. 117

4.3 The evolution of the median β of all galaxies in each redshift bin, shown in yellow circles. The median M_{1500} for these points are -17.95, -18.53, -18.77, and -19.44 at $z = 6$, $z = 7$, $z = 8$, and $z = 9$ respectively. Shown also are the results from the literature interpolated to represent the results at the median value of M_{1500} for our sample. The dashed yellow shows a linear fit through the median β points. A weak evolution in β from $z = 9$ to $z = 6$ is observed, presumably due to increased dust extinction. 119

4.4 Estimated UV slope β vs stellar mass at $z = 6 - 9$. The filled yellow circles show the results for individual galaxies, whereas the black circles show the median value of β in each stellar mass bin of $1 M_{\odot}$. The solid red lines shows a linear fit through the median β points. There is a strong correlation between β and stellar mass in all redshift bins, in that lower mass galaxies exhibit bluer UV slopes. The best-fit lines of Finkelstein *et al.* (2012) are also shown by dashed magenta lines for comparison. 122

4.5 Evolution of median value of UV spectral slope β in different mass bins with redshift. The red circle shows the median β in mass bin $6 < \log M/M_\odot < 7$, green circles show the median β in mass bin $7 < \log M/M_\odot < 8$, blue circles show the median β in mass bin $8 < \log M/M_\odot < 9$, yellow circles show the median β in mass bin $9 < \log M/M_\odot < 10$ and finally the magenta circle shows the median β in mass bin $10 < \log M/M_\odot < 11$. It appears that low mass galaxies at $\log M/M_\odot < 9$ become bluer with increasing redshift, whereas the massive galaxies at $\log M/M_\odot > 9$ appear to exhibit a nearly constant β at each redshift. 124

4.6 Estimated UV slope β vs SFR at $z = 6 - 9$. The filled yellow circles show the results for individual galaxies, whereas the black circles show the median value of β in each SFR bin of $1\mathrm{M}_\odot\mathrm{yr}^{-1}$. The solid red lines show a linear fit through the median β points. There is a strong correlation between β and SFR, in that galaxies with low SFRs exhibit bluer slopes. 126

4.7 Evolution of median value of UV spectral slope β in different SFR bins with redshift. The red circle shows the median β in SFR bin $-2.0 < \log \mathrm{SFR} < -1.5$, green circles show the median β in SFR bin $-1.5 < \log \mathrm{SFR} < -1.0$, blue circles show the median β in SFR bin $-1.0 < \log \mathrm{SFR} < 0.0$, yellow circles show the median β in SFR bin $0.0 < \log \mathrm{SFR} < 0.5$ and finally the magenta circle shows the median β in SFR bin $0.5 < \log \mathrm{SFR} < 1.5$. It appears that galaxies with low SFRs are bluer and they tend to get bluer with increasing redshift. 128

List of Tables

2.1 Description of dataset for the MACSJ0416 cluster and its parallel field 37

3.1 Best fit Schechter function parameters and their uncertainties for our UV LFs. The quoted best fit values and 1σ errors of the Schechter parameters constitute the median and the central 68 per cent of posterior distribution of each parameter from our MCMC analysis. **Note**: We only show the Schechter function parameters and their uncertainties derived using a classical Schechter function fit for Atek *et al.* (2018) and Bouwens *et al.* (2017b) and do not show the values they derive with a modified Schechter function that allows for a curvature at very faint magnitudes. 79

3.2 Best fit Schechter function parameters and their uncertainties for our GSMFs. The quoted best fit values and 1σ errors of the Schechter parameters constitute the median and the central 68 per cent of posterior distribution of each parameter from our MCMC analysis. . . 89

3.3 Best-fit $\log_{10}(\mathrm{M}_*/\mathrm{M}\odot) - \mathrm{M}_{\mathrm{UV}}$ relation. The values in parentheses are the best-fit values when we restrict our analysis to brighter magnitudes ($\mathrm{M}_{\mathrm{UV}} \leq -16$). The quoted errors represent the 1σ uncertainties. 101

3.4 Total stellar mass density estimates by integrating the best fit Schechter function from $M_* = 10^8$ to $10^{13} M_\odot$ for our GSMFs. The quoted 1σ error bars represent the minimum and maximum range of stellar mass densities within the 1σ contours of Schechter parameters obtained from our MCMC analysis. Also shown in the table are values of ρ_{UV} and ρ_{SFR}. The ρ_{UV} values are integrated down to $M_{\mathrm{UV}} = -13.5$, the magnitude of the faintest galaxy in our sample. The SFR densities are calculated using the (Kennicutt, 1998) relation, assuming a Salpeter IMF and a constant SFH over $\geq$100 Myr. The values in the parentheses are computed using point sources in our completeness simulations. 103

4.1 Median values of the UV spectral slope β 115
4.2 Median values of the UV spectral slope β in different mass bins. . . 123
4.3 Median values of the UV spectral slope β in different SFR bins. . . 127

A.1 Catalog of the $z \sim 8$ sample. Column (1) lists the source IDs, column (2) and (3) lists their coordinates, column (4) gives the photometric redshift, column (5) lists the median magnification, column (6) is the absolute magnitude at 1500 angstrom and column (7) is the logarithm of the stellar mass. Both absolute magnitude and stellar mass values are corrected for magnification. 139
A.2 Catalog of the $z \sim 9$ sample. Column (1) lists the source IDs, column (2) and (3) lists their coordinates, column (4) gives the photometric redshift, column (5) lists the median magnification, column (6) is the absolute magnitude at 1500 angstrom and column (7) is the logarithm of the stellar mass. Both absolute magnitude and stellar mass values are corrected for magnification. 140

Acknowledgements

First and foremost, I would like to thank my supervisor Chris Conselice for not only giving me the opportunity to work on this amazing project but also showing the confidence that someone like me, from an Engineering and software development background, could actually bring it to fruition. Without your guidance, advise and enduring support, this dissertation would have been inconceivable.

I am also indebted to many other people who helped me survive my PhD. Special thanks goes to Berta and Dongyao for being patient with my innumerable queries and for the many insightful discussions and suggestions, Charutha and Miguel for all the encouragement and reassurance when things went rough, Ulli for being such a massive support to me these past couple of years and Fahad for just being you! I am also grateful to my officemates and friends: Amelia, Rachel, Tom, Sunny, Lizzie, Julian, Emily and Nan for making our office such a fun and pleasant environment to work. Thank you Carl and KK for checking on me every now and then to make sure I was doing all right even after you left the department. I am blessed to have friends like you in my life. I was also fortunate to meet and work closely with people like Ken, Rachael and Derek. From you guys I learned what distinguishes a great research from a good research and what an independent research truly means.

I must also express my gratitude towards my parents, in-laws and members of my extended family who always supported my decisions and understood why this was important to me. Finally, and most importantly, I cant thank enough my husband Saurabh for supporting me with my decision of switching fields, from IT industry to astronomy, to pursue my childhood dream. This would not have been possible without your understanding and love.

Thank you all, what an incredible journey this has been!

This thesis is dedicated to my parents.

Chapter 1

Introduction

1.1 Epoch of Reionization

The human quest to comprehend the Universe, to understand what's out there, how it began, and how it will all eventually end can be dated back to 3000–3500BC. Starting with naked eye observations, astronomy has made a remarkable progress since the advent of modern telescopes such as the Hubble Space Telescope (HST).

We now know that the Universe began with the Big Bang 13.8 billion years ago as an unimaginably hot and dense place. This was so hot that even atoms could not form. As the Universe expanded, roughly 380,000 years after the Big Bang, the matter cooled and condensed to form neutral atoms predominantly of hydrogen and the Universe became electrically neutral – a phase called as recombination. This allowed the remnant heat from the Big Bang, the Cosmic Microwave Background (CMB) radiation, to propagate freely throughout the Universe. What followed this epoch was the "Dark Ages" of the Universe, lasting for several hundred million years; as there was no other source of light, the stars had not been born yet. Slowly, gravitational collapse of the overdense regions led to the formation of the first stars and first galaxies and the Ultraviolet (UV) light from these very first luminous sources ionized the intergalactic medium – a period referred to as the Epoch of Reionization (EoR), starting at $z \sim 20$ and ending at $z \sim 6$. Fig. 1.1 illustrates this timeline showing the evolution of the Universe.

As the first sources formed in the densest regions, the UV light from star formation in these sources caused a rapid increase in the ionized fraction of the gas in the Universe until the neutral hydrogen became fully ionized. This era of the Epoch of Reionization, during which the gas in the intergalactic medium went from neutral to ionized, was the last major phase change in the Universe's history and represents the frontier of studies of galaxy evolution. To ionize hydrogen and maintain the

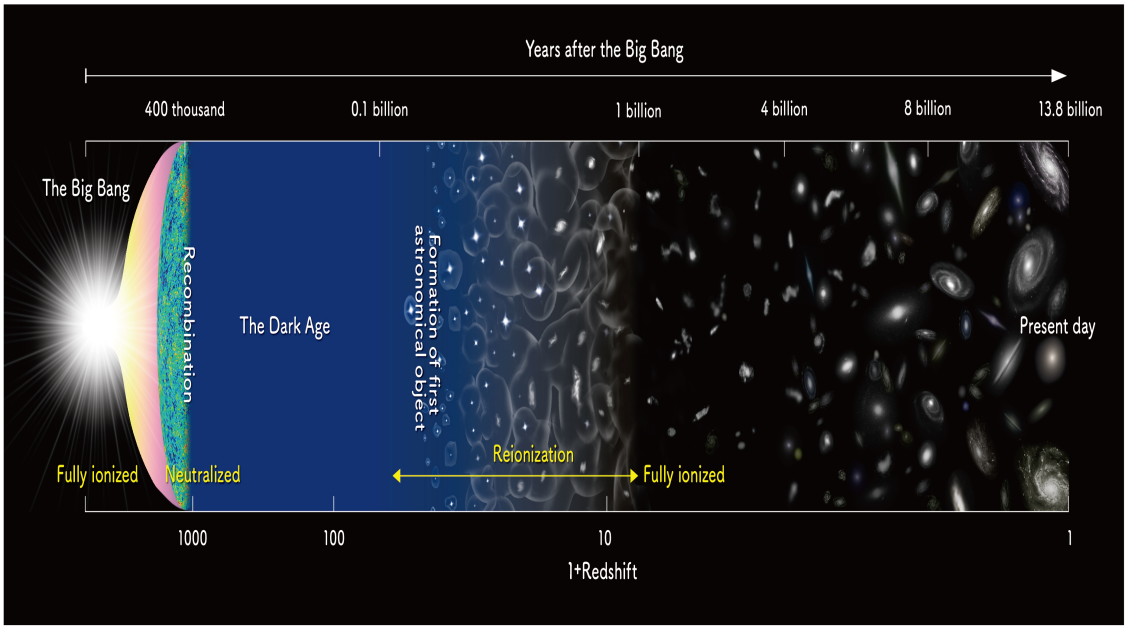


Figure 1.1: The timeline showing the evolution of the Universe, from the Big Bang to the present day.(Credit: NAOJ.)

reionization state of the Universe, objects need to provide UV photons with energy ≥ 13 eV. So a crucial question is what were the first energetic sources responsible for such a dramatic phase transformation? Could it be galaxies, quasars or population III stars? Understanding the formation of the very first luminous sources that reionized the early Universe remains one of the major unanswered questions in contemporary astronomy. There are a few observational methods to study reionization such as through the Lyman-α forest and the Gunn-Peterson trough, CMB anisotropy and polarization, as well as other energy sources namely dwarf galaxies, active galactic nuclei (AGN) and population III stars, which also provide the evidence for the occurrence of cosmic reionization.

For the hydrogen atom, electron transition between $n = 2 \rightarrow n = 1$ energy levels corresponds to Lyman-α line with a wavelength of 1216 Angstrom. In the otherwise continuous spectra of distant galaxies and quasars, the absorption of UV photons by the intervening neutral hydrogen clouds along the line of sight causes a spectral discontinuity at the Lyman-α line. As these hydrogen clouds are at different distances (and hence redshift), this leads to the formation of a series of absorption lines at a range of wavelengths called as the Lyman-α forest. With increasing redshift, the Lyman-α forest becomes denser such that at $z \sim 6$ the Lyman-α forest is so intense that it suppresses all of the electromagnetic radiation shortward of the Lyman-α line. This effect is known as the Gunn-Peterson trough. In 2001, the discovery of Gunn-Peterson trough in a $z = 6.28$ quasar (Becker *et al.*,

2001), and the absence of the trough in quasars at redshifts $z = 5.80$, $z = 5.82$ and $z = 5.99$ demonstrated strong evidence for the completion of reionization around $z = 6$ (See Fig. 1.2).

Another evidence for reionization is provided by the CMB anisotropies. The CMB photons are scattered off free electrons associated with reionization due to Thomson scattering. This results in a bump on the CMB polarization power spectrum. The Wilkinson Microwave Anisotropy Probe (WMAP) examined the anisotropies and compared it with how they would be like in the absence of the reionization event, allowing to calculate the redshift of reionization. The three year WMAP data suggested that reionization started at $z = 11$, ending by $z = 7$ (Spergel *et al.*, 2007), in agreement with the results from quasars, whereas Planck suggested an instantaneous reionization redshift of $z = 7.68 \pm 0.79$ (Planck Collaboration *et al.*, 2018).

Similarly, population III (pop III) stars, the earliest massive stars consisting entirely of primordial gas - hydrogen, helium and very modest amounts of lithium and beryllium, are also very efficient sources of UV photons, making them a leading candidate for reionization. In 2015, (Sobral *et al.*, 2015) reported the evidence for pop III-like stellar population in the most brightest Lyman-α emitter discovered yet at the epoch of reionization (at $z = 6.60$). These pop III stars exploding as supernovae are likely to produce chemical elements heavier than hydrogen necessary for the formation of stars and planets around us today.

1.2 High-redshift galaxies

Amongst the several techniques used in the identification of high redshift galaxies, the two methods that have proved most effective in producing large samples of star forming galaxies at early times are the Lyman-break and the Lyman-α selection technique, bringing a new era in the study of the high-redshift Universe.

The Lyman-break technique, first successfully implemented by Guhathakurta, Tyson & Majewski (1990) and Steidel & Hamilton (1992), takes advantage of the fact that the UV continuum of star forming galaxies at energies higher than the Lyman limit at 912 Angstrom is completely absorbed by the neutral hydrogen around star-forming regions of galaxies (as well as by the intervening clouds along the observer's light-of-sight), resulting in a characteristic drop at 912 Angstrom. By using a selected set of optical filters above and below the wavelength of the redshifted Lyman limit, Steidel & Hamilton (1992) were able to select a star-forming galaxy at $z \sim 3.4$ by utilizing the differing appearance of the galaxy in the filters. The

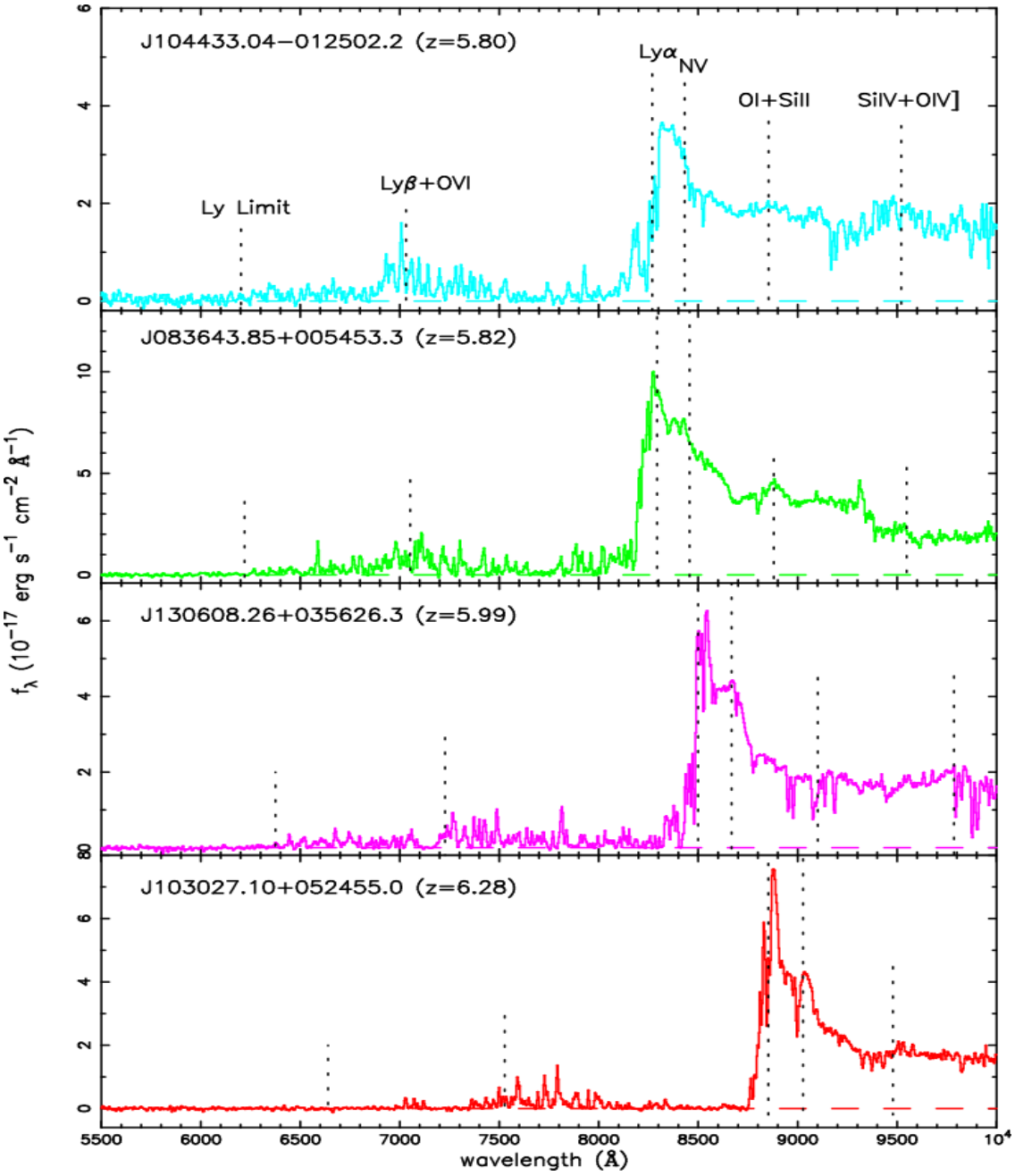


Figure 1.2: Discovery of Gunn-Peterson trough in a $z = 6.28$ quasar. The absence of the trough in quasars at redshifts $z = 5.80$, $z = 5.82$ and $z = 5.99$ demonstrated strong evidence for the completion of reionization around $z = 6$. Figure from Becker *et al.* (2001).

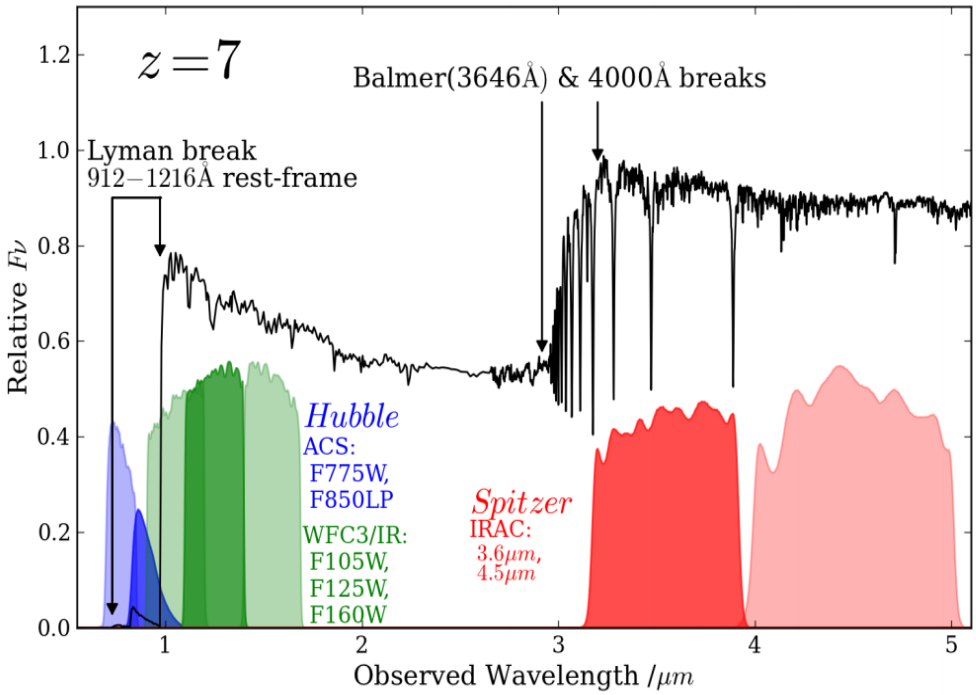


Figure 1.3: An example of a redshifted spectral energy distribution (SED) from a galaxy at $z \simeq 7$. A sharp drop in the spectrum is seen at 1216 Angstrom due to the Gunn-Peterson absorption.(Credit: S. Rogers.)

validity of this method was further shown by spectroscopic confirmation of galaxies at this era by Steidel *et al.* (1996a) and Steidel *et al.* (1996b).

Additionally, as mentioned above, the intervening neutral hydrogen clouds also generate a series of Lyman-α absorption lines resulting in Lyman-α forest (also known as Gunn-Peterson trough), such that all the flux shortward of Lyman-α is quenched, making the original 912 Angstrom break insignificant. The selection of objects with the Lyman-break method then essentially becomes a selection of objects with a break at 1216 Angstrom instead (See Fig. 1.3).

The second method, the Lyman-α method, selects galaxies on the basis of their redshifted Lyman-α emission lines (and hence called Lyman-α emitters; LAEs). This bright Lyman-α emission, produced by ionization of hydrogen atoms in the interstellar medium by the UV light from young stars, was first suggested as a signature to detect normal star-forming galaxies at early times by Partridge & Peebles (1967), with its first accidental success in discovering a Lyman-α emitting galaxy at $z = 5.34$ by Dey *et al.* (1998).

With the only drawback of their preferential selection of young galaxies that produce abundant amounts of UV light (and relatively dust free in order for the light to escape the galaxy in our direction), both these methods brought a revolution

in the study of the high-redshift Universe. The deep *HST* Wide Field and Planetary Camera 2 (WFPC2) imaging of the Hubble Deep Field (HDF; Williams *et al.* 1996; Ferguson, Dickinson & Williams 2000) and HDF-South (HDF-S; Casertano *et al.* 2000; Ferguson, Dickinson & Williams 2000; Williams *et al.* 2000), allowed the detection of a significant number of star forming galaxies out to $z = 5$ through the Lyman Break technique (e.g., Madau *et al.* 1996). Subsequent observations of the HDF and HDF-S in the infrared with *HST*'s Near Infrared Camera and Multi-Object Spectrometer (NICMOS) allowed the detection of even higher redshift galaxies at $z \sim 6$ both photometrically (e.g., Bouwens *et al.* 2003; Thompson 2003) and spectroscopically (e.g; Steidel *et al.* 1996a; Bunker *et al.* 2003). The installation of the Advanced Camera for Surveys (ACS) on *HST* in March 2002 produced the deepest and most iconic optical image of the sky, the Hubble Ultra Deep Field (HUDF; Beckwith *et al.* 2006). The ACS was also used as a part of the Great Observatories Deep Survey (GOODS) program (e.g., Giavalisco *et al.* 2004) during the same time. Together with deep *Spitzer* IRAC imaging and K-band imaging (at 2.2μm), this data uncovered new distant galaxy populations out to $z \sim 6$ (e.g., Bouwens *et al.* 2003; Stanway, Bunker & McMahon 2003; Beckwith *et al.* 2006; Grazian *et al.* 2006).

At $z \simeq 7$, the Lyman break has been redshifted from the optical into the near-infrared wavelengths ($\lambda \sim 1\mu$m) and therefore detections of galaxies at $z > 6.5$ were mainly restricted by the lack of adequately deep near-infrared imaging. With the installation of Wide Field Camera 3 (WFC3) on *HST* in May 2009, and the infrared (IR) channel of its camera, the detection of galaxies was pushed to $z \simeq 7$ and beyond (e.g., McLure *et al.* 2010; Bunker *et al.* 2010; Finkelstein *et al.* 2010; Labbé *et al.* 2010; Bouwens *et al.* 2010; Grazian *et al.* 2011). The increased efficiency and wider field near-infrared imaging also enabled surveys such as Cosmic Assembly Near-infrared Deep Extra-galactic Legacy Survey (CANDELS; Grogin *et al.* 2011; Koekemoer *et al.* 2011) to commence. Thanks to the advent of WFC3 on *HST*, and a series of observing programs like the HDF, HUDF, GOODS and CANDELS, the number counts of high redshift sources now lie in the thousands at $z \simeq 6$, hundreds at $z \simeq 7$ and ~ 300 at $z \geq 8$ (Laporte *et al.*, 2015).

With the advancement in the number of optical and infrared filters, a new approach of photometric redshift selection to find high redshift galaxies instead of the traditional two-colour drop-out technique came into existence (e.g; McLure *et al.* 2006). The photometric redshift selection method involves fitting a set of template spectra (SED template fitting) to the full broadband observed photometry of a galaxy to estimate the redshift by chi-squared minimization technique (e.g., Bol-

zonella, Miralles & Pelló 2000; Brammer, van Dokkum & Coppi 2008) or maximum likelihood Bayesian approach (e.g., Benitez 2000). The advantage the photometric redshift selection method has over the colour-colour method is that it uses photometry in all the available bands, including non-detections. It is also able to take into account the shape of galaxy spectrum above breaks such as the Lyman break and the Balmer break, which is not possible in a single colour. These features help secure the uncertainty in redshift as well as uncertainties in properties such as the resulting stellar mass, ages, star formation rates (SFRs) etc. for each source. Finally, it also produces a probability distribution across the redshift space (e.g; Finkelstein *et al.* 2010) for each source, revealing multiple redshift solutions, allowing one to inspect alternative solutions and hence reject the low redshift interlopers with follow-up spectroscopic observations. Chapter 2 of this thesis describes the photometric redshift selection technique used to build our sample of high redshift galaxies.

However, regardless of the benefits of SED fitting over the traditional two-colour drop-out technique, there could also be systematic biases in the results from SED fitting due to incorrect prescription of reddening laws and star formation histories (See Schenker *et al.* 2013). Also, proper care must be taken while selecting the templates, particularly by ensuring that they can deal with a wide range of low redshift interlopers by allowing relatively large reddening values. Two interdependent studies by McLure *et al.* (2013) and Schenker *et al.* (2013) used the HUDF12 data set to derive the UV luminosity function (UV LF) at $z = 7 - 8$. McLure *et al.* (2013) used the SED fitting technique, whereas Schenker *et al.* (2013) opted for a colour-selection method, finding similar results. This shows, on the other hand, that both these methods can be used to an immense extent in the studies of the high-redshift Universe.

1.3 Luminosity functions and Mass functions

Following the detection of statistically significant number of high-redshift galaxies it became possible to make one of the most basic measurements about a galaxy population – its census. This is achieved by the creation of the galaxy luminosity function (LF), which is the number density of galaxies per luminosity bin. In fact, measuring this census as a function of redshift and luminosity is fundamental to investigate galaxy evolution across time and to understand the process of cosmic reionization. The luminosity functions for Lyman break galaxies are typically determined at $\lambda_{rest} \sim 1500$ or $\lambda_{rest} \sim 1600$ Angstrom, whereas the luminosity functions

for the LAEs are characterized by integrating the Lyman-α line.

Previous studies have shown that the galaxy UV LF is well fitted by the Schechter (1976) parametrisation of the form:

$$\phi(L) = \Phi^*(\frac{L}{L^*})^{\alpha} \exp(-\frac{L}{L^*}). \tag{1.1}$$

The Schechter function can also be expressed in log space as,

$$\phi(M) = 0.4ln(10)\phi^* 10^{-0.4(M-M^*)(\alpha+1)} e^{-10^{-0.4(M-M^*)}}, \tag{1.2}$$

where ϕ^* provides the normalization, M^* (referred to as the knee of the Schechter function) corresponds to the characteristic magnitude at which the function turns over from a power law into an exponential form, and α is the faint-end slope. The faint-end slope is typically negative, denoting an abundance of faint galaxies.

These three parameters characterize the shape of the LF and an accurate determination of these parameters is necessary, as it has implications for the process of reionization. For example, the UV luminosity density (and hence the cosmic star formation rate density) is usually estimated by integrating the UV LF and therefore depends strongly on the faint-end slope of the LF. The faint-end slope in turn also depends on completeness corrections and since an overcorrection can lead to an artificial steepening of the faint-end slope, careful simulations are needed when the survey data is pushed towards the detection limit. In Chapter 2 of this thesis we describe in detail the completeness simulations undertaken in this work.

The UV LF has been studied at high-redshift extensively over the last couple of decades by several teams (e.g; Bouwens *et al.* 2007; Oesch *et al.* 2010; Grazian *et al.* 2011; McLure *et al.* 2013; Finkelstein *et al.* 2015; Bouwens *et al.* 2015b). Especially, since the installation of WFC3 on *HST*, galaxies are now being discovered out to $z \sim 11$ (e.g; Oesch *et al.* 2016), well into the epoch of reionization. These studies suggest that early star forming galaxies could well be the best candidates to drive reionization, as studies with *HST* have found that faint galaxies were substantially more abundant than bright ones in this epoch (See Fig. 1.4). One implication of these studies is that faint galaxies (those below the detection limits of *HST*) produced most of the energy that contributed to reionization. However, just as these early galaxies influenced their environment by ionizing the intergalactic medium, feedback from the reionization process is believed to have suppressed star formation in galaxies below some limiting mass. To date, this has only been predicted in

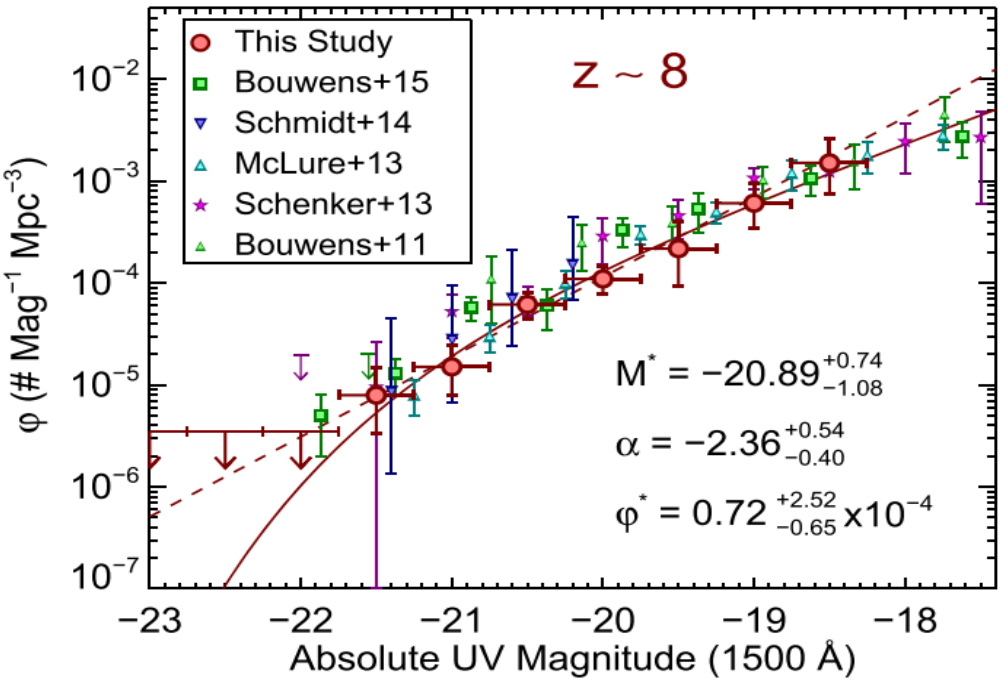


Figure 1.4: Rest-frame UV LF at $z \sim 8$ from Finkelstein *et al.* (2015). The solid red line shows their best-fitting Schechter function, with the best-fit values given by the inset text, revealing a steep faint-end slope that indicates a significant contribution from faint galaxies.

theoretical models (e.g; Finlator, Oppenheimer & Davé 2011; Jaacks *et al.* 2012; Gnedin 2016) as the galaxies are too faint to be seen with *HST*. Some of these models predict so much suppression of star formation that galaxies cannot produce enough ionizing radiation to reionize the Universe. This therefore presents a challenge for our models of galaxy formation and poses the question of whether there are enough galaxies to provide the required number of ionizing photons, requiring us to probe magnitudes fainter than *HST*'s limit. The Hubble Frontier Fields (HFF) is a Director's discretionary time campaign (Lotz *et al.*, 2017) designed for this purpose: deep imaging of six cluster fields allowing us to detect intrinsically faint, magnified galaxies over the full range of magnitudes required to sustain reionization beyond *HST*'s limit, before the advent of the James Webb Space Telescope (JWST). In Chapter 2 we present further details of the HFF program and its aims.

The drawback of the UV LF, however, is that it is sensitive to dust within the star-forming galaxies, and therefore is a dust-affected measure of the instantaneous star formation rate of a galaxy. For this reason, in order to fully understand the physical processes that dictate star formation in galaxies, it is crucial that we measure the fundamental properties such as stellar mass or ages and metallicities of the stellar populations within a galaxy. While the UV LF describes the ongoing star

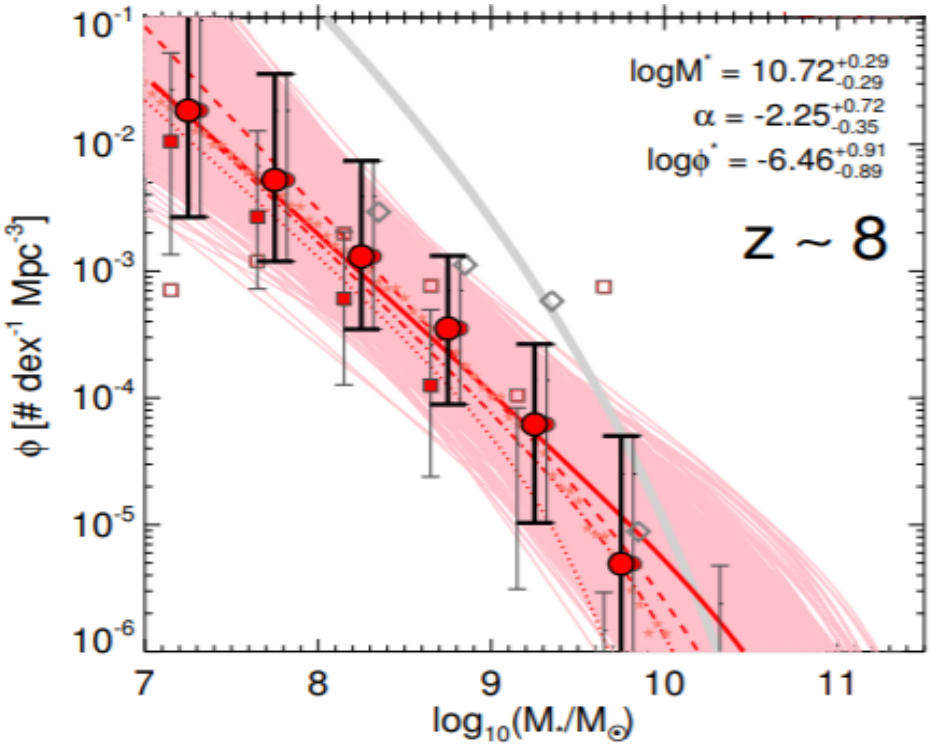


Figure 1.5: The GSMF at $z \sim 8$ from Song *et al.* (2016). The solid red line shows their best-fitting Schechter function, with the best-fit values given by the inset text, revealing a steep low mass end slope.

formation, the stellar mass is the time integral of past star-formation and the merging history of a galaxy and thus reveals the past formation. It also allows direct comparison with analytical or computational models of galaxy formation and evolution since they provide stellar mass functions as one of their fundamental outputs (e.g; Bower *et al.* 2006; Choi & Nagamine 2010; Finlator, Oppenheimer & Davé 2011).

Just as for the UV LF, galaxy stellar mass functions (GSMF) have also been studied widely at high redshift (e.g; Labbé *et al.* 2010; McLure *et al.* 2011; Duncan *et al.* 2014; Song *et al.* 2016). What these studies reveal is that the GSMF also becomes steeper with redshift such that there are more lower mass galaxies (per unit volume and relative to high mass galaxies) at high redshift than at lower redshift (See for example Fig. 1.5). At some stellar mass limit the mass function may turn over and thus deep observations beyond *HST*'s limit with surveys such as the HFF are needed to help us answer this.

However, obtaining accurate estimates of stellar masses from data that only probe the rest frame UV continuum is a non-trivial task. This is because the UV continuum is produced by young and massive but short-lived O, B stars and therefore is dominated by ongoing or recent star-formation, which is more sensitive

to dust attenuation as mentioned above. For this reason, the stellar masses should preferably be estimated from the rest-frame infrared emission at $\lambda_{rest} \sim 1.6\mu$m. However, at $z \simeq 5$ this is redshifted to $\lambda_{obs} \geq 10\mu$m and thus not attainable until the arrival of JWST. The Balmer break/4000 Angstrom break is vital in the measurement of stellar masses and therefore mid-infrared observations (at $\lambda_{obs} = 3.6\mu$m and $\lambda_{obs} = 4.5\mu$m) from the IRAC camera onboard *Spitzer* Space Telescope has proven crucial in providing reliable estimates of stellar masses of high redshift galaxies (e.g., Labbé *et al.* 2006; Stark *et al.* 2007; González *et al.* 2010, 2011; Duncan *et al.* 2014; Song *et al.* 2016). Stellar masses at high-redshift are much better constrained by including rest-frame optical photometry with mid-infrared imaging probed by the IRAC bands. This requires combining accurate photometry from *HST* and IRAC bands, but extracting accurate photometry from low resolution images is demanding due to the order-of-magnitude difference in resolution in *HST* and *Spitzer* data. This necessitates the application of deconfusion methods with software such as T-PHOT (Merlin *et al.*, 2015) as discussed in Chapter 2.

Finally, since these IRAC bands still probe the rest-frame optical emission at $z > 5$, the estimated stellar masses are affected by redshifted nebular emission lines such as Hα, [OII] and [OIII], potentially contaminating the broadband fluxes and biasing the SED fitting results. Several studies of galaxy SEDs at high redshift indicated the over estimation of galaxy properties such as stellar masses and ages due to such contamination (e.g; Schaerer & de Barros 2009, 2010; Ono *et al.* 2010). Therefore, it is important to include the effects of nebular emission in SED fitting in order to make un-biased measurements of galaxy properties of star forming galaxies at high-redshift. Taking into account all these concerns, we construct a multiwavelength photometry catalog from 0.4 to 4.5μm and estimate the stellar masses of our high-redshift sample using SED fitting technique with the inclusion of nebular emission lines in this thesis (See Section 2.3.6.1). In Chapter 2, we describe the construction of our multiwavelength photometry catalog and the estimation of stellar masses in detail.

1.4 Probing the Epoch of Reionization with lensing

Galaxy clusters are the largest gravitationally bound structures in the Universe, first studied by Zwicky in 1933. He was the first to determine the mass of galaxies within the Coma cluster using the Virial Theorem, estimating it to be 400× greater

than expected for their luminosity alone. This gave the first hints of the existence of dark matter, which he then referred to as "dunkle Materie" (Zwicky, 1933).

As shown in Fig. 1.6, these massive structures distort the space around them in such a way that the light from sources behind them is magnified. This gravitational lensing effect can result in magnifications of up to $\sim 100\times$ (e.g; Kneib & Natarajan 2011). With gravitational lensing from massive clusters, two distortion effect occur: strong lensing and weak lensing. In strong lensing, the light from source galaxies is bent by the curvature of space-time, which can be identified visually in the form of multiple images of background source strongly distorted into rings/arcs. The magnitude of distortion depends on the relative positions of the source, lensing object and observer, as well as the mass of the lensing object. If the geometry of the aforementioned objects is favourable, the distortions will be more prominent and will be characterized as strong gravitational lensing. In weak lensing, despite the massive lensing object, the geometry is less favourable, and therefore the effects of weak lensing are detected in the form of weak smears of arcs of singly imaged background sources centred on the lens center, an effect known as shear. This shear can be measured statistically by taking an average of several background galaxies further from the core of the lensing cluster. There are two ways in which these features can be exploited to study the background galaxies: firstly, the spatial magnification allows us to resolve galaxies and explore their internal properties in much greater detail than blank-field surveys; and secondly, the flux magnification enables the detection of fainter sources, allowing us to reach far beyond the observational limits of current telescopes.

The successor to *HST*, JWST will have 7 times the collecting area with double the field of view and will search for the First Light objects in the redshift range of $z = 10 - 15$. It will also observe further into the infrared and will revolutionise our understanding of the early Universe, providing access to galaxies that have never been visible before. Accessing these galaxies will be customary with JWST, however, until then, an innovative way of exploiting current telescope facilities beyond their nominal limits is to take advantage of the magnification effect caused by gravitational lensing.

This technique has already been used in the Cluster Lensing and Supernova Survey (CLASH; Postman *et al.* 2012), a 524-orbit *HST* Multi-Cycle Treasury Program aiming to study the gravitational lensing properties of 25 galaxy clusters. Before October 2013, the deepest WFC3/IR observations of any strong lensing cluster were just 7 orbits. These have still enhanced the results from "blank" field programs such as the Ultra Deep Field (UDF; Illingworth *et al.* 2013; Ellis *et al.* 2013)

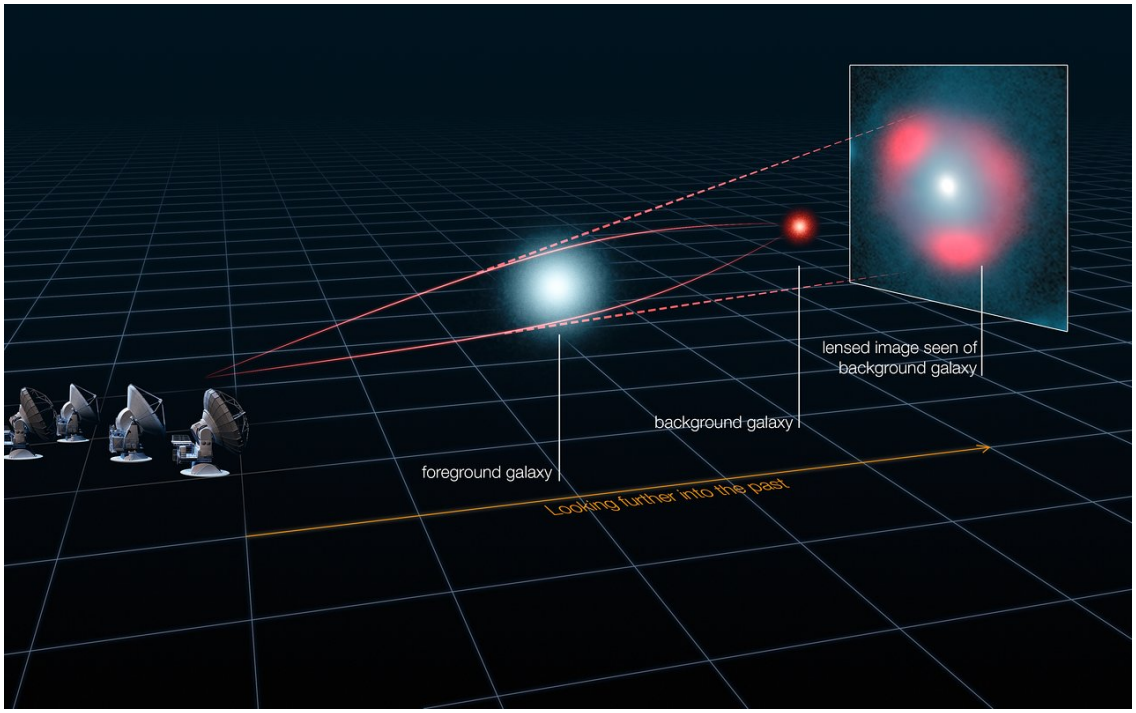


Figure 1.6: Massive objects such as galaxy clusters distort the space around them in such a way that the light from sources behind them is magnified. This gravitational lensing effect can result in magnifications of up to a factor of $\sim 100\times$, allowing us to directly observe the faintest galaxies beyond *HST*'s limit. (Credit: ALMA (ESO/NRAO/NAOJ), L. Calada (ESO), Y. Hezaveh et al.)

and CANDELS in the search of the most distant galaxies. With just a few *HST* orbits, CLASH discovered numerous $z > 9$ candidates highly magnified by massive clusters at $z \sim 0.5$ (e.g; Zheng *et al.* 2012; Coe *et al.* 2013; Bouwens *et al.* 2014a). Several other candidates were detected at $z \sim 9-10$ with CLASH (e.g; Zheng *et al.* 2012), the UDF (e.g; Oesch *et al.* 2013) and CANDELS (e.g; Oesch *et al.* 2014). A fairly large sample of ~ 100 candidates were reported at $z \sim 8$ from CLASH and blank fields (e.g; Bradley *et al.* 2014).

To complement these results and to provide us with a glimpse of the cosmos to be unveiled by JWST, *HST* started a three year program at the end of 2013, called the Hubble Frontier Fields, to observe six clusters of galaxies (Abell 2744, MACS J0416.1-2403, MACS J0717.5+3745, MACS J1149.5+2223, Abell S1063 and Abell 370) and six nearby blank fields (The details of the HFF survey are presented in Chapter 2). The reason that these clusters were observed was because they provide a magnified boost to the light from the background galaxies thus providing us with a deeper view of the Universe than we would obtain from just examining the blank fields, whilst the blank fields provide a larger area for deep observations as well as reducing the cosmic variance uncertainty. The revealed lensed galaxies include some of the most distant yet known, however some (but not all) of their observed

and derived properties will be affected by strong gravitational lensing and need to be corrected for.

The brightness of source galaxies is amplified as they get magnified and therefore the observed luminosities and derived quantities must be corrected for lensing magnification with the help of lensing models (which come with their own uncertainties) using,

$$\mu = \frac{1}{(1-\kappa)^2 - \gamma^2}, \tag{1.3}$$

where μ is the magnification factor, κ is the mass surface density and γ is the weak lensing shear. The quantities κ and γ scale with the distance ratio D_{LS}/D_S; D_{LS} being the angular diameter distance between the source and the cluster, and D_S the angular diameter distance between the observer and the source. In Chapter 2 we describe in detail the method used to compute the magnification factor.

The derived quantities that will be affected by lensing include SFRs, stellar masses and sizes of individual sources. However, the ratio of SFR and stellar mass (called as the specific star formation rate; sSFR) will be immune to the errors in magnification as these quantities are affected to the same degree by lensing magnification. Finally, since lensing is achromatic (unless the source is extended, which can produce differential lensing and hence modify colours in an aperture), the quantities extracted from colours or spectra such as UV colours (rest-frame UV slope β), redshift, age, metallicity, extinction are also not affected by lensing.

1.5 Thesis Outline

The aim of this thesis is to exploit the power of gravitational lensing of massive clusters by combining *HST*, Very Large Telescope (VLT) and *Spitzer* imaging of the MACSJ0416.1-2403 cluster and its parallel field to study the faint end of the UV LF and the low mass end of the GSMF along with SFRs and UV colours during the epoch of reionization at $z = 6 - 9$ with the Hubble Frontier Fields.

Chapter 2 describes the method developed to subtract the massive foreground galaxies from the cluster, allowing for a deeper and cleaner detection of the faintest systems at $z \geq 6$ and the construction of the multiwavelength catalog, from 0.4 to 4.5μm, using *HST*, *Spitzer* and ground-based VLT data. It also describes the photometric redshift determination method and the selection criteria used to construct

our sample of high-redshift galaxies at $z = 6 - 9$, along with the completeness simulations undertaken to take into account the effects of completeness and selection functions. In this chapter, I also outline the SED fitting method used to estimate the stellar masses, rest-frame UV magnitudes and star formation rates for our sample. This chapter is concluded with a description of the method used for estimating the volume (and hence number densities) including the effects of lensing, required for luminosity and mass functions.

Chapter 3 presents the results by including a derivation of the GSMF, UV LF and an analysis of the mass-to-light ratio of our sample of galaxies. The estimated total stellar mass density (SMD), the specific star formation rates (sSFR) and the UV luminosity density is also presented and discussed in this chapter.

Chapter 4 investigates the evolution of the galaxy rest-frame UV colours using the same sample of galaxies at $z = 6 - 9$ from Chapter 2 in the Hubble Frontier Fields.

In the final chapter I present the conclusions of the work done in this thesis and discuss the future work that can build upon these results.

Throughout the work in this thesis, a ΛCDM cosmology with $H_0 = 70$ km s^{-1} Mpc^{-1}, $\Omega_M = 0.3$, and $\Omega_\Lambda = 0.7$ is adopted. All magnitudes are quoted in the AB system (Oke & Gunn, 1983), and a Chabrier (2003) stellar initial mass function is used unless specified otherwise.

Chapter 2

Data and methods

The Hubble Frontier Fields survey serves as an excellent dataset to study the faintest and earliest galaxies in the Universe, $\sim 10 - 100$ times fainter than any previously observed. However, in addition to a good quality survey data, an essential factor in the study of high-redshift galaxies is the measurement of accurate photometry in the wavebands of interest. This chapter describes in detail the HFF dataset as well as the construction of the multiwavelength catalog, which was used to estimate the photometric redshifts and the measurement of properties such as stellar mass, star formation rates, rest-frame UV magnitudes and rest-frame UV colours.

2.1 Introduction

Exploring the very first galaxies is one of the major contemporary problems in astronomy. We do not know when the first galaxies formed, nor how their formation occurred – two related but distinct questions. Until JWST launches, these problems can be best addressed through deep imaging observations, particularly with *HST*. Hubble allows us to view the Universe back to within 500 million years of the Big Bang, and perhaps earlier. This allows us to address the question of how much of the current galaxy population was in place at these early times, and perhaps to also investigate the deeper question of how that formation occurred. *HST* has spent several 1000s of orbits over two decades on the various Hubble (Ultra) Deep Fields, to understand the formation and evolution of galaxies, which existed when the Universe was 500 million years old until today. This has led to interesting results on early galaxy formation and cosmic dawn at redshifts $z \sim 6 - 10$ (e.g.,Bouwens *et al.* 2011, 2015b; Finkelstein *et al.* 2012; McLure *et al.* 2013; Schenker *et al.* 2013; Schmidt *et al.* 2014; Duncan *et al.* 2014; Ishigaki *et al.* 2018). However, undetected $z > 6$ dwarf galaxies beyond the detection limit of *HST* are required to complete

reionization by $z \sim 6$ (e.g., Finkelstein *et al.* 2015; Robertson *et al.* 2015). Similarly, since scarcely any candidates at $z \geq 9$ were discovered (e.g., Zheng *et al.* 2012; Coe *et al.* 2013; Oesch *et al.* 2013), this led to a debate on how many $z > 9$ sources will be found with JWST (e.g., Oesch *et al.* 2012) and whether galaxies could solely complete the reionization process by $z \sim 6$. To address these questions, *HST*, along with the *Spitzer Space Telescope*, began an ambitious multi-cycle three year observing program at the end of 2013, called the Hubble Frontier Fields, to provide us with a deeper view of the Universe than ever before.

2.1.1 Hubble Frontier Fields

To extend its reach even farther beyond its native technical capabilities, before the launch of JWST, *HST* observed six massive clusters of galaxies as gravitational lenses as a part of the HFF program (Lotz *et al.*, 2017). Using Director's Discretionary (DD) observing time, the HFF program (FF program 13495; P.I. Lotz, Co-PI: Mountain) imaged six massive clusters (Abell 2744, MACSJ0416.1-2403, MACSJ0717.5+3745, MACSJ1149.5+2223, Abell S1063, Abell 370) and their associated parallel fields for 140 orbits each, with the ACS and WFC3 onboard *HST*, in three optical (F435W, F606W, and F814W) and four near-infrared (F105W, F125W, F140W, and F160W) bands over two epochs. These clusters are being used as gravitational lenses to magnify faint distant galaxies, while the flanking fields are for deep observations of otherwise blank areas. The parallel field images reach a depth of ~ 29 AB mag, the second deepest images ever obtained. In the highest magnification regions, the WFC3/IR images probe up to and more than 10 times deeper than the HUDF, and hence are our deepest views of the Universe to date.

The cluster targets were chosen based on: i) Their lensing strength: so as to enhance the number of detectable $z \sim 10$ sources magnified by $\sim 1.5 - 100\times$ within *HST* WFC3/IR field of view. ii) Zodiacal background and Galactic extinction: as the exploration of the very faint distant Universe is restricted by the foreground Galactic extinction as well as the brightness of the sky. They therefore had to be in relatively clean regions of the sky at high Galactic latitude where there is little foreground dust, in addition to being at high ecliptic latitudes to lessen the impact of zodiacal background. iii) Existing ancillary data: as several of the candidate clusters were previously observed by facilities such as *HST*, *Spitzer*, *Herschel* and *Chandra*, and finally iv) The observability by *HST* (ACS and WFC3), JWST and ground based facilities such as the Atacama Large Millimeter/submillimeter Array (ALMA) and VLT. Fig. 2.1 shows the names and locations of the six Frontier Fields

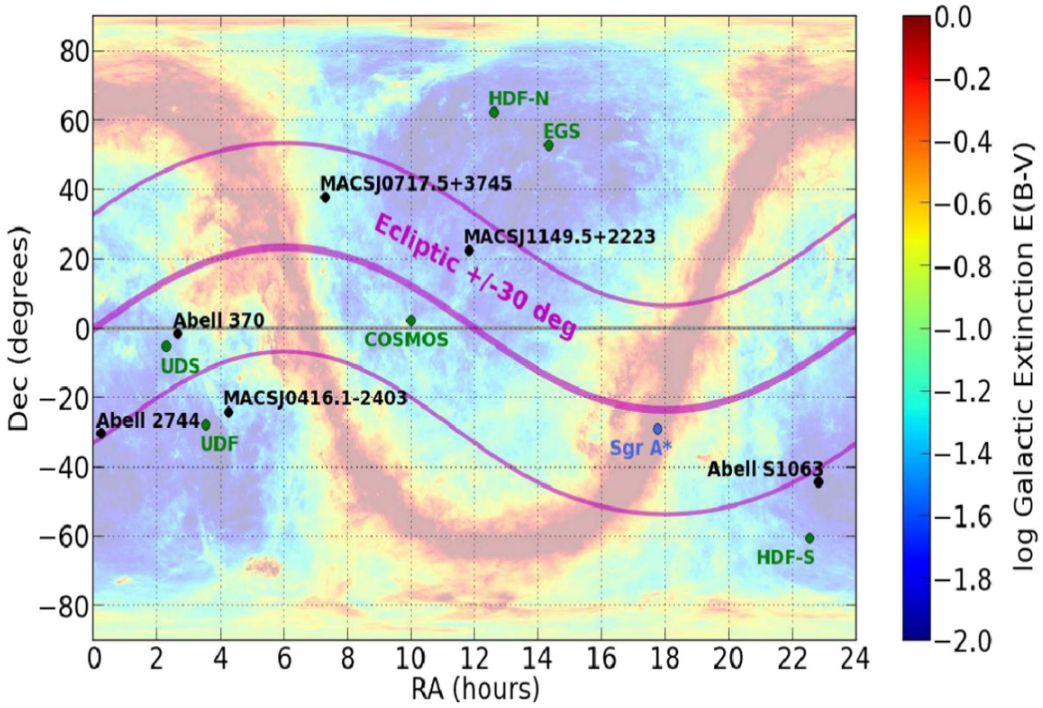


Figure 2.1: Names and locations of the six Frontier Fields cluster + parallel field pairs. Also shown are HDF-N, HDF-S, UDF, COSMOS, EGS, and UDS fields for reference (Figure from Lotz *et al.* (2017)).

chosen for the HFF program.

The primary scientific goals of the HFF program are:

- To uncover distant populations of $z = 5 - 10$ galaxies that are $10 - 50$ times fainter than any presently known
- To strengthen our understanding of the stellar mass function at the earliest times by characterizing the stellar populations of faint galaxies at high redshift.
- To provide a statistical morphological characterization of star-forming galaxies at $z > 6$ for the first time
- To find $z > 8$ galaxies that are stretched out by a great extent by massive foreground clusters to determine the internal structure and sizes and/or magnified enough for spectroscopic follow-up.

It is the first two of these areas that this thesis focuses on.

2.2 The Data

2.2.1 HST data

Observations of MACSJ0416.1-2403, hereafter MACSJ0416, (RA: 04:16:08.9, Dec: -24:04:28.7) and its parallel field (RA: 04:16:33.1, Dec: -24:06:48.7) were carried out between Jan 2014–Feb 2014 (Epoch 1) and July 2014–September 2014 (Epoch 2) as a part of the HFF program. In this study, we use the final reduced and calibrated v1.0 mosaics and their associated weight and rms maps provided by the Space Telescope Science Institute (STScI) on the HFF website [1], drizzled at 60 mas pixel-scale. For a detailed description of data release, including the data reduction pipeline, exposure times, and calibration procedures, we refer the reader to the STScI data release documentation [2].

We compute the depth of these *HST* images by placing 100s of 0.″2 radius apertures in random positions on the images and measuring fluxes in them. Table 2.1 lists the resulting 5σ limiting magnitudes for the seven bands using our detection methods. We find that the 5σ limiting magnitudes of the cluster are lower than the parallel field (See Table 2.1). This is the result of the cluster field being dwarfed by the light from the massive foreground galaxies, making the effective raw depths shallower than the parallel field.

2.2.2 VLT data

HFF data by itself is inadequate for characterizing the galaxies we are interested in at $z \geq 6$. Typically, the way to study the stellar masses and stellar populations of $z \geq 6$ galaxies is through the use of *Spitzer*/IRAC data at $> 3\mu$m. This is often included and used along with *HST* imaging in addition to K_s band, the reddest ground based filter we can obtain deep imaging data from. In fact, good quality K_s band data has been crucial to fully exploit *Spitzer*/IRAC data, which has poor resolution and is affected by blended sources. Finally, K_s band at 2.2 μm also fills in the gap between the 1.6μm F160W band and the IRAC 3.6μm band.

Because of the aforementioned reasons, and in order to put better constraints on redshift estimates, we include longer wavelength K_s band data in our analysis. K_s band observations of MACSJ0416 fields were obtained between October 2013 and February 2014 with the High Acuity Wide-field K-band Imager (HAWK-I) on the 8.2 m UT4 telescope at the ESO Very Large Telescope. We use the fully

[1] http://www.stsci.edu/hst/campaigns/frontier-fields/FF-Data
[2] https://archive.stsci.edu/pub/hlsp/frontier/

reduced K_s band images that are made available to the public through the Phase 3 infrastructure of the ESO Science Archive Facility (ESO program 092.A-0472, P.I. Brammer). The full HAWK-I $7'.5 \times 7'.5$ field of view covers both the cluster and the parallel fields in a single pointing.

Similar to *HST* bands, we calculate the depth of the image by placing 100s of $0''.4$ radius apertures in random positions on the image and measuring fluxes in them. Table 2.1 describes the 5σ limiting magnitudes for the K_s band. We refer the reader to Brammer *et al.* (2016) for a detailed description of observations and data reduction process.

2.2.3 Spitzer data

The Balmer break/4000 Angstrom break is crucial to estimate the age of stellar populations and subsequently in the measurement of galaxy stellar mass. This break is at observed wavelengths beyond 2.4 μm at $z > 5$, and only the IRAC camera on board *Spitzer* can identify the break. IRAC data is also essential to put better constraints on redshift estimates in addition to obtaining robust stellar mass estimates. We therefore include *Spitzer* data in our analysis. In addition to *HST*, the *Spitzer* Space Telescope has dedicated $\sim$ 1000 hours of Director's Discretionary time to observe the Frontier Fields at 3.6 μm and 4.5 μm and has observed each field for $\sim$50 hours in each channel. We use the final reduced mosaics made available to the public on IRSA website [3] (Program ID 90258, P.I T. Soifer). The depth of *Spitzer* data was again, similar to *HST* and K_s band data, computed by using a similar method of placing 100s of $1''.4$ apertures in random positions in the images. The 5σ limiting magnitudes for both the channels are as listed in Table 2.1.

[3] http://irsa.ipac.caltech.edu/data/SPITZER/Frontier/

Table 2.1: Description of dataset for the MACSJ0416 cluster and its parallel field. The 5σ depths are calculated using 100s of $0\farcs2$ radius apertures in random positions for *HST* images, $0\farcs4$ radius apertures for HAWK-I image and $1\farcs4$ radius apertures for IRAC images.

	MACSJ0416 Cluster	MACSJ0416 Parallel	
Filter	Depth (5σ)	Depth (5σ)	Instrument
F435W	28.87	28.91	ACS
F606W	28.95	29.01	ACS
F814W	29.35	29.40	ACS
F105W	29.22	29.30	WFC3
F125W	28.95	28.02	WFC3
F140W	28.85	28.93	WFC3
F160W	28.65	28.75	WFC3
Hawk-I K_s	26.25	26.35	HAWK-I
IRAC 3.6	25.10	25.16	IRAC
IRAC 4.5	25.13	25.20	IRAC

2.3 Methods

2.3.1 Divide and conquer

One aim of the HFF program is to find the faintest and the earliest galaxies in the Universe, $\sim 10 - 100$ times fainter than any previously studied, and examine their properties using clusters as gravitational lenses. While the clusters provide a magnified boost to the light from background galaxies, providing us with a deeper view of the early Universe than we would obtain from just examining blank fields, the overwhelming luminosity of the brightest galaxies in the cluster impedes the detection of the faint galaxies. For this reason, it was imperative that we first model and subtract the foreground galaxies from the cluster. In this study, we choose to model and subtract galaxies on the critical line, as shown in Fig. 2.2, since the greatest magnification of distant objects occurs along the line of sight of the densest areas of the cluster.

Two other studies Livermore, Finkelstein & Lotz (2017) and Merlin *et al.* (2016) have attempted to subtract the foreground light using wavelet decomposition method and GALFIT, respectively, delivering promising results. More recently, Shipley *et al.* (2018) have sought to model the light from the brightest cluster members that contribute significant light to the cluster using IRAF.

In this work, to subtract the massive foreground galaxies, we build upon the strategy used by Gu *et al.* (2013) to detect faint substructures in NGC 4889. As a first attempt, we try to model the brightest galaxies in the reddest band F160W, which is our detection image, using GALAPAGOS (Barden *et al.*, 2012) as a stand alone application. GALAPAGOS is a IDL based software that uses SExtractor (Bertin & Arnouts, 1996) to detect the sources, and then fits a single Sérsic profile (Sersic, 1968) to the detected sources using GALFIT (Peng *et al.*, 2002). Unfortunately, the resulting residuals from this procedure were unsatisfactory. This is primarily because GALAPAGOS uses only a single Sérsic component to model the galaxies. The galaxies in the MACSJ0416 cluster are very bright/massive and also lie in a crowded field. They therefore cannot be modelled with simply one or two Sérsic components. As the massive galaxies are embedded in a crowded field, we also need to fit and remove all the neighbouring galaxies at the same time.

To overcome these difficulties, we developed an iterative procedure, dubbed "Divide and conquer", in which we split the image into small regions, with the target bright galaxy in the center, and make use of GALAPAGOS and GALFIT on those regions to model the small neighbouring galaxies first before attempting to model the big galaxies. This procedure is essentially a series of iterations between fitting

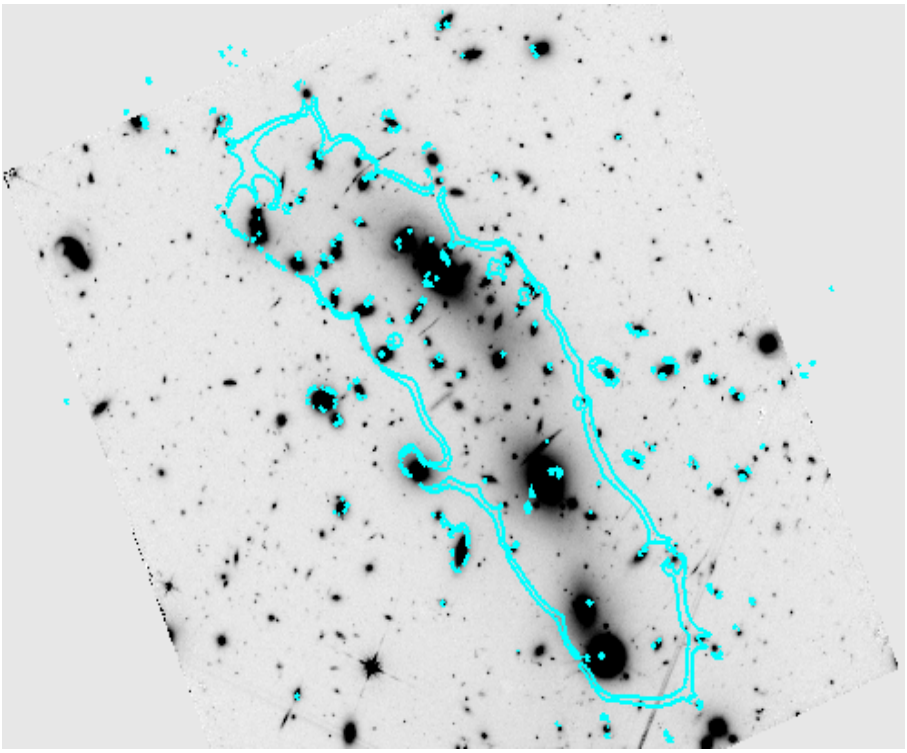


Figure 2.2: F160W image of MACSJ0416 cluster. The critical line at $z = 7$ from the CATS model (Jauzac *et al.*, 2014) is shown in cyan.

away the small objects first in a small region, one by one, using one or more Sérsic models to simulate the galaxy of interest as well as the local sky background (whose parameters are thrown away afterwards as they are only needed to approximate the sky). We keep increasing the complexity until we get a reasonable residual (e.g. there are no over-subtracted regions in the residual). This process is repeated on all the small galaxies until we are left with the central galaxy, with all the neighbours subtracted away and the process is then repeated on the central galaxy. After we get a good fit, we do a massive simultaneous fit with all the neighbours together. We then create an image with these objects subtracted out from the original image and move on to fit the next bright galaxy.

The basic steps of our method are as follows:

1. To subtract the bright galaxies, we select a rectangular patch covering the central bright galaxy, and its nearby region with smaller galaxies, and use GALAPAGOS to create postage stamps to acquire the first guess of the model parameters of each source in the stamp.

2. We then model the small neighbouring galaxies first using GALFIT, and once the small galaxies are fitted away cleanly, we model the central bright galaxy.

3. After all the galaxies in the rectangular patch are modelled accurately, we sub-

tract the final model from the original image and move to the next rectangular patch and repeat the process in iteration.

In the following sections we describe our procedure in detail.

2.3.2 Subtraction of brightest cluster galaxies

2.3.2.1 Creating postage stamps and obtaining initial guess of model parameters

Frontier Fields images are sky subtracted and in units of counts/s. The very first step that we perform, before we run GALAPAGOS, is to add sky background to the detection image (F160W band) and convert the image to counts. This was done as:

$$\mathrm{sky}^2 = \mathrm{mean} \times \sqrt{\mathrm{t_{exp}}}, \tag{2.1}$$

where mean was calculated from the rms map using IRAF and $\mathrm{t_{exp}}$ was the exposure time. Once the sky was added to the detection image, the image was scaled by the exposure time to get the image in counts (For model details refer to the STScI data release documentation mentioned in Section 2.2.1). This step was necessary in order for GALFIT to produce a reliable sigma image. We then select a rectangular patch on the detection image that consists of the target central bright galaxy and the nearby region with smaller galaxies and run GALAPAGOS on it to get the postage stamp as well as the first guess of model parameters for all the sources in the stamp. For each object that was contributing light to the stamp, we obtain the initial guesses for all the model parameters such as position within the stamp, magnitude, effective radii, Sérsic index, axis ratio and position angle required to produce a Sérsic model.

2.3.2.2 Modelling brightest cluster galaxies using GALFIT

Once the postage stamp and the initial guess of model parameters are obtained, the next step is to model the galaxies. As described above, we first model the small neighbouring galaxies, along with the local background, as accurately as possible (and eventually all the bright galaxies on the critical line).

Every galaxy is modelled using a Sérsic profile described by the following ex-

pression for the surface brightness $\sum$(r) at radius r,

$$\sum(r) = \sum_e \exp\left\{ -k\left[(\frac{r}{r_e})^{\frac{1}{n}}) - 1\right]\right\}, \tag{2.2}$$

where r_e is the half-light radius, $\sum_e$ is the effective surface brightness, k is a normalisation coefficient and n is the Sérsic index. The de Vaucouleurs profile with index $n = 4$ is a good fit for massive elliptical galaxies, and exponential profiles with $n = 1$ to Gaussian $n = 0.5$ tend to fit spiral galaxy discs and dwarf ellipticals. We start with the smallest/faintest galaxy that is contributing to the light in the stamp (with the neighbouring sources masked), with a single component Sérsic model and the initial guesses obtained from GALAPAGOS. We run GALFIT on this system and visually inspect the residual. Although the reduced χ^2 value is the most reliable method to judge the goodness of fit, for our application, since we are not striving to obtain any physical information from the parameters, we judge the goodness of fit merely by looking at the quality of the residuals; the smoothness of the residual gives a good indication of how successful the model has been. To refine the fit, we slowly build the complexity by adding additional components and visually examining the fit and the model parameters after each trial. For example, in addition to inadequate components required to model a galaxy, we also found that GALAPAGOS was unable to accurately estimate the radius for almost all the sources, defaulting to either a very small value or a very large value, resulting in poor residuals. As such, we found that GALFIT converged faster when we estimated the radius from the stamp image and changed this value manually. We note that this would be unsatisfactory were we interested in the properties of these galaxies. But since the aim is only to remove the foreground galaxies, this tuning by hand is not critical. This was similarly done for the other model parameters. We let all the fitting parameters free to vary but we fix them once we get a reasonable residual before moving on to the next galaxy.

This step is performed on all the neighbouring galaxies that contribute light to the stamp until we are left with the central target bright galaxy. We repeat the process on the target bright galaxy once again until we get a reasonable residual. Finally, we do a massive simultaneous fit with all the neighbours together. Fig. 2.3 illustrates our method, showing the postage stamp for our target brightest cluster galaxy in the center, surrounded by smaller neighbouring galaxies. For example, two components were required to model the smallest galaxy on the top and four components to model the bright galaxy below it (enclosed in green circle in the

top left panel)), revealing two faint sources (shown by red circles in the residual image). Similarly, for the massive galaxy in the middle (enclosed in green circle in the bottom left panel), six components were required, once again revealing two faint sources (shown by red circles in the residual image) that were obscured by the light of this massive galaxy. As shown in Fig. 2.3, our procedure clearly allows us to detect objects that are obscured by the bright galaxies once the bright galaxies are subtracted from the cluster. We note that the number of Sérsic components that were required to model some of the galaxies are higher than that are studied usually. However, we attribute no physical significance to the total number of components; they were solely needed for the purpose of subtraction. In this work, we obtained GALFIT models in the range $0.5 < n < 6.55$, indicating that the brightest cluster galaxies in MACSJ0416 cluster vary greatly in profile, and hence structure and morphology.

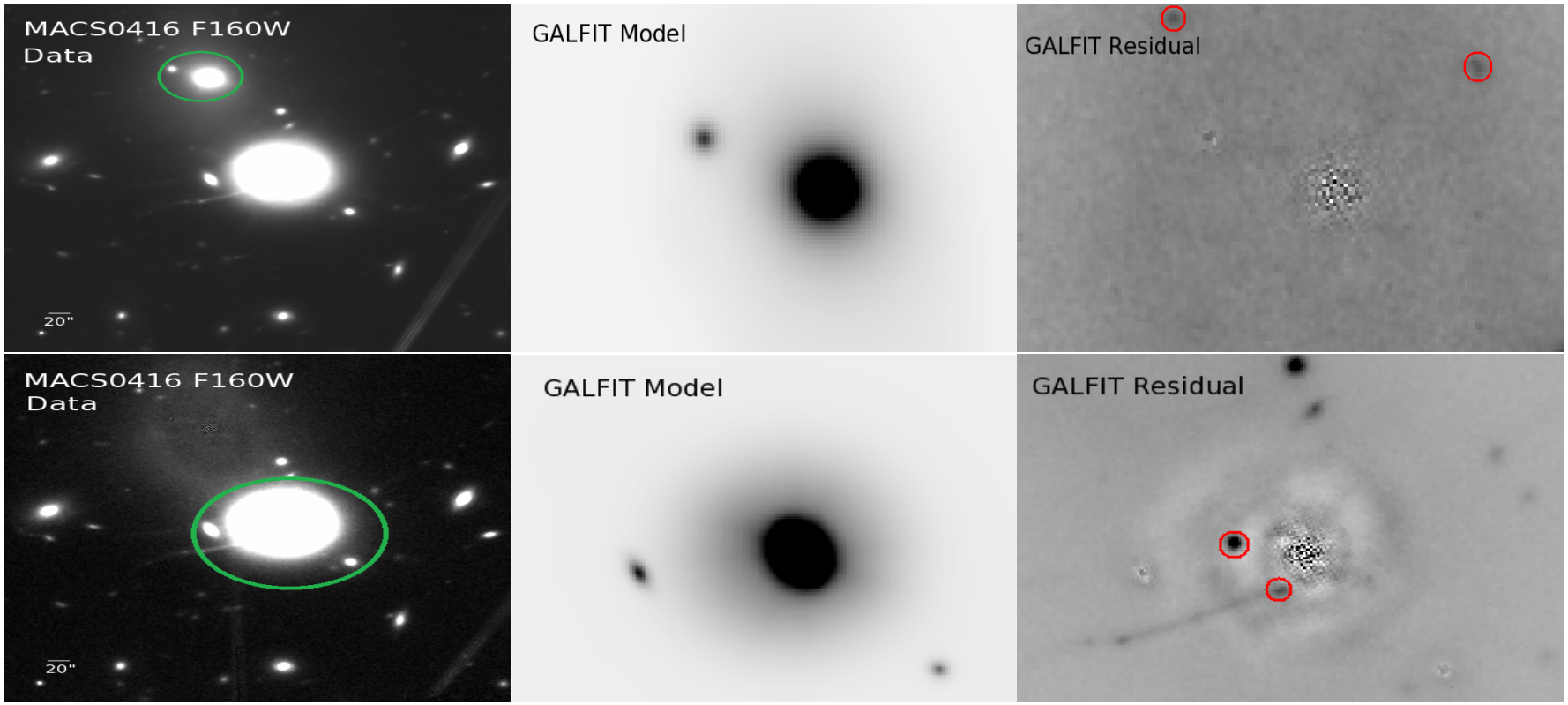


Figure 2.3: Illustration of our multi-component fitting procedure on the F160W image. Top row left: Postage stamp showing the target central bright galaxy to be subtracted along with neighbouring smaller galaxies. Middle: GALFIT models of the smaller systems on the top (shown by green circle in the top left panel) that we attempt to subtract first before subtracting the brightest galaxy in the center. Two components were required to model the smallest galaxy at the top, and four components were required to model the brighter galaxy. Right: Residual after models subtraction, revealing two faint sources shown by red circles. Bottom row left: Postage stamp with the smaller systems on the top subtracted out. Middle: GALFIT model of the brightest central galaxy (shown by green circle in the bottom left panel) we want to subtract. Six components were required to model the brightest galaxy in the center. Right: Residual image, clearly revealing the faint sources that were obscured behind it, shown by red circles.

2.3.2.3 Subtracting models from the original image

After obtaining reasonable models for all the secondary and primary sources in a stamp, we create a new object file such that the stamp pixel coordinates correspond to the pixel coordinates in the original image, along with all the other model parameters. GALFIT is then run on this new object file, resulting in an image with models only, which could be subtracted from the original image. This models-only image is then subtracted out from the original image before we move on to fit the next bright galaxy on the critical line. Steps 1 to 3 are then repeated in iteration until all the models for all the stamps are sequentially subtracted from the original image. Fig. 2.4 shows the final results of our procedure.

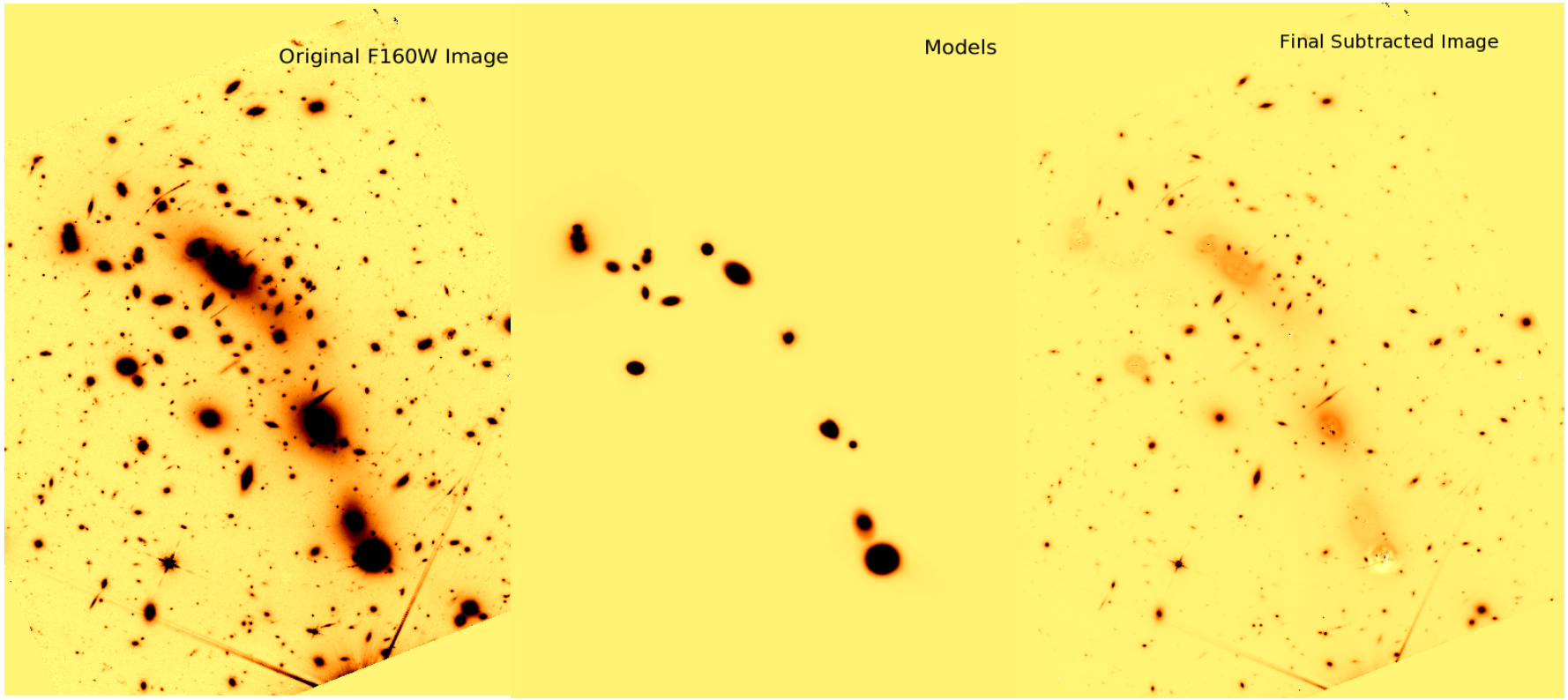


Figure 2.4: Results of our subtraction procedure on the MACSJ0416 cluster. Left to right: Original F160W detection image on which we applied our "Divide and Conquer" procedure, models of galaxies, final subtracted image. Some of the faint sources that were obscured by the light of bright galaxies are clearly seen after the subtraction procedure.

2.3.3 Multiwavelength photometry

Having subtracted the massive galaxies on the critical line of the cluster in the H-band, we proceed to construct a multiwavelength photometry catalog from 0.4 to 4.5μm. In this section we explain how we obtained our photometric measurements for MACSJ0416 cluster and its parallel field starting from our subtracted H-band.

2.3.3.1 HST images

To measure accurate photometry, we first PSF-match all the other *HST* bands to the PSF of the lowest resolution H-band (F160W) using PSFMATCH task in IRAF. Empirical PSFs were generated by stacking the images of several isolated and unsaturated stars in the field. We then use SExtractor in dual image mode with our subtracted H-band as detection image and use the same detections/apertures to perform photometry on the rest of the bands. SExtractor relies on the GAIN parameter to calculate accurate flux uncertainties. We therefore compute the effective gains for each band separately using EFFECTIVE GAIN = INSTRUMENT GAIN $\times$ EXPOSURE TIME (the instrument gain is different for ACS and WFC3/IR; 2 for ACS and 2.5 for WFC3/IR) and use this value while performing photometry.

Similarly, SExtractor is particularly notorious for underestimating the errors. To investigate this, we first perform photometry on the imaging data with SExtractor and note the errors. We then perform simulations in which we insert artificial sources with a range of input magnitudes at random positions in the imaging data and attempt to recover them with SExtractor. Fig. 2.5 shows the mean actual reported errors from SExtractor when we perform photometry on the H-band image along with the dispersion of the difference between recovered magnitudes and input magnitudes with simulations in bins of $\Delta m = 0.5$. We find that SExtractor appears to underestimate the errors by a factor of $\sim 1.5 - 2$ at all magnitudes.

To rectify this, we correct the rms maps by randomly picking 500 positions in the science image such that they are far away from the detected sources. We then measure the flux of the artificial sources inserted at the selected positions and estimate the scaling factor required to make the distribution of the computed S/N to have a standard deviation consistent with 1. The rms maps are then corrected with this scaling factor. In addition to this, we further correct the rms map following Merlin *et al.* (2016) to take into account the effect of subtracted massive galaxies on the detection and flux estimation by adding photon noise to the rms map. Since the rms map only includes the background (sky) noise in counts/sec, we also need to add in quadrature the photon noise from the big sources to have the correct

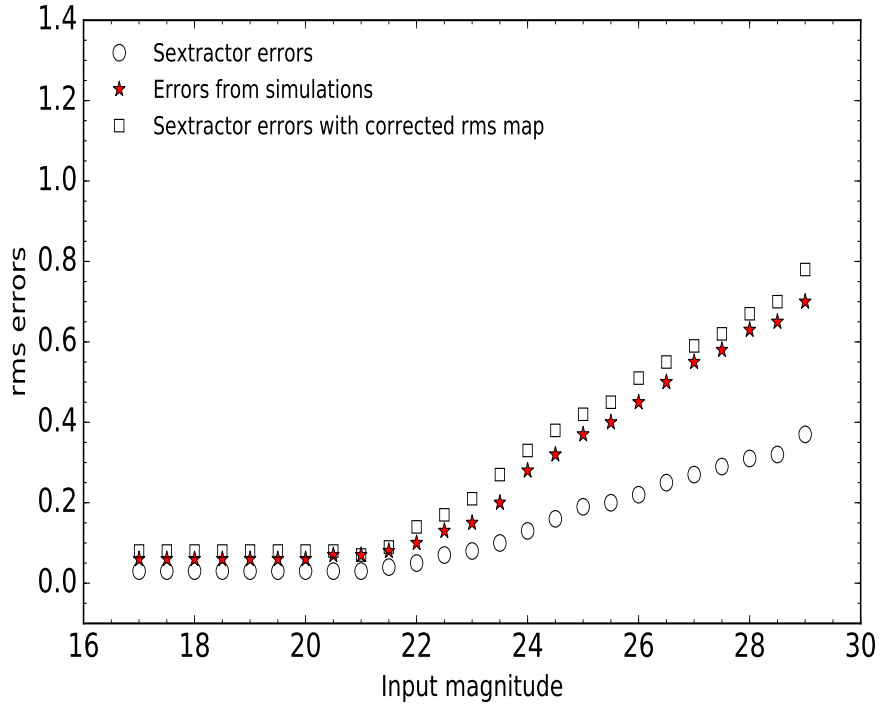


Figure 2.5: Photometric errors from SExtractor with photometry on the H-band image, dispersion of the difference between recovered magnitudes and input magnitudes with simulations, and photometric errors from SExtractor with the corrected rms map in bins of $\Delta m = 0.5$. SExtractor appears to underestimate the errors by a factor of $\sim 1.5 - 2$ at all magnitudes. The errors are noticeably improved with the corrected rms map.

rms map. The photon noise contribution is a Poisson term, i.e., it comes from the square root of the counts from sources, while the background noise is Gaussian. We do the following to have the corrected rms map in counts/sec:

$$\mathrm{rmscorr} = \sqrt{\mathrm{model/texp} + \mathrm{rms}^2}, \tag{2.3}$$

where model is the GALFIT model map and texp is the exposure time expressed in seconds.

With the corrected rms maps, we then once again measure the photometry and the associated errors with SExtractor. Fig. 2.5 shows the noticeably improved error measurements with the corrected rms map.

Although MAG_AUTO (derived from flux in a flexible Kron-like elliptical aperture) generally gives the best estimate of the magnitude irrespective of the settings, it still underestimates the magnitudes for faint objects. On the other hand, MAG_ISO computes the magnitude in an isophotal area roughly the same shape as

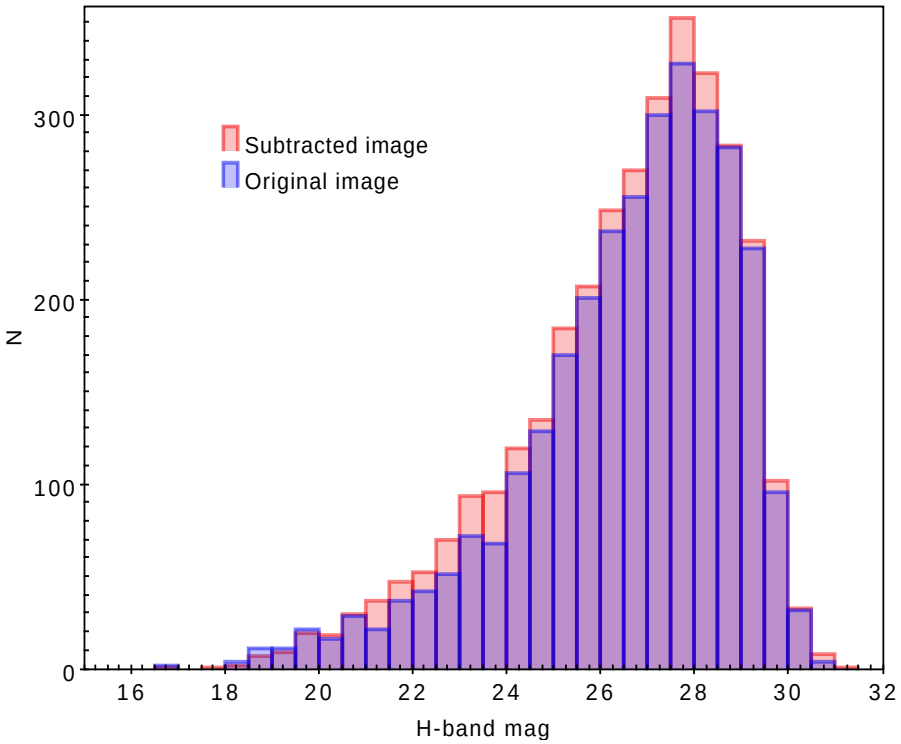


Figure 2.6: Comparison of detections in the original H-band image and the subtracted H-band image for the MACSJ0416 cluster. The subtraction procedure has enhanced the detection of faint sources in the cluster field by ~ 8 per cent.

the object, and when using separate detection and photometry images, gives you the most accurate colours (Bertin & Arnouts, 1996). Following previous work (e.g., Galametz *et al.* 2013; Guo *et al.* 2013) we therefore adopt MAG_ISO magnitudes in our analysis. Since our aim is to detect faint galaxies at $z \geq 6$, we employ a detection strategy with following SExtractor parameters: *DETECT_MINAREA* 4 pixels, *DETECT_THRESH* 0.7, *DEBLEND_NTHRESH* 64 and *DEBLEND_MINCONT* 0.0001. We employ the same method on the parallel field, with the exception of subtraction procedure, as there are no bright foreground galaxies in the parallel field. To analyze how much our subtraction procedure has enhanced the detection of faint sources in the cluster field, we run SExtractor with the same parameters on the original H-band image of MACSJ0416 cluster. We detect 3051 objects in the original H-band and 3293 objects in the subtracted H-band, showing that the subtraction procedure has enhanced the detection of faint sources in the cluster field by ~ 8 per cent (See Fig. 2.6).

In order to compute stellar mass from SED fitting, we need to estimate the total flux in all the bands. For this, we use the same approach as Guo *et al.* (2013), and first derive an aperture correction to total flux for each source in H-band as aprcor = FLUX_AUTO_F160W/FLUX_ISO_F160W. We then convert the

SExtractor isophotal fluxes and their uncertainties into μJy first and then into total fluxes and uncertainties as:

$$\text{FLUX_TOTAL} = \text{aprcor} \times \text{FLUX_ISO} \tag{2.4}$$

$$\text{FLUXERR_TOTAL} = \text{aprcor} \times \text{FLUXERR_ISO} \tag{2.5}$$

However, the caveat here is that we assume MAG_AUTO as a proxy for total magnitude, which is well known for underestimating the flux and it tends to get even worse at faint magnitudes (e.g., Franceschini *et al.* 1998; Graham & Driver 2005). To investigate this, we compare the values of MAG_AUTO estimated through simulations above with the input magnitude. Fig. 2.7 shows the results of these simulations showing the mean difference between the input magnitude and recovered MAG_AUTO magnitude in bins of $\Delta m = 0.5$ confirming that MAG_AUTO underestimates the flux by as much as $\sim$65 per cent at the faintest magnitudes. Nevertheless, previous works (e.g., Benitez *et al.* (2004) have shown that MAG_AUTO still gives the best approximation (as compared to MAG_ISO or MAG_BEST) for the total magnitudes of objects. We therefore adopt MAG_AUTO for our analysis but note that our total fluxes are likely underestimated for the faintest objects.

Finally, we build a catalog of total fluxes and the associated uncertainties that combines the photometry of the MACS0J416 cluster and the parallel field.

2.3.3.2 K_s band and Spitzer images

We also include longer wavelength K_s band and *Spitzer* data in our multiwavelength photometry catalog for reasons mentioned in 2.2.2 and 2.2.3. However, extracting accurate photometry from low resolution images ($\sim 1\farcs8$ FWHM PSF of *Spitzer* as opposed to $\sim 0\farcs18$ FWHM of WFC3) is challenging because the sources are severely blended (See Fig. 2.8), rendering aperture photometry and PSF fitting photometry unreliable. Also, PSF matching from *HST* to *Spitzer* data is not necessarily the best solution because we are then effectively throwing away all the useful spatial information from *HST* when we smooth it out.

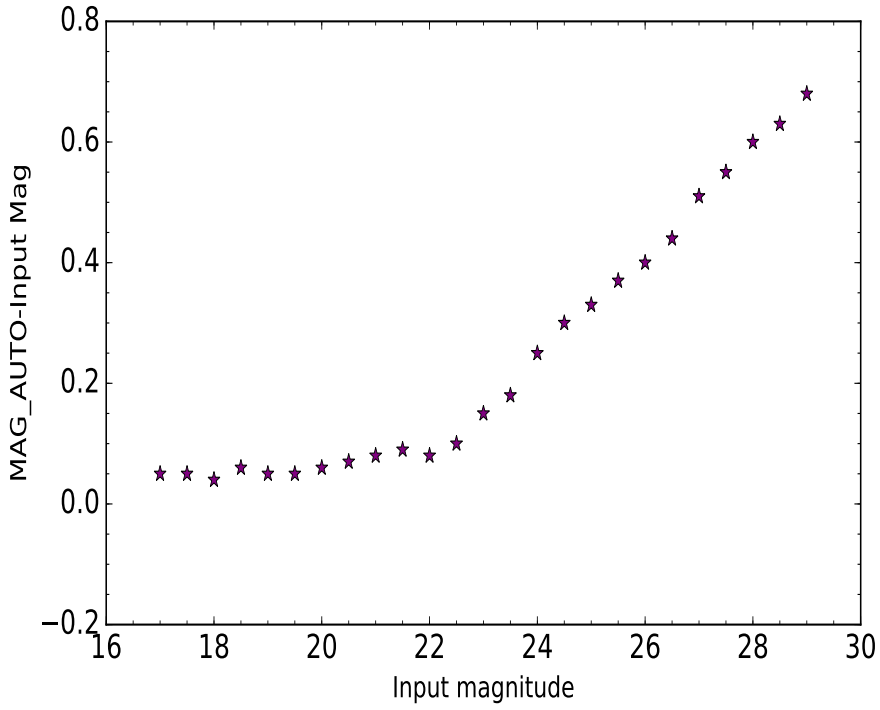


Figure 2.7: Results of our simulations, showing the mean difference between the input magnitude and recovered MAG_AUTO magnitude as a function of input magnitude in bins of $\Delta m = 0.5$. MAG_AUTO underestimates the flux by as much as $\sim$65 per cent at the faintest magnitudes.

Figure 2.8: IRAC 3.4 μm and 4.5 μm imaging of the MACSJ0416 cluster. Top left: Example of severely blended sources in IRAC channel 1 low resolution image. Top right: Residual image from T-PHOT. Bottom left: Original IRAC channel 2 image. Bottom right: Residual image from T-PHOT.

To overcome these issues, we perform photometry on the K_s band and *Spitzer* imaging using the T-PHOT code (Merlin *et al.*, 2015), built on TFIT (Laidler *et al.*, 2007) and CONVPHOT. T-PHOT is a software designed to use information from the high resolution image (such as source positions and morphologies), and use this information as priors to measure fluxes in the low resolution image. T-PHOT uses a combination of input priors such as:

1. a list of sources to obtain cutouts from the high resolution image.
2. analytical models from codes such as GALFIT.
3. unresolved, point-like sources.

In our study, we use the first method, which uses the true high resolution priors. First, a list of source positions is obtained by SExtractor in order to obtain the high resolution cutouts of the sources as priors. The priors are then convolved with a suitable convolution kernel in order to degrade them to the resolution of the low resolution image. These low resolution (normalized) model templates are then placed at appropriate positions given by the high resolution image source catalogue and scaled by a χ^2 minimization technique to give the measured fluxes of sources in the low resolution image (see Merlin *et al.* 2015 for more details).

Several steps had to be performed before running T-PHOT as explained below:

1. The units of IRAC images are in MJy/sr, whereas the units of K_s band are in counts/s. We first convert all the low resolution images to the same flux units of μJy so that the fluxes from T-PHOT can be directly fed to the photometric redshift fitting code EAZY (Brammer, van Dokkum & Coppi, 2008).
2. Since the resolution of IRAC is about 10 times lower than that of F160W, we use the IRAC PSF itself as the kernel to convolve the F160W images. We assume that the actual kernels would not be so different from the IRAC PSFs. For K_s band images, however, we run IRAF/PSFMATCH to compute the kernel. We derive empirical PSFs for both IRAC and K_s band via neighbor-masked median-scaled stacks of isolated stars.
3. T-PHOT requires that the lower resolution image (as well as the rms maps) be at the same orientation as the high resolution image. We therefore resample all IRAC and K_s band images and the rms maps to the F160W pixel scale of $\sim 0\farcs06$ and reproject to *HST* astrometry using SWarp (Bertin *et al.*, 2002).

To correct the spatial distortion/misregistration and to obtain more astrometrically precise results, we run T-PHOT in two passes. The first pass cross-correlates the model image and the low resolution image to compute the shifts and build a new set of kernels for regions under consideration. The second pass uses these shifted kernels to reduce the misalignment between the templates and low resolution images to obtain more precise results (see Merlin *et al.* 2015).

The accuracy of this procedure with T-PHOT on IRAC images is illustrated in Fig. 2.8. A comparison between the original image and the residual image demonstrates that T-PHOT does a remarkably good job at fitting sources in the low resolution image, with the exception of the very bright sources in the cluster. We notice that if the bright sources lie close to the faint sources, then their residuals affect the photometry of nearby faint sources significantly. For example, for such faint sources the S/N was significantly high (or negative) in the output catalogue generated by T-PHOT even if those faint sources were physically absent in the low resolution IRAC image (e.g., Song *et al.* 2016 have noticed the same effect). We found that such contaminated sources caused some unfortunate high-z solutions. T-PHOT helps to identify unreliable measurements for sources, especially contaminated from neighbours, with the help of a flag designated as "c_i", the covariance index flag and suggests users to treat sources with $c_i > 1$ with caution (see Merlin *et al.* 2015). Fig. 2.9 shows the values of covariance index as a function of estimated fluxes in IRAC 3.4 μm in the MACSJ0416 cluster. Out of 3293 sources in our catalog, 527 (16 per cent) objects have $c_i > 1$. We therefore visually inspected each of these sources carefully to ensure that their photometric measurements are reliable.

2.3.4 Photometric redshifts and source selection

2.3.4.1 Photometric redshifts

As mentioned in Chapter 1, there are two widely used methods for computing photometric redshifts – i) The Lyman Break (LB) (Steidel *et al.*, 1996c) also known as the "drop-out" technique that relies on the large break in the continuum flux from an object in bands blueward of the Lyman break and two-color selection in bands redward of the break, and ii) Template fitting method in which photometric redshifts are derived by fitting synthetic template spectra to the observed photometry. There are several codes, such as HYPERZ (Bolzonella, Miralles & Pelló, 2000), EAZY (Brammer, van Dokkum & Coppi, 2008), BPZ (Benitez, 2000), LePHARE [4] (Arnouts & Ilbert, 2011) in place that use their own methods to calculate

[4]http://www.cfht.hawaii.edu/ arnouts/LEPHARE/lephare.html

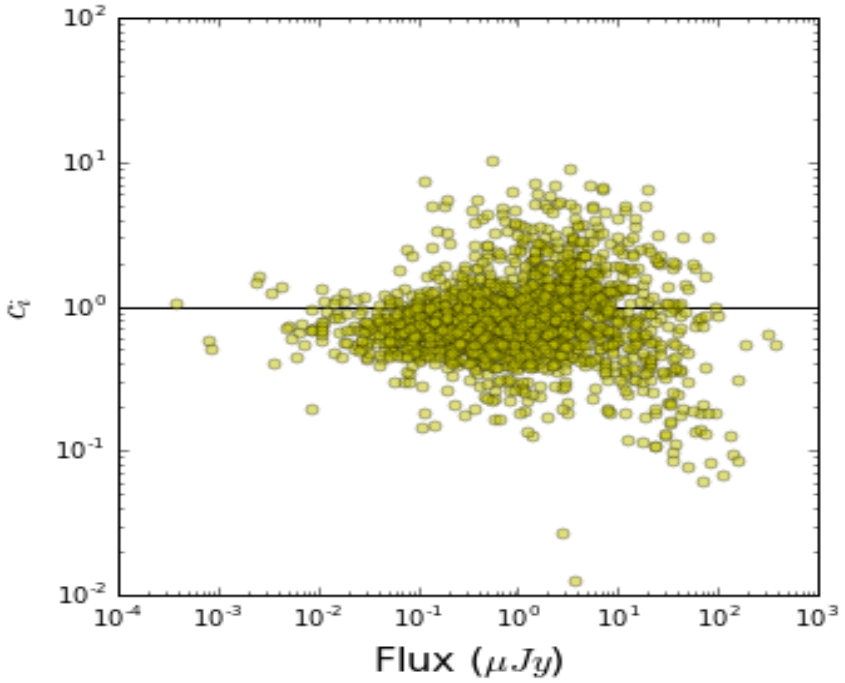


Figure 2.9: Covariance index c_i as a function of measured fluxes from T-PHOT for the MACSJ0416 cluster. 527 (16 per cent) sources from our catalog lie above $c_i > 1$ and are treated with caution.

photometric redshifts.

By providing a critical assessment of photometric redshift methods Dahlen *et al.* (2013) have shown that there is no specific code or set of template SEDs that result in significantly better photometric redshifts in comparison to others. However, they find that the codes that produce the lowest scatter and outlier fraction utilize a training sample to optimize photometric redshifts such as by adding zero-point offsets, template adjusting, or extra smoothing errors. In our work, we determine the photometric redshifts for our multiwavelength catalog using EAZY (Brammer, van Dokkum & Coppi, 2008). For this, we first calibrate the photometric redshifts by using the CANDELS dataset trimmed down to the filters we have in the HFF and use those to optimise EAZY parameters, which could then be applied to our data. We use the default reduced template set provided with EAZY, based on the PEGASE stellar population synthesis models of Fioc & Rocca-Volmerange (1997), which includes contribution from emission lines, and also an additional template based on the spectrum of Erb *et al.* (2010) that includes features such as strong optical emission lines and a high Lyα equivalent width; characteristics peculiar to young, unreddened, low-metallicity galaxies at high redshift, similar to Duncan *et al.* (2014). We choose not to include a magnitude based prior when calculating

redshifts due to the large uncertainties present in the H-band luminosity function at high redshifts (Henriques *et al.*, 2012).

2.3.4.2 Sample selection criteria

After computing photometric redshifts, we construct a sample of galaxies in the redshift range $5.5 \leq z \leq 9.5$. To do this, instead of simply relying on the best-fit redshift value, we take advantage of the full redshift probability distribution function (PDF) ($P(z) \propto \exp(-\chi^2/2)$, using the χ^2 distribution from EAZY, similar to previous work (e.g., Finkelstein *et al.* 2012, 2015; Duncan *et al.* 2014). We then form galaxy samples in four redshift bins centered at z $\sim$ 6, 7, 8, and 9 with $\triangle z$ = 1, for both the MACSJ0416 cluster and the parallel field, by applying a set of additional selection criteria following Duncan *et al.* (2014) as:

$$\int_{z_\mathrm{s}-0.5}^{z_\mathrm{s}+0.5} p(z)dz > 0.4 \tag{2.6}$$

$$\int_{z_\mathrm{p}-0.5}^{z_\mathrm{p}+0.5} p(z)dz > 0.6 \tag{2.7}$$

$$(\chi^2_\mathrm{min}/N_\mathrm{filters} - 1) < 3, \tag{2.8}$$

where z_s = 6, 7, 8 and 9 for the respective bins and z_p is the primary redshift peak.

With the first criterion we ensure that a significant area of the PDF occupies the redshift range of our interest. The second criterion ensures that at least 60 per cent of the PDF lies under the peak of the distribution, making sure if the high-redshift solution is picked, then it is the dominant one. With the third criterion we ensure that EAZY provides a reasonable fit. In addition to the above three criteria, we also place a S/N cut such that S/N(J_{125}) > 3.5 and S/N(H_{160}) > 5. This ensures the secure detection of candidates in primary filters with very high significance, excluding spurious detections.

Once we have the sample of high-redshift candidates in each redshift bin for both the cluster and the parallel field, we inspect each object thoroughly to eliminate the potential contaminants such as stars, stellar diffraction spikes, sources at the edge of the images, sources with flagged photometry etc. For example, cool dwarf stars can contaminate the high redshift sample as they can have very similar colours (e.g.,

McLure *et al.* 2006; Stanway *et al.* 2008). However, the high resolution of HST makes it possible to distinguish between galaxies and stars by considering if the object is extended or point-like. Similarly, the number densities of brown dwarfs are expected to drop-off at J_{125} magnitudes fainter than $\sim 24 - 25$, while the number density of high-redshift galaxies increases (e.g., Bowler *et al.* 2015). This is such that in small area surveys like the HFF, the number of such contaminants is considered to be negligible.

Our final samples then contains 134 galaxies: 82 in the MACSJ0416 cluster, and 52 in the parallel field, out of which, 92 are at $z \sim 6$, 24 are at $z \sim 7$, 10 are at $z \sim 8$ and 8 are at $z \sim 9$ (cluster and parallel field combined), as shown in Fig. 2.10.

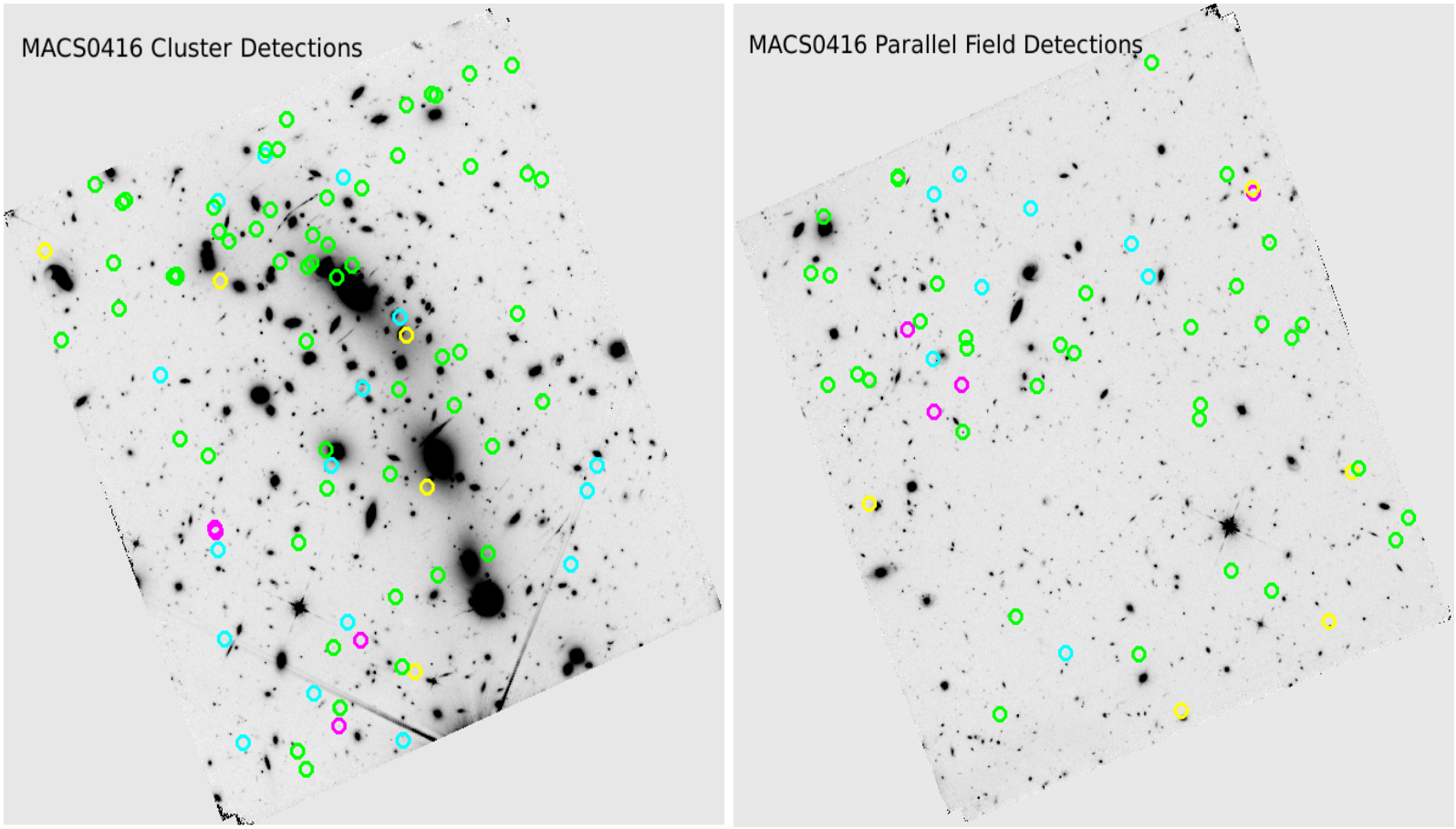


Figure 2.10: H-band image of the MACSJ0416 cluster (left) and the parallel field (right). The positions of our high-z galaxy sample at $z = 6, 7, 8$ and 9 are shown by green, cyan, yellow, and magenta circles, respectively.

In order to do comparisons between our estimated photometric redshifts and available spectroscopic redshifts, we use the published redshift catalog of MACSJ0416 cluster from the combination of the VIMOS CLASH-VLT campaign (Balestra *et al.*, 2016) and the MUSE spectroscopic study presented in Caminha *et al.* (2017) (VLT programme IDs 186.A-0798, 094.A-0115(B), 094.A-0525(A)). We match our photometric redshifts catalog and the spectroscopic redshifts catalog within 1 arcsec and include only those redshifts with QualityFlag = 3, 4, 5 and 9. Following Dahlen *et al.* (2013), we define outliers as $|\Delta z/(1+z_{\rm spec})| \geq 0.15$, where $\Delta z = (z_{\rm spec} - z_{\rm phot})$. After excluding the outliers, we compute $\Delta z/(1+z_{\rm spec})$ and find $\sigma_{\Delta z/(1+z_{\rm spec})} = 0.041$. The comparison between photometric and spectroscopic redshifts for the MACSJ0416 cluster are shown in Fig. 2.11.

2.3.4.3 Comparison of $8.5 \leq z \leq 9.5$ sample with previous work

Following the comparison of our photometric redshifts with available spectroscopic redshifts, we now compare our sample of high redshift candidates with previous studies. While the number counts of our lower redshift sources are in general agreement with previous work such as Livermore, Finkelstein & Lotz (2017), given the strong interest in the very high redshift candidates, in this section we only directly compare our highest redshift sample at $8.5 \leq z \leq 9.5$ with previous works of Laporte *et al.* (2015), McLeod, McLure & Dunlop (2016) and Castellano *et al.* (2016) who study MACSJ0416 and its parallel field using all the bands (*HST*, VLT and IRAC) available for the HFF.

Laporte *et al.* (2015) report four candidates at $z \sim 8$ behind the MACSJ0416 lensing cluster. Our results are in excellent agreement with theirs, in that we are able to recover all four of their sources in our work (our IDs 126, 1040, 1065, 393, See Appendix A), and the photometric redshift estimates agree within the error bars. McLeod, McLure & Dunlop (2016) furthermore report two sources (their HFF2C-9-3 and HFF2C-9-5) in addition to the three sources (so five in total) found by Laporte *et al.* (2015) (their Y1, Y2, and Y4) at $z \sim 8.4$. However, these two sources are rejected in our defined selection criteria (See Section 2.3.4.2) and are therefore not included in our sample. Examining the parallel field, McLeod, McLure & Dunlop (2016) report five candidates at $z \sim 8.4$ and we recover three of these (Ours IDs 1524, 1957 and 2660) with the correct photometric redshifts within the error bars. However, their HFF2P-9-2 and HFF2P-9-5 sources get rejected in our defined selection criteria.

Finally, we compare our detections with Castellano *et al.* (2016) who determine the photometric redshifts of their high-z sample from the ASTRODEEP catalog

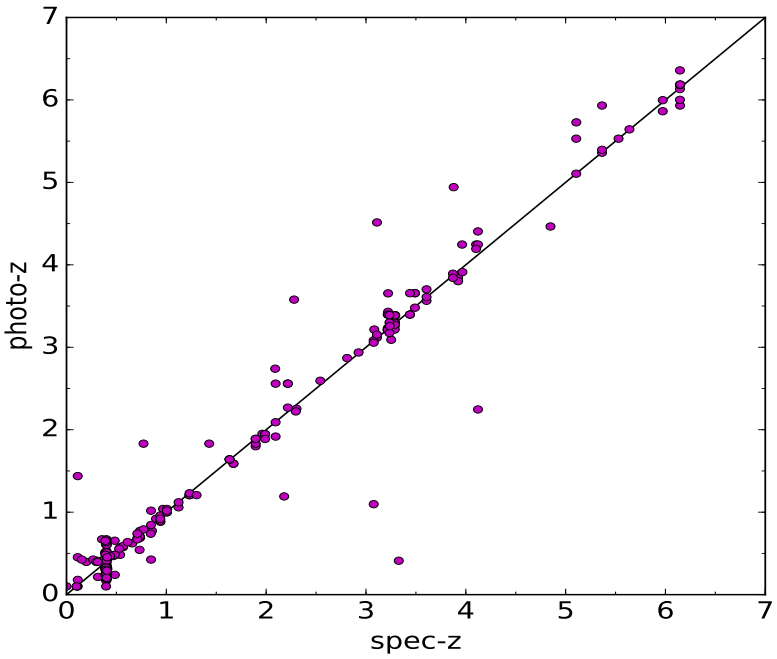


Figure 2.11: Photometric redshift and spectroscopic redshift comparison for sources in our catalog for the MACSJ0416 cluster with spectroscopic redshifts from the published redshift catalog of the MACSJ0416 cluster from the combination of the VIMOS CLASH-VLT campaign (Balestra *et al.*, 2016) and the MUSE spectroscopic study presented in Caminha *et al.* (2017).

(Merlin *et al.*, 2016) constructed by subtracting the massive galaxies in the cluster, similar to this work. They report four sources at $8.5 \leq z \leq 9.5$ in the MACSJ0416 cluster and we are able to recover two of them (their ID 99 and 743, our IDs 126 and 1065). Of the other two sources, one source (their ID 2385, which is their HFF2C-9-3 in McLeod, McLure & Dunlop (2016)) is rejected in our sample selection criteria and the other source (their ID 538 reported at $z = 8.7^{+3.6}_{-3.6}$) appears to be a possible low-z interloper at $z = 0.27^{+1.581}_{-0.143}$ based on our analysis. In addition, Castellano *et al.* (2016) report eight candidates at $z \geq 9.5$ in the MACSJ0416 cluster, out of which five appear to be possible noisy detections, one appears to be a potential low-z interloper (at $z = 0.14^{+0.001}_{-0.037}$ in our analysis), and the other two (their IDs 2362 and 2543) get rejected in our sample selection criteria, and therefore we are not able to recover any of their reported sources. In the parallel field, Castellano *et al.* (2016) find seven sources at $8.5 \leq z \leq 9.5$. We recover two of these (their ID 1272 and 1656, our IDs 1524 and 1957), while three of these sources get rejected by our sample selection criteria, and two appear to be potential low-z interlopers at $z = 1.51^{+0.943}_{-0.70}$ and $z = 0.654^{+0.044}_{-0.135}$ respectively in our analysis. Lastly, they report two candidates at $z \geq 9.5$, one of which appears to be a possible noisy detection in our analysis, and the other one again seems to be a potential low-z interloper at $z = 2.22^{+7.437}_{-0.374}$. However, because of the large uncertainty on the photometric redshift, it is difficult to ascertain the exact nature of this source.

2.3.5 Completeness simulations

Completeness correction helps us better constrain the low-mass end of the GSMF as well as the faint-end of UV LF. However, an overcorrection can lead to an artificial steepening of slope. We therefore perform an extensive set of simulations to estimate the completeness of our high-redshift sample by accounting for both the image incompleteness and the sample selection effects.

The gold standard way of doing this is by inserting 1000s of mock galaxies into the imaging data and perform the same analysis for source detection and recovery, photometric redshift estimation and sample selection as for real data. This can be separated into two parts: a) completeness from the method used to extract the objects – Here we insert 1000s of fake galaxies to a blank image in the source place, assuming different intrinsic source sizes, positions and magnitudes, and attempt to recover them with the same SExtractor parameters as for building the original catalog, and b) selection efficiency of an object in a given sample of particular redshift because of the employed selection criteria – This involves calculating the photometric redshifts of a sample of galaxies and passing them through the same

sample selection criteria as our real catalog and estimating their recovery fraction, which is then folded into completeness from part a).

2.3.5.1 Detection completeness

This is determined by inserting thousands of synthetic sources in the detection image (H-band in our case) and attempting to recover them with the same SExtractor parameters as used for building the original catalogue.

For this, we first make an artificial list of galaxies using the IRAF/GALLIST function. GALLIST produces a list of x and y coordinates, magnitudes, morphological types, half-light radii, axial ratios, and position angles for a sample of galaxies based on user defined input. Various studies have looked into the evolution of sizes of galaxies at high-redshift. For example, Grazian *et al.* (2012) and Ono *et al.* (2013) have found that faint galaxies at $z > 7$ have extremely small half-light radii of $0.3 - 0.5$ kpc. Kawamata *et al.* (2015) report the detection of a few lensed galaxies at $z \sim 6 - 8$ in Abell 2744 with sizes as small as 0.08kpc. More recently, Bouwens *et al.* (2017a) have shown that the detection of highly magnified galaxies as a function of shear is highly dependent on galaxy sizes. With the help of simulations, they have demonstrated that only the most compact galaxies can be detected in high-shear regions, indicating that extremely faint $z \sim 2 - 8$ galaxies have near point-source profiles, resulting in smaller completeness corrections and hence shallower faint-end slopes than reported in recent HFF studies.

To quantify this, we perform our completeness simulations with two different methods: i) Prompted by previous work such as Ferguson *et al.* (2004), Grazian *et al.* (2011) and Oesch *et al.* (2010), we draw galaxy sizes from a log-normal distribution of mean = 0.15 arcsec and $\sigma = 0.075$, and ii) With galaxies having near point-source profiles i.e., unresolved point sources. For both the methods, the Sérsic indices are chosen from a log-normal distribution in the range $0.5 \leq n \leq 4.0$ with the majority of the galaxies having disc-like morphologies with $n \leq 2$ (Ravindranath *et al.*, 2006), whereas the position angle is selected from a uniform distribution between 0° and 360°. The axial ratio we use is also lognormal with a peak at 0.8 and the H-band magnitudes range from $21 < H < 35$. In each iteration of the simulation, the redshift is selected from a uniform distribution of $z = 5 - 10$. To avoid confusion due to excessive number of sources, and also due to blending with nearby sources in the field, we insert only 200 fake sources in each iteration.

The next step is to insert the mock sources in the source plane and incorporate the effect of lensing on them. Selecting the galaxy positions randomly in the source plane and then lensing them back to the image plane caused the sources to fall out

of the edge of the image. We therefore choose the galaxy positions randomly in the image plane and then use IRAF/MKOBJECTS function to insert fake sources to a blank image at those positions in the source plane. This image is lensed back to the image plane using LENSTOOL (Jullo & Kneib, 2009; Jullo *et al.*, 2007; Kneib, 1993) with the help of the latest lens models by the Sharon team (Johnson *et al.* 2014) made available to the Frontier Fields project[5]. The image is then convolved with the H-band PSF after its been transformed to the image plane; convolving it before the transformation made the galaxies look much bigger than they should. SExtractor is then run on this convolved image to recover the lensed galaxies and the parameters such as magnitudes, positions, half-light radii etc are stored in an input catalog. These lensed, fake sources are then added to the subtracted H-band image and SExtractor (with the same parameters as used for building the original catalog) is used to recover them and to construct a new catalog. Finally, this catalog is matched to the input catalog with fake sources within a $\sim 0\farcs2$ matching radius.

We repeat the above process 2000 times and ultimately combine the results to calculate the recovery fraction as a function of position, input magnitude and profile type. The same process was repeated for the parallel field, with the exception of the lensing equations.

Fig. 2.12 shows the recovery fraction as a function of input magnitudes for the MACSJ0416 cluster and the parallel field both with disc-like profile galaxies and unresolved point sources. As expected, we find that with point sources the completeness goes deeper. On the other hand, not all the sources are not recovered even at brighter magnitudes due to confusion and blending with nearby sources.

2.3.5.2 Selection function

To determine the selection function efficiency, we build a custom mock catalog of high redshift galaxies using the Theoretical Astrophysical Observatory (TAO) (Bernyk *et al.*, 2016). The TAO is an online cloud-based virtual laboratory that allows web based access to mock observations of extragalactic survey data. To build our mock photometry catalog, we use the existing CANDELS mock cone from redshift $z = 0$ to $z = 9$ on the TAO and generate SEDs from the single stellar populations of Bruzual & Charlot (2003), using the initial mass function (IMF) of Chabrier (2003). Dust is then applied using the dust model of Calzetti *et al.* (2000) and the final catalog is made with a H-band distribution of magnitudes in the range $21 < H_{160} < 35$, such that the magnitudes in the rest of the filters are determined based on the range of H-band magnitudes.

[5]https://archive.stsci.edu/prepds/frontier/lensmodels/

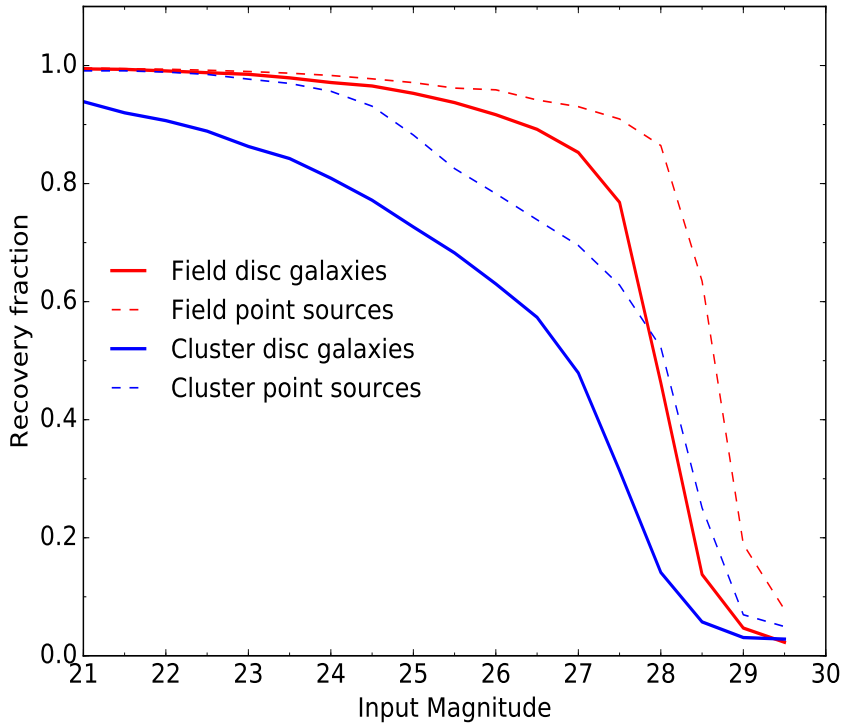


Figure 2.12: Recovery fraction as a function of H-band input magnitude for unresolved point-like (blue and red dashed lines for cluster and field respectively) and disc-like sources (solid blue and solid red line for cluster and field respectively) in the MACSJ0416 cluster and the parallel field.

In order to generate errors for the mock photometry catalog, we bin the fluxes of sources from our real catalog and calculate the standard deviation and mean of the flux errors in those bins, giving us a Gaussian distribution of the errors. Photometric errors for each filter in the mock catalog were then simulated by picking random errors each time from the Gaussian distribution in the corresponding bins. Furthermore, we ensure that the colors of the mock galaxies are a sufficiently close representation of the colors of real galaxies in our sample. For eg., at $z = 9$, our catalog had brighter galaxies as compared to the mock catalog. Therefore, as there were not enough bright galaxies intrinsic to the catalog, we rescaled the faint sources of the mock catalog to the magnitudes we need so that the mock data samples our real data very well (See also Duncan *et al.* (2014) who use CANDELS mock cones and compare the color distributions of the sources). Following these steps, we run EAZY on this mock catalog and compute the photometric redshifts.

Finally, to determine the selection efficiency for each of the redshift bins, we pass the high redshift sources from the mock catalog through the same sample selection criteria (See Section 2.3.4.2) as our real sample. From this, we measure the fraction of simulated galaxies that pass the selection criteria. This is then folded into the detection completeness computed in Section 2.3.5.1. Fig. 2.13 shows the selection efficiencies for the MACSJ0416 cluster.

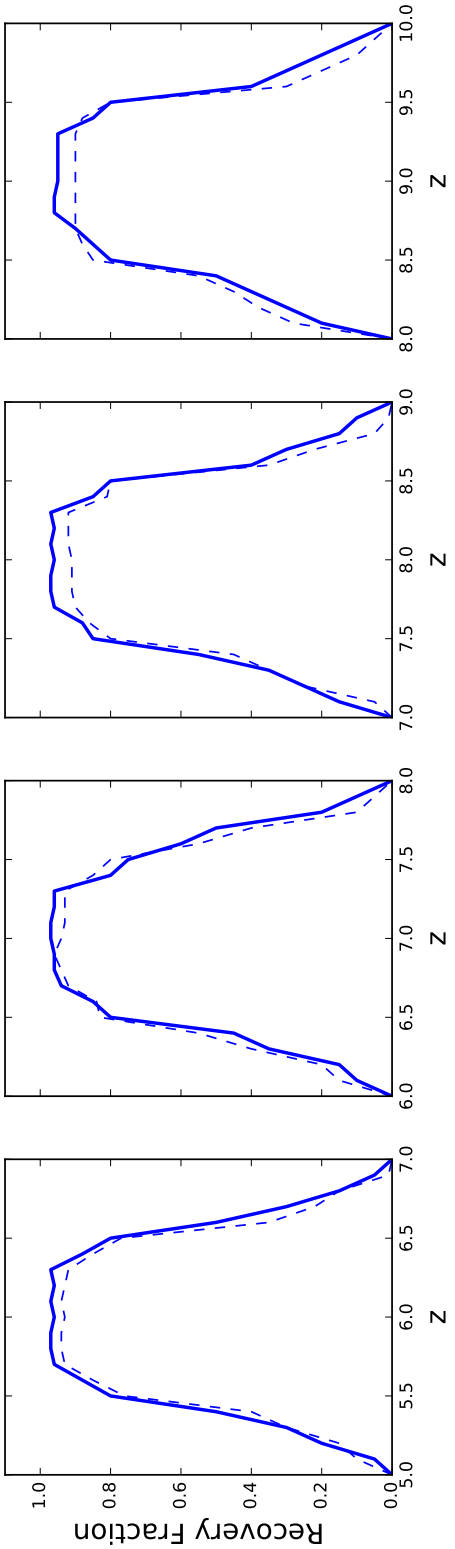


Figure 2.13: Selection efficiencies for the MACSJ0416 cluster, showing recovery fraction as a function of redshift and input magnitude. The solid line is for objects with $H_{160} = 25$ and the dashed line is for $H_{160} = 27$, finding very similar results.

2.3.6 Stellar masses, rest-frame magnitudes and star formation rates

2.3.6.1 Stellar masses and rest-frame magnitudes

To examine the evolution of the GSMF and UV LF from $z = 6-9$, we first estimate the stellar masses and rest-frame magnitudes for our sample in different redshift bins for both the cluster and the parallel field using a stellar population fitting technique described in detail in Duncan *et al.* (2014).

Briefly, we compute the stellar masses and rest-frame magnitudes using a custom template-fitting routine **SMpy**[6] (Duncan *et al.*, 2014), which matches the observed SED of each source to one of the models it generates. First, single stellar population models of Bruzual & Charlot (2003) are used to generate synthetic SEDs for a user-defined combination of parameters such as metallicity, age and star formation history (SFH), assuming a Chabrier IMF (Chabrier, 2003). The ages are allowed to vary from 5 Myr up to the age of the Universe at the redshift step being fit, dust attenuation is varied in the range $0 \leq A_v \leq 2$, and metallicities of 0.02, 0.2 and 1 $Z_\odot$ are used. The widely adopted parametrization of the SFH (SFR $\propto e^{-t/\tau}$) is used with $\tau = 0.05, 0.25, 0.5, 1, 2.5, 5, 10, -0.25, -0.5, -1, -2.5, -5, -10$ and 1000 (constant SFR) Gyr, (similar to Duncan *et al.* 2014), where negative τ values represent exponentially increasing histories.

Galaxy properties such as age, mass and star formation rate deduced from SED fitting are affected to different degrees depending on the inclusion (or not) of nebular emission. Schaerer & de Barros (2012) discussed the importance of accounting for nebular emission in the SEDs of high redshift galaxies while analysing a large sample of Lyman break galaxies from $z \sim 3-6$ and found that the majority of objects were better fit with SEDs that include nebular emission, irrespective of star formation history. Several other studies have also shown that significantly younger ages and lower masses could be obtained when nebular emission lines are included in SED fitting (e.g., Schaerer & de Barros 2009, 2010; Ono *et al.* 2010; McLure *et al.* 2011; Duncan *et al.* 2014). It has therefore become evident that nebular emission must be taken into account while understanding the photometric measurements of the SEDs of star-forming galaxies at high redshift.

Hence, we apply nebular emission lines on the model SEDs in this work, assuming an escape fraction of $f_{\rm esc} = 0$ (See Duncan *et al.* 2014 for a detailed description of the method for including nebular emission lines). Dust extinction is then applied using the law described by Calzetti *et al.* (2000). We then redshift each model SED

[6] https://github.com/dunkenj/smpy

in the range $0 \leq z \leq 11$ in steps of $\triangle z = 0.02$ and apply the attenuation by neutral hydrogen according to Madau (1995). Finally, each model spectrum is convolved through the photometric filters and the resulting SED grid is fit to the observed photometry. For each model, we compute the absolute magnitude at 1500 Angstrom by fitting a 100 Å-wide top-hat filter centered on 1500 Å. The model SEDs are fitted to the observed photometry using a Bayesian-like approach, resulting in a likelihood distribution of stellar mass and rest-frame magnitudes. The stellar masses and rest-frame magnitudes thus are computed by summing the likelihoods.

The uncertainties of the stellar masses and rest-frame magnitudes are computed via a Monte Carlo analysis. For this, the observed flux of each source was perturbed by randomly choosing a point from a Gaussian distribution with standard deviation equal to the 1σ uncertainty on the flux in a given filter. The stellar mass and rest-frame magnitude for each source is then estimated with the simulated photometry. This process is repeated 500 times and the final uncertainty is the standard deviation of the distribution of these 500 values. We employ the same method to account for errors on photometric redshifts on the estimation of stellar masses. The uncertainty due to photometric redshifts is then folded into the uncertainty from flux measurement by summing both errors in quadrature. This is then taken as the final uncertainty on stellar mass, which are found to be $\sim 0.2 - 0.3$ dex.

2.3.6.2 Star formation rates

To calculate the UV SFR, we use the rest-frame absolute magnitudes (M_{1500}) obtained from the SED fitting in Section 2.3.6.1. The absolute magnitudes are converted to UV luminosities and the Kennicutt (1998) relation that converts the UV luminosities to star formation rates is used, corrected to the Chabrier IMF (-0.24 dex) as:

$$\mathrm{SFR_{UV}(M_{\odot}yr^{-1}) = 1.4 \times 10^{-28} L_{UV}(ergs^{-1}Hz^{-1})}. \tag{2.9}$$

This, however, does not take into account the dimming of light caused by dust, which can significantly affect the measurements of SFRs. In order to study the effects of dust on the UV continuum, Meurer, Heckman & Calzetti (1999) fitted the observed UV continuum of a sample of local starburst galaxies to a power law

expressed by,

$$f(\lambda) \propto \lambda^{\beta}, \tag{2.10}$$

where $f(\lambda)$ is the observed flux density and β is the power-law index. Likewise, the UV slope (β) is measured by fitting a power-law to each model spectrum (See Section 2.3.6.1) using the 10 windows defined by Calzetti, Kinney & Storchi-Bergmann (1994) and the dust extinction is calculated using the Meurer, Heckman & Calzetti (1999) relation as:

$$A_{1600} = 4.43 + 1.99\beta, \tag{2.11}$$

which relates the UV slope β and the dust extinction at 1600 Å. This is then used to calculate the final dust-corrected SFRs ($\mathrm{SFR_{Madau}}$ hereafter).

Individual stellar population parameters such as age, dust and metallicity are degenerate in SED fits of high-redshift galaxies. In order to investigate this, we also calculate the SFRs from the SED fitting code by obtaining the SFR from the best-fitting template ($\mathrm{SFR_{Template}}$ hereafter) for each galaxy. We find that the two estimates agree well with a $\mathrm{median}(\log_{10}(\mathrm{SFR_{Madau}}) - \log_{10}(\mathrm{SFR_{Template}})) < 0.1$, with the exception of a few galaxies with the highest SFR ($\mathrm{SFR_{Madau}} > 100\mathrm{M_{\odot}yr^{-1}}$). In order to be consistent with previous works, we use $\mathrm{SFR_{Madau}}$ as estimated by the SED fitting code in this work.

2.3.7 Lensing magnification

Reliable lensing models are required in order to interpret many of the properties of background lensed galaxies accurately. For the HFF, the lens models were produced by seven independent teams for all six clusters using different methods, assumptions and software. The primary difference between the lensing models is that some assume that the cluster mass substructure is traced by the luminous cluster galaxies, while others make no assumption about light tracing mass, and their models are instead solely constrained by lensing observables, and thus probe a broader range of possible mass distributions. We refer the reader to the MAST website [7] for more details of the lensing models. Five models that assume that light-traces-mass are: CATS (Jauzac *et al.*, 2014), Sharon (Johnson *et al.*, 2014), GLAFIC (Oguri, 2010;

[7] https://archive.stsci.edu/prepds/frontier/lensmodels/

Ishigaki *et al.*, 2015), Zitrin-NFW and Zitrin-LTM (Zitrin *et al.*, 2013). The rest of the models that work without this assumption are provided by Bradac (Bradač *et al.*, 2009), Williams (Grillo *et al.*, 2015) and Merten (Merten *et al.*, 2011).

In order to demagnify the masses and the rest-frame magnitudes, we first need to compute the per pixel magnification factor. Each lens modelling team has provided maps of mass surface density (kappa), and weak lensing shear (gamma) from which magnifications at any redshift can be derived. As a first step, we regrid the gamma and kappa maps to match the *HST* pixel scale and then use these maps to calculate the magnification values at each pixel using,

$$\mu = \frac{1}{(1-\kappa)^2 - \gamma^2}, \tag{2.12}$$

where κ and γ both scale with the distance ratio D_{LS}/D_S, D_{LS} being the angular diameter distance between the source and the cluster, and D_S the angular diameter distance between the observer and the source. Finally, we calculate the median magnification value, $\mu_{\rm med}$, for all eight different lensing models in order to exclude possible outliers. This median magnification value was used to demagnify the masses and the rest-frame magnitudes for our sample in each redshift bin for the MACSJ0416 cluster (we do not demagnify the masses for parallel field).

We find that our subtraction procedure and the lensing effect allows us to probe stellar masses as low as $10^{6.8} M_{\odot}$; lower than previous studies (e.g., González *et al.* 2011; Duncan *et al.* 2014; Grazian *et al.* 2015; Song *et al.* 2016) at $z \sim 6$ (See Fig. 3.6). Similarly, we are probing masses as low as $10^{7.4} M_{\odot}$, $10^{7.8} M_{\odot}$, and $10^{8.3} M_{\odot}$ at $z \sim 7$, $z \sim 8$, and $z \sim 9$ respectively. With these methods we also find that we are able to probe magnitudes as faint as $M_{\rm UV} = -13.5$, $M_{\rm UV} = -15.5$, $M_{\rm UV} = -15.6$ and $M_{\rm UV} = -18.8$ at $z \sim 6$, $z \sim 7$, $z \sim 8$ and $z \sim 9$ respectively.

2.3.8 Number densities

2.3.8.1 Effective volume estimation

To estimate the volume for our luminosity and mass functions we use the enhancement of the $1/V_{\rm max}$ method (Schmidt, 1968) introduced by Avni & Bahcall (1980) and treat our high redshift samples as a "coherent" sample (nomenclature of Avni & Bahcall (1980)) including the cluster and the parallel field with their corresponding depths, following Avni & Bahcall (1980), Eales (1993), Ilbert *et al.* (2005) and Duncan *et al.* (2014).

Strong gravitational lensing with massive clusters enable the detection of faint galaxies by providing a magnified boost to the light from background sources. However, the disadvantage is that a high magnification region will essentially reduce the survey volume. To account for this, we calculate the maximum observable comoving volume in which a galaxy can remain detectable as:

$$V_{\rm obs,i} = \sum_{k}^{N_{\rm fields}} \int_{z1,k}^{z2,k} \frac{{\rm d}V}{{\rm d}z} f(z, m, \mu) {\rm d}A_k(\mu, z) {\rm d}z \tag{2.13}$$

where the summation, k, is over the cluster and the parallel field with their corresponding survey area, ${\rm d}A_k$, $z_{1,k}$, $z_{2,k}$ are the integration limits, f is the completeness function, and ${\rm d}V/{\rm d}z$ is the comoving volume. For the cluster, the survey area ${\rm d}A$ is the delensed survey area in the source plane, which is a function of the magnification computed in Section 2.3.7 and redshift, whereas for the parallel field the survey area is just the survey area without the effects of lensing. Similarly, the completeness function f, which includes the corrections for incompleteness and the selection function calculated in Section 2.3.5, is a function of redshift, magnitude m and magnification factor μ for the cluster, but does not incorporate the effects of lensing for the parallel field. The integration limits are given by $z_{1,k} = z_{\rm min}$ and $z_{2,k} = \min\{z_{\rm max}, z(z_{\rm j}, m_{\rm j}, m_{\rm max,k})\}$, where $z_{\rm min}$ and $z_{\rm max}$ are the minimum and maximum redshift to which the source could be pushed and still be included in the sample (e.g. Avni & Bahcall 1980; Eales 1993; Ilbert *et al.* 2005; Duncan *et al.* 2014. The function, $z(z_{\rm j}, m_{\rm j}, m_{\rm max,k})$, gives the maximum redshift at which a source of apparent magnitude m_j, observed redshift z_j, could be observed and included in the sample given the depth $m_{\rm max,k}$ of the field/cluster. So for e.g. for the $z = 9$ sample ($8.5 < z < 9.5$), $z_{\rm min} = 8.5$ and $z_{\rm max} = 9.5$ in the case of the object being still sufficiently bright to be detected beyond this redshift.

Once we have the estimated volume, the number density in each magnitude (or mass) bin is calculated as:

$$\phi(M){\rm d}M = \sum_{i}^{N{\rm gal}} \frac{N_i}{V_{\rm obs,i}} \tag{2.14}$$

2.3.8.2 Errors on number densities

To calculate the errors on number densities, we perform a Monte Carlo analysis in which the stellar mass (or rest-frame UV magnitude) and redshift of each galaxy is

varied along a Gaussian distribution with standard deviation equal to the 1σ uncertainty of the stellar masses (or rest-frame UV magnitudes) and redshifts. We then repeat the number density calculation explained in this section on 500 simulated redshifts and stellar masses (or rest-frame UV magnitudes) to obtain simulated number densities. The standard deviation of these values then is the uncertainty due to measurement error. We then calculate the Poisson uncertainty for the number counts and add these in quadrature to the uncertainty from the simulations.

Furthermore, the choice of lensing maps impacts the magnification factor, the survey area and hence the effective volume. This can introduce large uncertainties, in particular at the very faint end of the UV LF/GSMF where magnification factors exceed $10\times$. These uncertainties can reach a factor $> 2\times$ on the selection volume as shown in Atek *et al.* (2018) and therefore needs to be accounted for. For this, we calculate the effective volume and hence the number densities explained in this section using all eight lensing models used in this study. The standard deviation of these values is then the uncertainty due to lensing maps and is added in quadrature to the uncertainties from simulations and the Poisson uncertainty calculated above, which is then taken as the final uncertainty on number densities.

2.4 Summary

In this chapter I described the method we developed to subtract the massive foreground galaxies on the critical line of the MACSJ0416 cluster and the construction of the multiwavelength catalog, from 0.4 to 4.5μm, using *HST*, *Spitzer* and ground-based VLT data. I also described the photometric redshift determination and the selection criteria used to construct our sample of high-redshift galaxies at $z = 6-9$, along with the completeness simulations undertaken to take into account the effects of completeness and selection functions. I also outlined the SED fitting method used to estimate the stellar masses, rest-frame UV magnitudes and star formation rates for our high redshift sample. I concluded this chapter describing the method used for the estimation of volume (and hence number densities) including the effects of lensing, required for luminosity and mass functions. Our primary results are as follows:

1. Our subtraction method allows for a deeper and cleaner detection of the faintest systems at $z \geq 6$. We find that our subtraction procedure has enhanced the detection of faint sources in the cluster field by ~ 8 per cent.

2. The construction of a multi-wavelength catalog (from 0.4 to 4.5μm) using all

the bands (*HST*, K_s and IRAC) available for the HFFs has allowed us to put better constraints on redshift estimates as well as obtain robust stellar mass estimates.

3. Our photometric redshift determination and the employed selection criteria has enabled us to construct our high-redshift sample consisting of 134 galaxies: 82 in the MACSJ0416 cluster, and 52 in the parallel field, out of which, 92 are at $z \sim 6$, 24 are at $z \sim 7$, 10 are at $z \sim 8$ and 8 are at $z \sim 9$ (cluster and parallel field combined).

4. Finally, we also find that our subtraction procedure and the strong gravitational lensing effect has allowed us to probe magnitudes as faint as $M_{\rm UV} = -13.5$, $M_{\rm UV} = -15.5$, $M_{\rm UV} = -15.6$ and $M_{\rm UV} = -18.8$ at $z \sim 6$, $z \sim 7$, $z \sim 8$ and $z \sim 9$ respectively. Similarly, it has allowed us to probe masses as low as $10^{6.8} M_{\odot}$, $10^{7.4} M_{\odot}$, $10^{7.8} M_{\odot}$, and $10^{8.3} M_{\odot}$ at $z \sim 6$, $z \sim 7$, $z \sim 8$, and $z \sim 9$ respectively.

Chapter 3

Evolution of the UV LF and GSMF

In this chapter, the evolution of the Ultra-Violet luminosity functions (UV LF) and galaxy stellar mass functions (GSMF) is investigated for the sample of our high redshift galaxies at $z = 6 - 9$ in the MACSJ0416 cluster and its parallel field derived in Chapter 2.

3.1 Introduction

As described in Chapter 1, one of the primary and popular methods for comparing and understanding galaxy evolution is to use the UV LF and to measure its evolution (e.g., McLure *et al.* 2013; Finkelstein *et al.* 2015; Bouwens *et al.* 2015b). This is largely because the UV luminosity function is the most straightforward way of measuring a galaxy property and determining how it changes with time. The UV LF, which gives the number densities of galaxies at different UV luminosities, is the simplest measure of galaxies at these redshifts, which requires the fewest assumptions. Furthermore, the rest-frame ultraviolet luminosity function (as well as the stellar mass function) allows us to answer fundamental questions about the way the first galaxies and stars formed. This is becoming even more true with the advent of specific predictions for the shape and normalization of the $z > 8$ UV LF (and GSMF).

In fact, we now have a good understanding of the amount of light emitted by these early galaxies in the rest-frame UV. We are able to measure this for galaxies at a range of luminosities and masses back to this epoch of $z \sim 7$ (e.g.,Bouwens *et al.* 2007; Oesch *et al.* 2010; Grazian *et al.* 2011; Schenker *et al.* 2013; McLure *et al.* 2013). What this reveals is that there is a gradual steepening of the UV luminosity

function as one goes back in time, such that there are more fainter galaxies per brighter galaxies as one probes from $z \sim 3$ to $z \sim 7$. This is such that there are in fact more galaxies at these earlier times than there are today, as there are so many fainter and lower mass systems (e.g., Conselice *et al.* 2016). However, the issue with UV photometry and the UV luminosity function is that these are a combination of a few physical processes. Namely, a higher star formation rate will produce a higher UV luminosity, but this does not necessarily correlate with the underlying stellar mass of the galaxy. It is easy to imagine scenarios whereby the underlying mass is high, but because of dust or a low star formation rate, the UV luminosity is not as high. Therefore, it is essential to measure the stellar mass functions as well as luminosity functions as they can be substantially different.

Whilst there is a significant amount of work done on the UV LF in these and other fields (e.g., Bouwens *et al.* 2015b; Finkelstein *et al.* 2015; McLeod, McLure & Dunlop 2016; Laporte *et al.* 2016; Livermore, Finkelstein & Lotz 2017; Atek *et al.* 2018), this reveals the ongoing star formation, while the stellar masses reveal the past formation, and is thus complementary. The stellar mass, unlike the UV luminosity, is a measure of the integrated formation and merging history of a galaxy. It includes all processes such as star formation and mergers, which contribute to building up the mass of a galaxy. In this sense, it is an excellent indicator for how galaxy formation has progressed over the epochs before it is measured, as it is the integral of all galaxy formation processes previous to the time in which we observe it. This is in contrast to the UV luminosity, which is a good, albeit affected by dust, measure of the instantaneous star formation rate of a galaxy. This is in a sense the differential of the formation process, albeit with uncertainties due to dust. UV luminosities, therefore, as such do not tell us about the past history of a galaxy or how/when it formed.

There are many other reasons to search for these early galaxies and to study their stellar masses. The first is that by pushing back in time, we can find when the very first galaxies formed and therefore understand the physical causes of that early formation. Whilst this is still not possible due to technical limitations, we are able to see galaxies when they are forming at high star formation rates back to this early epoch of around $z \sim 7-8$ and measure their stellar masses (e.g., Labbé *et al.* 2010; McLure *et al.* 2011; Oesch *et al.* 2014; Duncan *et al.* 2014; Song *et al.* 2016; Laporte *et al.* 2016).

Just as for the UV luminosity function, the stellar mass function also evolves with time, and becomes steeper with higher redshift, such that there are more lower mass galaxies per massive/bright galaxy at higher redshift than at lower

redshift (e.g., González *et al.* 2011; Duncan *et al.* 2014; Grazian *et al.* 2015; Song *et al.* 2016). The stellar masses of these galaxies allows us to probe the past star formation history to reveal, and place constraints, on when the first epochs of star formation occurred and to probe whether galaxies could have caused reionization (e.g., Duncan & Conselice 2015).

As there are so many more faint and low mass galaxies compare to massive ones, and the fact that the stellar mass function continues to be occupied by progressively lower mass galaxies, it is worth asking if, and how, this continues. At some point we may expect the mass function to turn over, such that at some mass limit we see a natural decline in the number of galaxies lower than some stellar mass limit. Stellar masses also provide information about the mass-to-light ratio of the lowest mass galaxies, which can only be probed through deep observations. Reaching these galaxies will be routine with JWST, but until then our best chance to study these systems is through deep observations of lensing clusters (e.g., Kneib & Natarajan 2011; Bouwens *et al.* 2009; Coe *et al.* 2013; Zheng *et al.* 2012; Bradley *et al.* 2014; Zitrin *et al.* 2014). In this Chapter, we therefore use the stellar masses and number densities estimated in Chapter 2 and derive the first GSMF at $z = 6 - 9$ for the Frontier Fields program.

Currently there are inconsistencies, and large uncertainties, in the best available measurements of galaxy number densities and luminosity functions at $z > 6$. One of the most intriguing recent results from the deepest existing *HST* data is that there is an apparent decline of the number of galaxies at the highest redshifts, $z \sim 6 - 11$ (e.g., Bouwens *et al.* 2016). Based on extrapolating the UV LF at lower redshifts, we should have found more systems than the candidates discovered in the deepest *HST* data (e.g., Oesch *et al.* 2013). On the other hand, deep *HST* imaging of lensing clusters in the CLASH and HFF clusters have found a significant number of $z > 6$ candidates (e.g., Atek *et al.* 2014; Livermore, Finkelstein & Lotz 2017). This includes several lensed candidates at $z \sim 9$ behind the HFFs (e.g., Zitrin *et al.* 2014). Another intriguing result from HFF studies is that the UV LF continues to remain unbroken to magnitudes as faint as $M_{\rm UV} = -12.5$ at $z \sim 6$ (e.g., Livermore, Finkelstein & Lotz 2017) and $M_{\rm UV} = -15$ at $z \sim 9$ (e.g., Ishigaki *et al.* 2018), whereas more recently Bouwens *et al.* (2017b) and Atek *et al.* (2018) have reported a turnover in the faint-end of the UV LF beyond an absolute magnitude of $M_{\rm UV} = -15$ at $z \sim 6$. In this chapter, we therefore revisit this issue by deriving the UV luminosity function from $z = 6 - 9$ with our new measurements.

3.2 Ultra-Violet luminosity function

There are many different physical processes that are responsible for the formation of the first galaxies, and thus the creation of UV light, including the metallicity of the gas and stars, the dust content and form of extinction laws, various forms of feedback, the density of gas, as well as perhaps magnetic fields. The predictions for the formation of these first galaxies can vary significantly depending on the assumptions, and the luminosity function is a powerful approach for understanding this issue, as models of its distribution are degenerate at lower redshifts, but differ significantly at higher redshifts.

Previous studies of luminosity functions at a wide range of redshifts have shown that the number densities of galaxies as a function of luminosity can be characterized by a Schechter function (Schechter, 1976) of the form:

$$\phi(L) = \Phi^*(\frac{L}{L^*})^{\alpha} \exp(-\frac{L}{L^*}). \tag{3.1}$$

The Schechter function can also be expressed in log space as,

$$\phi(M) = 0.4ln(10)\phi^* 10^{-0.4(M-M^*)(\alpha+1)} e^{-10^{-0.4(M-M^*)}}, \tag{3.2}$$

where ϕ^* provides the normalization, M^* (referred to as the knee of the Schechter function) corresponds to the characteristic magnitude at which the function turns over from a power law into an exponential form and α is the faint-end slope.

3.2.1 Best fit Schechter parameters and their uncertainties for the UV LF

Once we have the number densities (See Section 2.3.8) in each luminosity bin, we proceed to determine the rest-frame UV luminosity function at $z = 6, 7, 8$ and 9 by fitting a Schechter function as defined above to the number densities in each redshift bin.

To determine the best fit Schechter parameters and their uncertainties for the UV LF, we use a pure-Python implementation of Goodman & Weare's Affine Invariant Markov chain Monte Carlo (MCMC) Ensemble sampler (Goodman & Weare, 2010; Foreman-Mackey *et al.*, 2013) that examines the three-dimensional parameter space of Schechter parameters. For each redshift, we use 10^2 MCMC chains of

10^4 steps each to explore the full parameter space, building a distribution of $M^*_{\rm UV}$, Φ^* and α. For the priors, we limit the parameter space to $-24 < M^*_{\rm UV} < -17$, $\log(\phi^*/{\rm Mpc}^{-3}) > -8$ and $\alpha > -4$. However at $z = 9$, where the sample size is small, we fix $M^*_{\rm UV}$ to the value estimated at $z = 8$.

As a first step, we compute the likelihood function, which is simply a Gaussian, and numerically optimize it. The starting position of the chain(s) is then a small Gaussian ball around the maximum likelihood result. The chains start in small distributions around the maximum likelihood values and then they quickly diverge and start exploring the full posterior distribution. To minimize the dependence of the posterior distribution on the starting point, we discard the first 10 per cent of steps in the burn-in phase before running each chain. For our final result, we join the chains together giving a distribution of 10^6 values of Schechter function parameters at each redshift. The best-fit values for each Schechter function parameter are the median of this distribution, with the uncertainties covering the central 68 per cent of the distribution.

In order to investigate the effect of galaxy sizes on completeness corrections and hence on the faint-end slopes, we derive the best-fit Schechter parameters and their uncertainties for our UV luminosity functions in this way using the completeness curves described in Section 2.3.5, with both disc-like galaxies and point sources. Our results, along with the values from the literature, are listed in Table 3.1 and the resulting UV luminosity functions plotted along with previous work are shown Fig. 3.1. The error bars on our data points in Fig. 3.1 take into account the errors on photometric redshifts, errors on magnitudes, Poisson errors and uncertainties due to lensing maps, but does not include the errors due to cosmic variance.

To estimate the fractional uncertainty in the number densities due to cosmic variance, we use the cosmic variance calculator tool by Trenti & Stiavelli (2008) using the estimated completeness and survey area as inputs. The average excess uncertainty in the moderately lensed area (e.g., $\sim 1-10$x magnification) is typically only $10-30$ per cent higher than an equivalent blank field (Brant Robertson, private discussion). We therefore estimate the cosmic variance of our sample by computing the blank field cosmic variance and then scaling the rms cosmic variance by ~ 1.2. For the highest magnification objects, we compute the effective area and volume for their magnification and then estimate the cosmic variance as if the sources were in a blank field of that (much smaller) size. Finally, since we are observing two fields, we estimate the joint uncertainty on the combined sample by adding the uncertainties in quadrature. We find that the cosmic variance errors span from $30-90$ per cent from the low luminosity/mass end to the high luminosity/mass end in all redshift

bins. In Fig. 3.1 we show the measured error on number densities for galaxies of $M_{UV} \approx -19$.

We find through these Schechter fits that the faint-end slope α of the UV LF appears ($\sim 0.4\sigma$ significant) to become steeper at higher redshifts, such that the ratio of lower to higher luminosity galaxies increases back to where we can measure these systems. The faint-end slope α changes from $-2.03^{+0.12}_{-0.10}$ at $z = 6$ to $-2.20^{+0.51}_{-0.47}$ at $z = 9$ using disc-like galaxies in our completeness simulations. These measurements are consistent with a continuation of the trends seen from lower redshift, however we cannot rule out a constant α and more data is needed to confirm the trend at these redshifts. Bouwens *et al.* (2017a) suggest shallower faint end slopes than what has been derived in some recent studies (by $\Delta\alpha \sim 0.1 - 0.3$) when simulated galaxies for completeness have near point-source profiles. When point sources are considered in our analysis, we find that the faint-end slopes are indeed shallower ($\Delta\alpha \sim 0.09 - 0.12$, See Table 3.1) in the redshift range probed. We note that these systematic offsets in slope are less than those estimated by Bouwens *et al.* (2017a) but we can attribute this to the difference in assumed profiles for input galaxies with our broader range of assumed Sérsic indices resulting in a higher completeness for the same half-light radii (i.e. $0.5 \leq n \leq 4.0$, vs $n = 1$ for Bouwens *et al.* (2017a)). We also find a decrease in Φ^* with increasing redshift at $z = 6 - 9$, and a slight evolution in M^*_{UV} is also observed, with it decreasing with redshift from $z = 6 - 8$.

In order to show the variation due to individual lensing model, we also estimate the number densities with four lensing models of CATS (Jauzac *et al.*, 2014), Sharon (Johnson *et al.*, 2014), Bradac (Bradač *et al.*, 2009) and Merten (Merten *et al.*, 2011). Two of these models (CATS and Sharon) assume that light-traces-mass and the other two (Bradac and Merten) operate without this assumption. The resulting LFs for each redshift bin are shown in Fig. 3.2. It is seen that there is scatter between the different LFs, which is a result of different magnification factors estimated from the lensing models. However, in all the cases we observe a steeply increasing faint-end slope without any evidence of a turn over.

Finally, as shown in Fig. 2.7, since the faintest objects have their flux underestimated due to the use of MAG_AUTO in our analysis, we also investigate the implications of this on the slope of the derived luminosity functions at all redshifts. For this, we use the offset between measured magnitude with MAG_AUTO and the input magnitude in our observed distribution and refit the luminosity functions. With this we find that the faint end slopes are shallower by $\Delta\alpha \sim 0.06 - 0.07$ than reported in this work.

Table 3.1: Best fit Schechter function parameters and their uncertainties for our UV LFs. The quoted best fit values and 1σ errors of the Schechter parameters constitute the median and the central 68 per cent of posterior distribution of each parameter from our MCMC analysis. **Note**: We only show the Schechter function parameters and their uncertainties derived using a classical Schechter function fit for Atek *et al.* (2018) and Bouwens *et al.* (2017b) and do not show the values they derive with a modified Schechter function that allows for a curvature at very faint magnitudes.

Redshift	$M^*_{\rm UV}$	α	$\phi^*(10^{-4}{\rm Mpc}^{-3})$
$z\sim6$			
This work (disc galaxies)	$-20.94^{+0.31}_{-0.26}$	$-2.03^{+0.12}_{-0.10}$	$2.01^{+0.85}_{-0.60}$
This work (point sources)	$-21.00^{+0.36}_{-0.30}$	$-1.93^{+0.11}_{-0.11}$	$1.61^{+0.88}_{-0.62}$
Livermore et al. (2017)	$-20.83^{+0.05}_{-0.04}$	$-2.10^{+0.04}_{-0.03}$	$2.23^{+0.273}_{-0.100}$
Finkelstein et al. (2015)	$-21.13^{+0.25}_{-0.31}$	$-2.02^{+0.10}_{-0.10}$	$1.86^{+0.94}_{-0.80}$
Bouwens et al. (2015)	$-20.94^{+0.20}_{-0.20}$	$-1.87^{+0.10}_{-0.10}$	$5.00^{+2.2}_{-1.6}$
Bouwens et al. (2017) [a] [b]	-20.94 (fixed)	$-1.91^{+0.02}_{-0.02}$	$6.6^{+0.4}_{-0.4}$
Atek et al. (2018) [a]	$-20.74^{+0.21}_{-0.20}$	$-1.98^{+0.11}_{-0.09}$	$3.72^{+2.31}_{-1.43}$
$z\sim7$			
This work (disc galaxies)	$-20.85^{+0.40}_{-0.38}$	$-2.06^{+0.17}_{-0.15}$	$1.70^{+1.20}_{-0.70}$
This work (point sources)	$-21.04^{+0.45}_{-0.40}$	$-1.95^{+0.20}_{-0.18}$	$1.20^{+1.00}_{-0.51}$
Livermore et al. (2017)	$-20.80^{+0.06}_{-0.05}$	$-2.06^{+0.05}_{-0.05}$	$2.13^{+0.260}_{-0.188}$
Finkelstein et al. (2015)	$-21.03^{+0.37}_{-0.50}$	$-2.03^{+0.21}_{-0.20}$	$1.57^{+1.49}_{-0.95}$
Bouwens et al. (2015)	$-20.87^{+0.26}_{-0.26}$	$-2.06^{+0.13}_{-0.13}$	$2.9^{+2.1}_{-1.2}$
Atek et al. (2015)	$-20.89^{+0.60}_{-0.72}$	$-2.04^{+0.17}_{-0.13}$	$2.88^{+5.82}_{-1.86}$
Laporte et al. (2016)	$-20.33^{+0.37}_{-0.47}$	$-1.91^{+0.26}_{-0.27}$	$3.7^{+1.2}_{-1.1}$
Ishigaki et al. (2018)	$-20.89^{+0.17}_{-0.13}$	$-2.15^{+0.08}_{-0.06}$	$1.65^{+0.684}_{-0.484}$
$z\sim8$			
This work (disc galaxies)	$-20.40^{+0.52}_{-0.54}$	$-2.14^{+0.37}_{-0.32}$	$1.49^{+1.83}_{-0.83}$
This work (point sources)	$-20.58^{+0.57}_{-0.58}$	$-2.02^{+0.40}_{-0.36}$	$1.09^{+1.58}_{-0.62}$
Livermore et al. (2017)	$-20.72^{+0.18}_{-0.14}$	$-2.01^{+0.08}_{-0.08}$	$1.69^{+0.592}_{-0.439}$
Finkelstein et al. (2015)	$-20.89^{+0.74}_{-1.08}$	$-2.36^{+0.54}_{-0.40}$	$0.72^{+2.52}_{-0.65}$
Bouwens et al. (2015)	$-20.63^{+0.36}_{-0.36}$	$-2.02^{+0.23}_{-0.23}$	$2.08^{+2.3}_{-1.1}$
Laporte et al. (2016)	$-20.32^{+0.49}_{-0.26}$	$-1.95^{+0.43}_{-0.40}$	$3.01^{+8.5}_{-1.9}$
Ishigaki et al. (2018)	$-20.35^{+0.20}_{-0.30}$	$-1.96^{+0.18}_{-0.15}$	$2.5^{+1.03}_{-1.25}$
$z\sim9$			
This work (disc galaxies)	-20.40 (fixed)	$-2.20^{+0.51}_{-0.47}$	$0.98^{+1.65}_{-0.60}$
This work (point sources)	-20.58 (fixed)	$-2.11^{+0.56}_{-0.47}$	$0.55^{+1.10}_{-0.35}$
Laporte et al. (2016)	-20.45 (fixed)	$-2.17^{+0.41}_{-0.43}$	$0.70^{+0.30}_{-0.30}$
Ishigaki et al. (2018)	-20.35 (fixed)	-1.96 (fixed)	$1.31^{+0.266}_{-0.318}$
Mcleod et al. (2015)	-20.1 (fixed)	-2.02 (fixed)	$2.51^{+1.46}_{-1.39}$

[a] Using classical Schechter function

[b] Using the CATS model

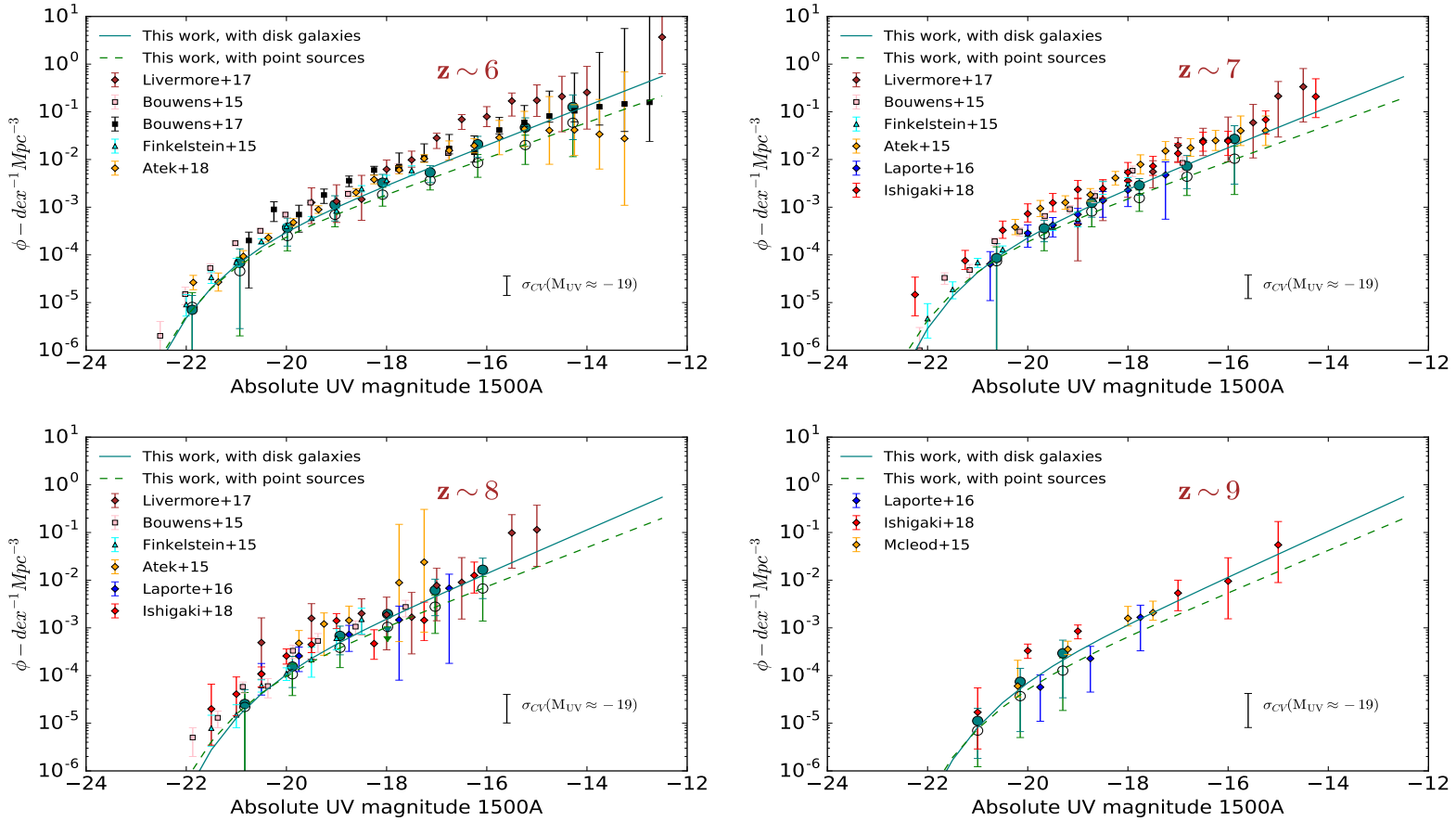


Figure 3.1: The UV LF at $z = 6 - 9$ in the MACSJ0416 cluster and its parallel field. The solid green line is our best fit Schechter function derived from the MCMC analysis to the green circles, using disc-like galaxies in completeness simulations. The dashed green line is our best fit Schechter function from the MCMC analysis to the open green circles, using point sources. The error bars on our data points take into account the errors on photometric redshifts, errors on magnitudes, Poisson errors and uncertainties due to lensing maps, but does not include the errors due to cosmic variance. The representative error bar in the bottom right corner of each plot shows the measured error on number densities for galaxies of $M_{UV} \approx -19$ due to cosmic variance.

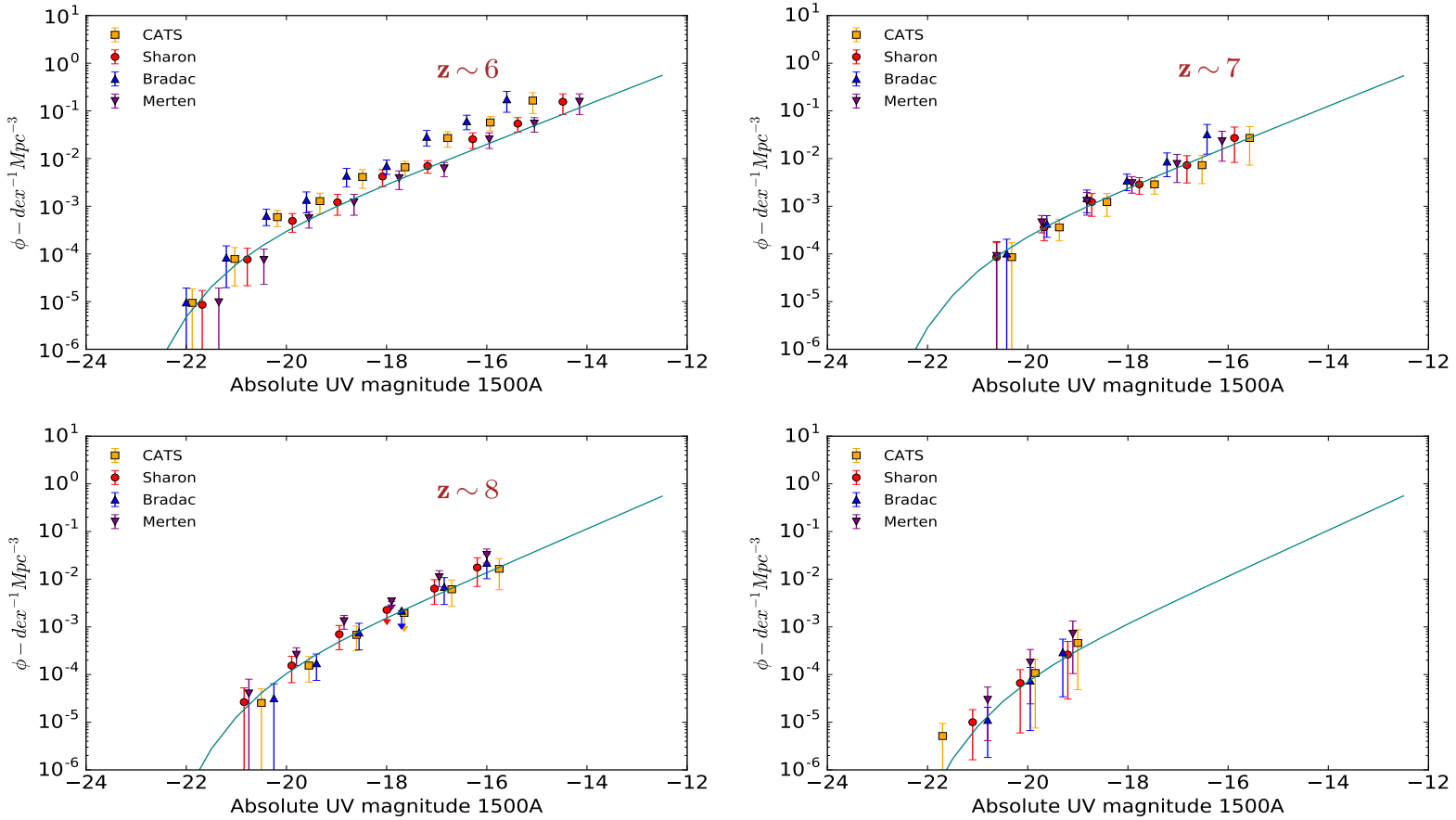


Figure 3.2: The UV LF at $z = 6 - 9$ in the MACSJ0416 cluster and its parallel field estimated using the lensing models of CATS, Sharon, Bradac and Merten using disc-like galaxies in completeness simulations. There is scatter between the different LFs, which is a result of different magnification factors estimated from the lensing models. But in all the cases a steeply increasing faint-end slope is observed without any evidence of a turn over. The solid green line is our best fit Schechter function to our fiducial luminosity function estimated from MCMC analysis using the median magnification factor, with disc-like galaxies in completeness simulations. The error bars on our data points take into account the errors on photometric redshifts, errors on magnitudes and Poisson errors.

3.2.2 Comparison with previous work

As can be seen from Fig. 3.1, there are some differences and similarities between our work and previous work[8]. First, at $z \sim 6$ we observe a disagreement in the binned luminosity function values at various luminosities for the number densities across the entire luminosity range. We, for example, do not see the upturn in the luminosity function near $M_{\rm UV} = -18$ as seen by Livermore, Finkelstein & Lotz (2017). We, however, also do not find the downturn that Atek *et al.* (2018) and Bouwens *et al.* (2017b) find in the UV luminosity function near $M_{\rm UV} = -15$. Instead, we find that at $z \sim 6$ the luminosity function is well fit by a Schechter function, as well as a single power-law, up to the faintest limits we go, $M_{\rm UV} = -13.5$. Similarly, looking at the faint-end of the LF, we find a difference in the estimated error bars between our work and Atek *et al.* (2018) and Bouwens *et al.* (2017b). Our errors bars are likely underestimated due to the fact that we have only used the median magnification factors to demagnify the magnitudes for individual sources and also have not included the errors due to cosmic variance in our analysis.

At this redshift, we generally find that our binned luminosity function values are lower than previous studies. This can be attributed to the significantly smaller volume that we are probing as compared to Finkelstein *et al.* (2015), Bouwens *et al.* (2015b), Bouwens *et al.* (2017b) and Atek *et al.* (2018) [Bouwens *et al.* (2015b) utilize data sets from CANDELS, HUDF09, HUDF12, ERS, and the BoRG/HIPPIES programs (Trenti *et al.*, 2011), Bouwens *et al.* (2017b) combine the data from the first four HFF clusters; Abell 2744, MACS 0416, MACS 0717, and MACS 1149, Finkelstein *et al.* (2015) use data sets from CANDELS/GOODS, HUDF, the parallel fields near MACSJ0416 and Abell2744 from the HFF program, whereas Atek *et al.* (2018) combine the data sets of all 6 clusters from the HFF program]. The difference in binned luminosity function values with Livermore, Finkelstein & Lotz (2017) is, however, unclear since they are probing a similar volume as our study (They combine data from the Abell2744 and the MACSJ0416 clusters). Further discrepancy is observed in the Schechter function parameters. Livermore, Finkelstein & Lotz (2017) are able to probe magnitudes as faint as $M_{\rm UV} = -12.5$, with higher number densities resulting in a steeper faint-end slope than ours. Comparing our detections with Livermore, Finkelstein & Lotz (2017), we find that their faintest source at $M_{\rm UV} = -12.5$ lie in the Abell2744 cluster, which we have not included in our analysis in this study, and the next faintest source at $M_{\rm UV} = -14$

[8]Note: We restrict the comparison of our results with previous work to the best-fit Schechter parameters derived using disc-galaxies in our completeness simulations, and do not compare our results derived using point sources.

is in the MACSJ0416 cluster, but is not recovered in our analysis (it appears to be a possible noisy detection). In the case of $M^*_{\rm UV}$ values, we are unable to put robust constraints on $M^*_{\rm UV}$ as there are very few galaxies in the brightest bins ($\sim 1-3$), given the smaller volume we are probing in this study.

At $z \sim 7$, our binned luminosity function values are in excellent agreement with Laporte *et al.* (2016) who combine data from the HFF MACSJ0717 cluster and its parallel field. However, our binned luminosity function values are lower as compared to other studies, once again possibly because of the smaller volume/area that we are probing. We also find that our faint-end slope is generally in agreement with previous studies, except Laporte *et al.* (2016) and Ishigaki *et al.* (2018) who are finding significantly shallower and steeper faint-end slopes respectively. This is because we are going fainter than Laporte *et al.* (2016) at this redshift, whereas Ishigaki *et al.* (2018) are probing ~ 2 magnitudes fainter than us and finding higher number densities with the complete HFF data, resulting in observed differences in the measured values of the faint-end slopes.

Comparing to previous studies at $z \sim 8$, we find large discrepancies due to smaller number statistics in all the studies. For example, there are inconsistencies in the binned luminosity function values at various luminosities. Our number densities are in agreement with Finkelstein *et al.* (2015) in brighter bins upto $M_{\rm UV} = -19$, after which they find higher number densities in their faintest bin at $M_{\rm UV} = -18.5$, possibly leading to a steeper faint-end slope than ours. Similarly, the number densities of Ishigaki *et al.* (2018) are higher than ours, except that they find a drastic drop in their number densities at $M_{\rm UV} = -18.25$. Similarly, there is disagreement in the measured values of faint-end slopes at this redshift, in that our faint-end slope is steeper, except Finkelstein *et al.* (2015).

Finally, at $z \sim 9$, we find that our faint-end slope is in agreement with Laporte *et al.* (2016). McLeod, McLure & Dunlop (2016) and Ishigaki *et al.* (2018) are finding shallower faint-end slopes than ours, however, we note that they held the value of faint-end slope α to be fixed while fitting their data points.

In general, at all redshifts, the difference in errors bars on the Schechter parameters between our work and previous work (e.g., Finkelstein *et al.* 2015; Bouwens *et al.* 2015b; Atek *et al.* 2018) can be attributed to the fact that we do not include the errors due to cosmic variance on our number densities.

3.2.3 Comparison with theoretical predictions

In Fig. 3.3, we compare our measurements of the UV LFs with the theoretical galaxy formation models from cosmological hydrodynamics simulations. The simu-

lations results are taken from the IllustrisTNG project that combines the three IllustrisTNG simulations; TNG50, TNG100 and TNG300 (Vogelsberger *et al.*, 2019), the FirstLight project (Ceverino, Glover & Klessen, 2017), the "Cosmic Reionization On Computers" (CROC) project (Gnedin, 2016) and the simulations results from Finlator, Oppenheimer & Davé (2011). We refer the reader to the relevant papers for the details of the respective simulations. For consistency, we renormalize their number densities to the comoving volume of the cosmology used in this thesis ($H_0 = 70$ km s^{-1} Mpc^{-1}, $\Omega_M = 0.3$, and $\Omega_\Lambda = 0.7$), wherever necessary.

Inspecting our measurements of the UV LF $z \sim 6$, we find an agreement between our results estimated with disc-like galaxies in completeness simulations with Vogelsberger *et al.* (2019), Ceverino, Glover & Klessen (2017) and Gnedin (2016) at $-16 < M_{\rm UV} < -14$, after which the models of Ceverino, Glover & Klessen (2017) and Gnedin (2016) predict a turn over at the lowest luminosities. This turn over is likely to be caused due to the suppression of star formation in low-mass galaxies by feedback from reionization as well as by inefficient cooling of gas at low metallicities (Finlator, Oppenheimer & Davé 2011; Jaacks *et al.* 2012; Gnedin 2016). Our results are in disagreement with the models at bright luminosities ($-22 < M_{\rm UV} < -17$).

At $z \sim 7$, our results with disc-like galaxies are in excellent agreement with Vogelsberger *et al.* (2019) at $-21 < M_{\rm UV} < -17$, after which it appears that the model predicts a turn over at low luminosities. However, our results are in disagreement with the results of Finlator, Oppenheimer & Davé (2011) and Gnedin (2016) who predict an overabundance of galaxies and fewer number densities of galaxies, respectively, at all the luminosities probed in this study.

Inspecting the results at $z \sim 8$, once again the observed UV LF with disc-like galaxies are in excellent agreement with Ceverino, Glover & Klessen (2017) for the luminosity range probed in this work. The results are also in excellent agreement with Vogelsberger *et al.* (2019) at $-21 < M_{\rm UV} < -17$, beyond which the model predicts a turn over. The measured UV LFs, however, are in disagreement with Finlator, Oppenheimer & Davé (2011) and Gnedin (2016) who once again predict an overabundance of galaxies and fewer number densities of galaxies, respectively, at all the luminosities probed in this work. Finally, at $z \sim 9$, our results with point sources are in somewhat agreement with the model predictions of Vogelsberger *et al.* (2019).

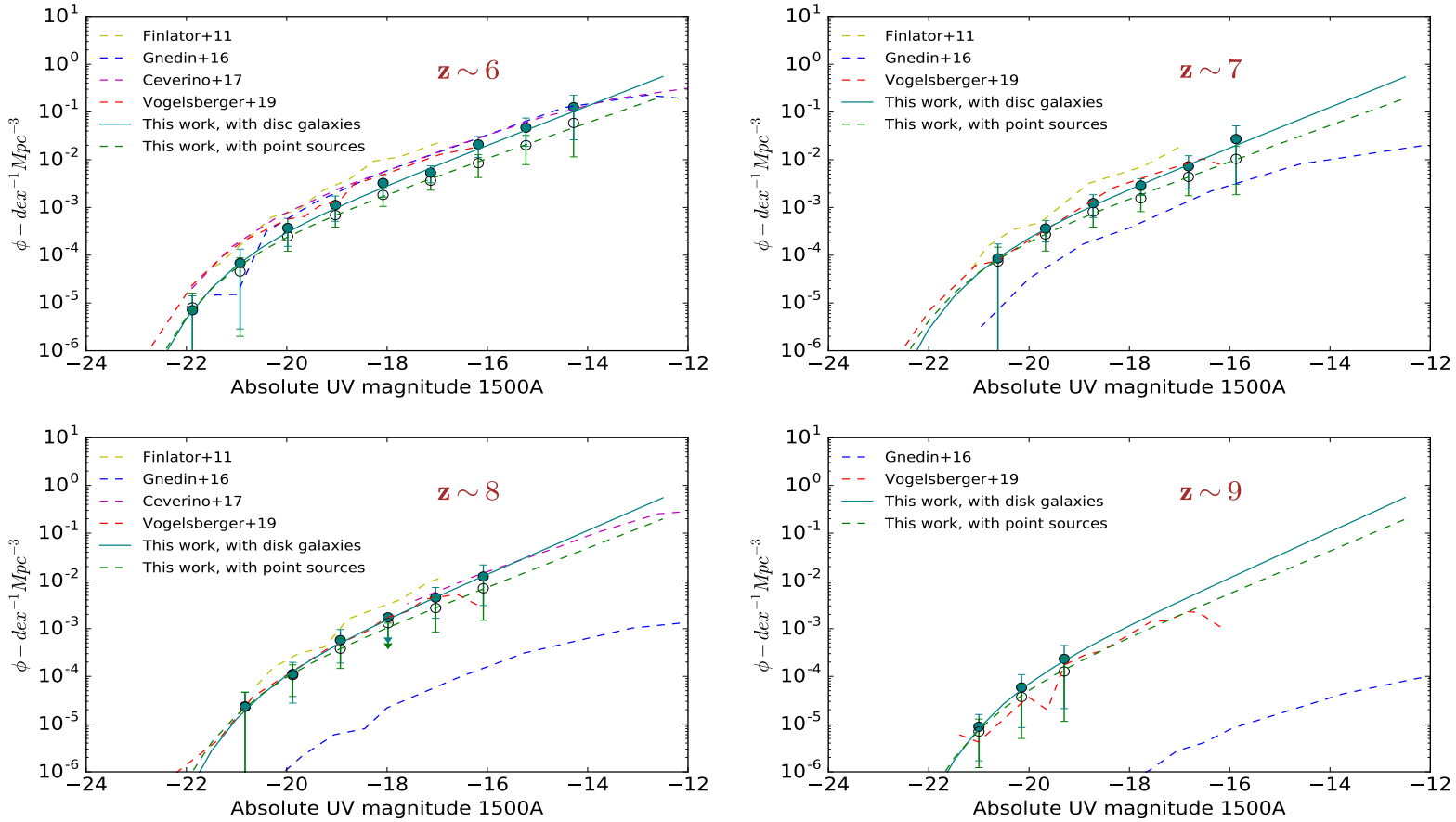


Figure 3.3: Comparison of the observed UV LF at $z = 6 - 9$ in the MACSJ0416 cluster and its parallel field estimated using disc-like galaxies and point sources in completeness simulations with theoretical predictions. We show the results from the cosmological hydrodyamics simulations of the IllustrisTNG project (Vogelsberger *et al.*, 2019), FirstLight project (Ceverino, Glover & Klessen, 2017), CROC project (Gnedin, 2016) and the simulations results from Finlator, Oppenheimer & Davé (2011).

3.3 Galaxy stellar mass function

The galaxy stellar mass function is a valuable mechanism to probe the growth of stellar mass, as it includes all processes such as star formation and mergers, which contribute to building up the mass of a galaxy. Cosmological simulations produce a distribution of dark matter halos by hierarchical assembly following the initial tiny perturbations in the early young Universe. The mass distribution of these halos follows the Schechter form and for this reason a Schechter function for the galaxy mass distribution is also expected. We therefore fit our number densities in each redshift bin derived in Section 2.3.8 with a Schechter function of the form:

$$\Phi(M) = ln(10)\Phi^* 10^{(M-M^*)(\alpha+1)} e^{-10^{(M-M^*)}}, \tag{3.3}$$

where ϕ^* provides the normalization, M^* corresponds to the characteristic stellar mass at which the function turns over from a power law into an exponential form, and α is the slope of the low-mass end. α is usually negative, implying large numbers of galaxies with low masses.

3.3.1 Best fit Schechter parameters and their uncertainties for the GSMF

To determine the best fit Schechter parameters and their uncertainties for GSMF, we perform a MCMC analysis described in 3.2.1 that examines the three-dimensional parameter space of Schechter parameters. Just as for the UV LF, for each redshift, we use 10^2 MCMC chains of 10^4 steps each to explore fully the parameter space, building a distribution of M^*, Φ^* and α. For the priors, we limit the parameter space to $8 < \log(M^*/M_\odot) < 13$, $\log(\phi^*/\mathrm{Mpc}^{-3}) > -8$ and $\alpha > -4$. However, at $z = 9$, where the sample size is small, we fix M^* to the value estimated at $z = 8$. Fig. 3.4 shows 100 random samples from the chain plotted on the top of our data points for our GSMF at $z \sim 6$.

For our final result, just as for the UV LF, we join the chains together giving a distribution of 10^6 values of Schechter function parameters at each redshift. The best-fit values for each Schechter function parameter are the median of this distribution, with the uncertainties covering the central 68 per cent of the distribution. Fig. 3.5 shows the two dimensional posterior probability distributions of characteristic stellar mass M^* and faint end slope α at $z = 6 - 8$.

Similar to the UV LF, we derive the best-fit Schechter parameters and their

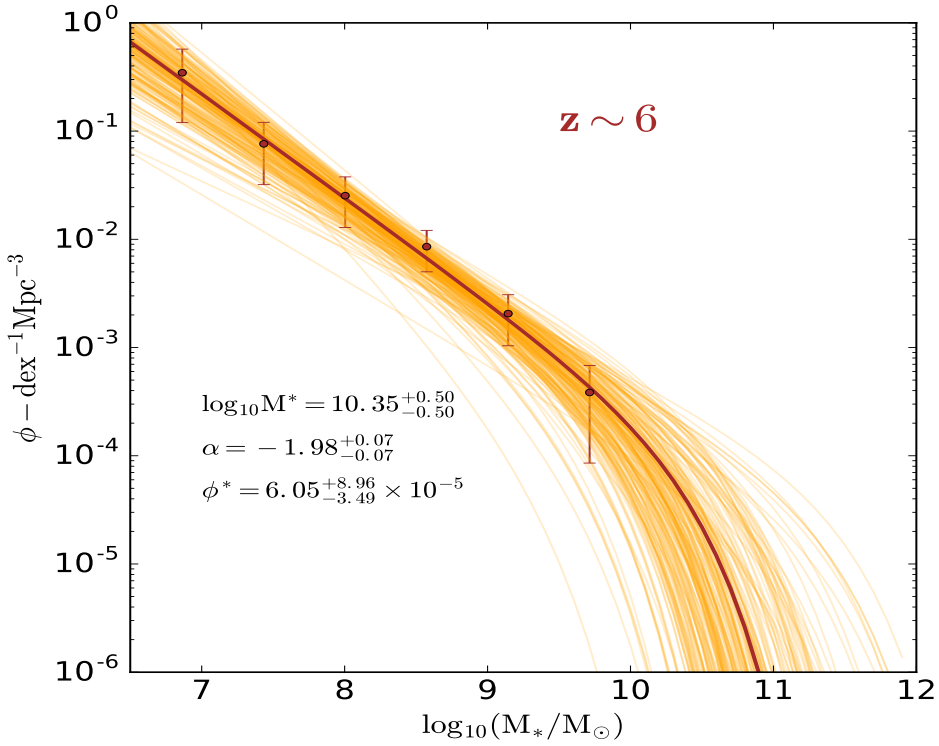


Figure 3.4: Distribution of 100 random samples drawn from the chain at $z \sim 6$ from our MCMC analysis and projected into the space of the observed data.

uncertainties for our GSMF using the completeness curves described in 2.3.5, with both disc-like galaxies and point sources, in order to investigate the effect of galaxy sizes on completeness corrections, and hence on the faint-end slopes. Our results, along with the values from the literature, are listed in Table 3.2 and the resulting GSMFs plotted alongside previous work are shown in Fig. 3.6. The error bars on our data points in Fig. 3.6 take into account the errors on photometric redshifts, errors on magnitudes, Poisson errors and uncertainties due to lensing maps, but does not include the errors due to cosmic variance.

We estimate the fractional uncertainty in number densities due to cosmic variance using the method described in Section 3.2.1 and in Fig. 3.6 we show the measured error on number densities for galaxies of $10^{8.5}\mathrm{M}_{\odot}$.

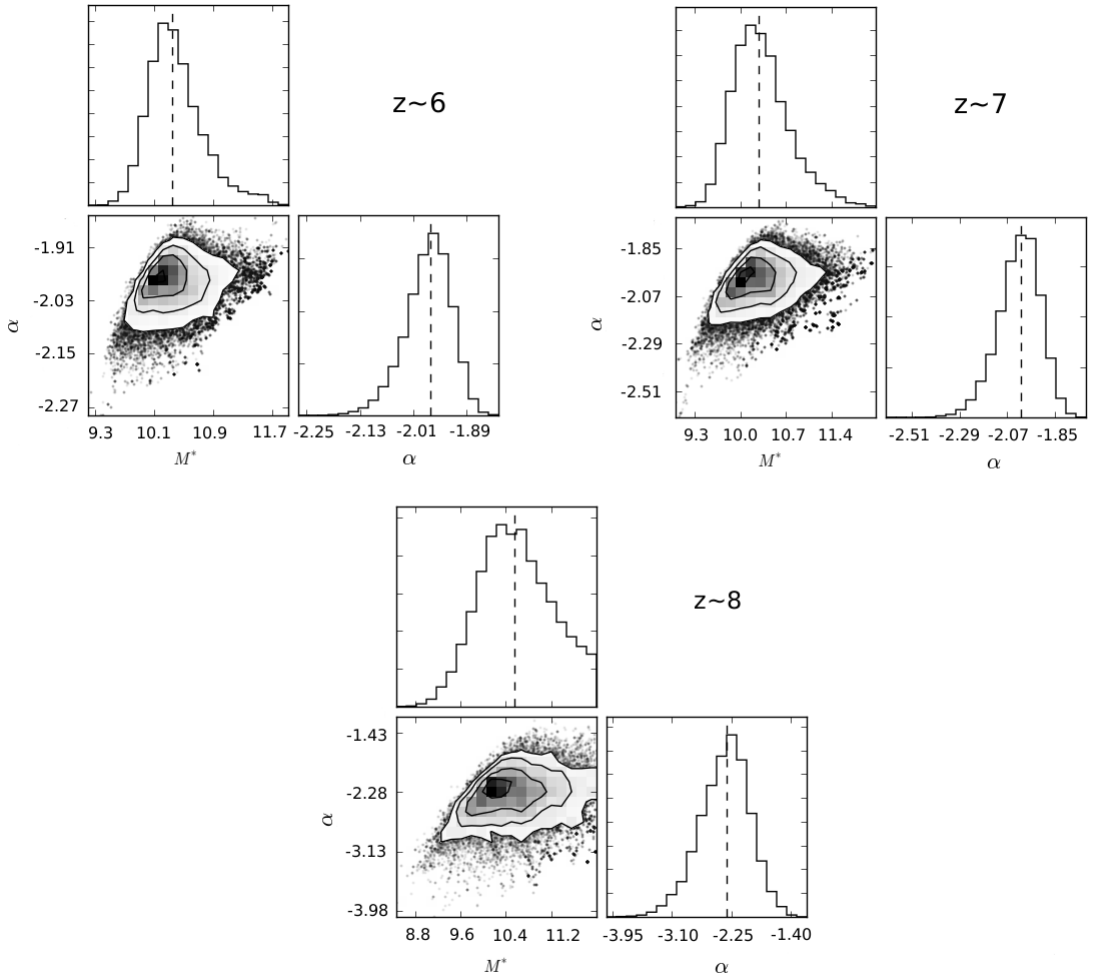


Figure 3.5: Corner plots showing the two dimensional posterior probability distributions of characteristic stellar mass M^* and faint end slope α at $z = 6, 7$ and 8 with contours shown at 0.5, 1, 1.5, and 2 sigma. Top left: Posterior probability distribution at $z \sim 6$. Top right: Posterior probability distribution at $z \sim 7$. Bottom: Posterior probability distribution at $z \sim 8$. The marginalized distribution for each parameter is shown independently in the histograms, with the dashed line being the median value of the distribution.

Table 3.2: Best fit Schechter function parameters and their uncertainties for our GSMFs. The quoted best fit values and 1σ errors of the Schechter parameters constitute the median and the central 68 per cent of posterior distribution of each parameter from our MCMC analysis.

Redshift	$\log_{10}M^*$	α	$\phi^*(10^{-5}\mathrm{Mpc}^{-3})$
$z\sim 6$			
This work (disc galaxies)	$10.35^{+0.50}_{-0.50}$	$-1.98^{+0.07}_{-0.07}$	$6.05^{+8.96}_{-3.49}$
This work (point sources)	$10.29^{+0.65}_{-0.67}$	$-1.89^{+0.09}_{-0.10}$	$5.43^{+8.16}_{-3.29}$
Song et al. (2016)	$10.72^{+0.29}_{-0.30}$	$-1.91^{+0.09}_{-0.09}$	$1.35^{+1.66}_{-0.75}$
Duncan et al. (2014)	$10.87^{+1.13}_{-0.54}$	$-2.00^{+0.57}_{-0.40}$	$1.40^{+41.1}_{-1.4}$
Grazian et al. (2015)	$10.49^{+0.32}_{-0.32}$	$-1.55^{+0.19}_{-0.19}$	$6.91^{+13.5}_{-4.57}$
$z\sim 7$			
This work (disc galaxies)	$10.27^{+0.60}_{-0.67}$	$-2.01^{+0.17}_{-0.13}$	$3.90^{+9.20}_{-2.85}$
This work (point sources)	$10.25^{+0.67}_{-0.71}$	$-1.91^{+0.18}_{-0.14}$	$2.93^{+6.29}_{-1.99}$
Song et al. (2016)	$10.78^{+0.29}_{-0.28}$	$-1.95^{+0.18}_{-0.18}$	$0.53^{+1.10}_{-0.38}$
Duncan et al. (2014)	$10.51^{+0.36}_{-0.32}$	$-1.89^{+1.39}_{-0.61}$	$3.6^{+3.01}_{-0.35}$
Grazian et al. (2015)	$10.69^{+1.58}_{-1.58}$	$-1.88^{+0.36}_{-0.36}$	$0.57^{+59.68}_{-0.56}$
$z\sim 8$			
This work (disc galaxies)	$10.54^{+1.00}_{-0.94}$	$-2.30^{+0.51}_{-0.46}$	$0.095^{+0.56}_{-0.080}$
This work (point sources)	$10.48^{+1.19}_{-0.92}$	$-2.17^{+0.55}_{-0.53}$	$0.090^{+0.51}_{-0.078}$
Song et al. (2016)	$10.72^{+0.29}_{-0.29}$	$-2.25^{+0.72}_{-0.35}$	$0.035^{+0.246}_{-0.030}$
$z\sim 9$			
This work (disc galaxies)	10.54 (fixed)	$-2.38^{+0.72}_{-0.88}$	$0.057^{+0.65}_{-0.050}$
This work (point sources)	10.48 (fixed)	$-2.28^{+0.83}_{-0.98}$	$0.045^{+0.63}_{-0.040}$

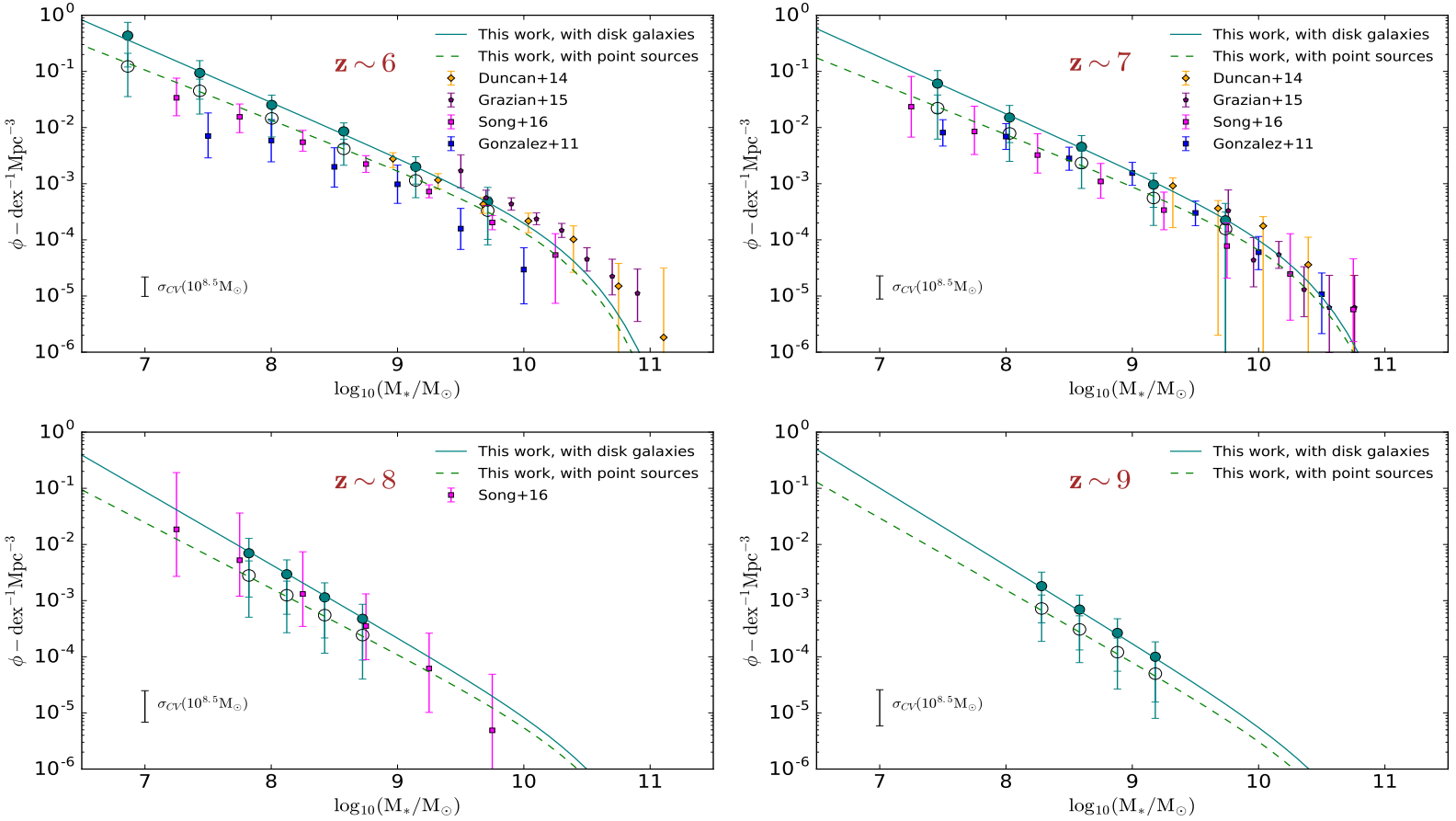


Figure 3.6: The GSMF at $z = 6 - 9$ in the MACSJ0416 cluster and its parallel field. The solid green line is our best fit Schechter function from our MCMC analysis to the green circles, considering disc-like galaxies in completeness simulations. The dashed green line is our best fit Schechter function from MCMC analysis to the open green circles, using point sources. The error bars on our data points take into account errors on photometric redshifts, errors on stellar mass, Poisson errors and uncertainties due to lensing maps, but does not include errors due to cosmic variance. The representative error bar in the bottom left corner of each plot shows the measured error on number densities for galaxies of $10^{8.5}M_\odot$ due to cosmic variance.

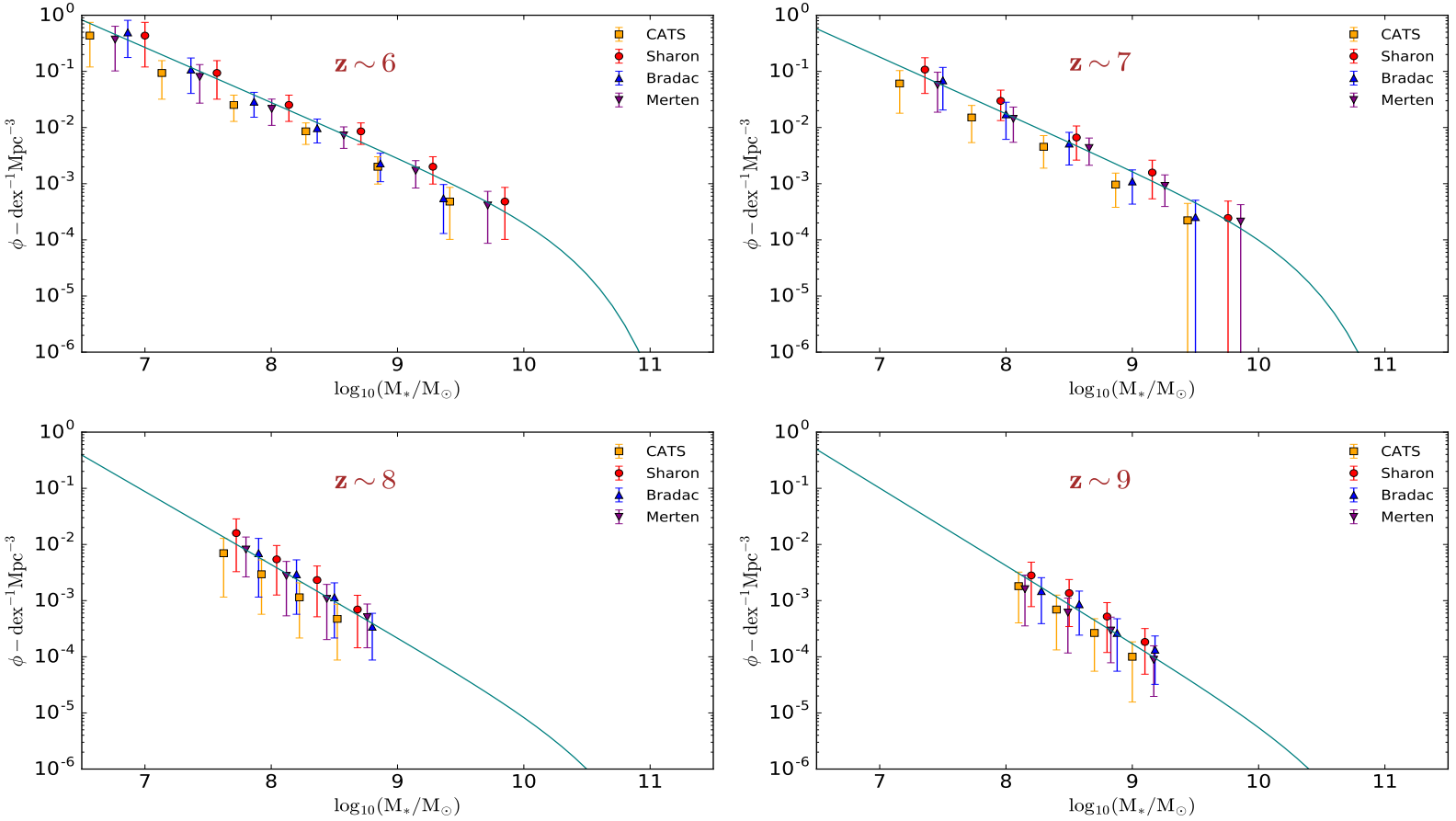


Figure 3.7: The GSMF at $z = 6-9$ in the MACSJ0416 cluster and its parallel field estimated using the lensing models of CATS, Sharon, Bradac and Merten using disc-like galaxies in completeness simulations. There is scatter between the different MFs, which is a result of different magnification factors estimated from the lensing models. But in all the cases a steeply increasing low-mass end slope is observed without any evidence of a turn over. The solid green line is our best fit Schechter function to our fiducial mass function estimated from MCMC analysis using the median magnification factor, with disc-like galaxies in completeness simulations. The error bars on our data points take into account the errors on photometric redshifts, errors on magnitudes and Poisson errors.

Examining our best fit Schechter parameters, our results show an apparent steepening ($\sim 0.5\sigma$ significant) of the low mass end slope α with increasing redshift ($-1.98^{+0.07}_{-0.07}$, $-2.01^{+0.17}_{-0.13}$, $-2.30^{+0.51}_{-0.46}$ and $-2.38^{+0.72}_{-0.88}$ at $z = 6, 7, 8$ and 9 respectively). However, similar to the UV LF, we cannot rule out a constant α between $z = 6 - 9$ and more data is needed to confirm the trend at these redshifts.. There is also a decrease in Φ^* with increasing redshift, but no evolution in M^* is observed. We notice a similar trend for the low mass end slope α (steepening with increasing redshift) when point sources are considered in our completeness simulations, albeit with a shallower slope as compared to disc galaxies ($\Delta\alpha \sim 0.09 - 0.13$). A decrease in Φ^* with increasing redshift is also observed in the case of point sources, but once again no evolution in M^* is observed. Fig. 3.8 shows the redshift evolution of the Schechter parameters for the stellar mass functions along with the values from the literature.

Similar to the UV LFs, in order to show the variation due to individual lensing model, we also estimate the number densities with four lensing models of CATS (Jauzac *et al.*, 2014), Sharon (Johnson *et al.*, 2014), Bradac (Bradač *et al.*, 2009) and Merten (Merten *et al.*, 2011). The resulting MFs for each redshift bin are shown in Fig. 3.7. It is seen that there is scatter between the different MFs, which is a result of different magnification factors estimated from the lensing models. However, in all the cases we observe a steeply increasing low-mass end slope without any evidence of a turn over.

Finally, since the faintest objects have their flux underestimated due to the use of MAG_AUTO (as shown in Fig. 2.7), similar to the UV LFs, we also investigate the implications of this on the slope of the derived mass functions at all redshifts. For this, we use the offset between measured magnitude with MAG_AUTO and the input magnitude in our observed distribution, consider how a magnitude change correlates with a mass change assuming the same mass-to-light ratio, and refit the mass functions. With this we find that the low mass end slopes are shallower by $\Delta\alpha \sim 0.05 - 0.06$ than reported in this work.

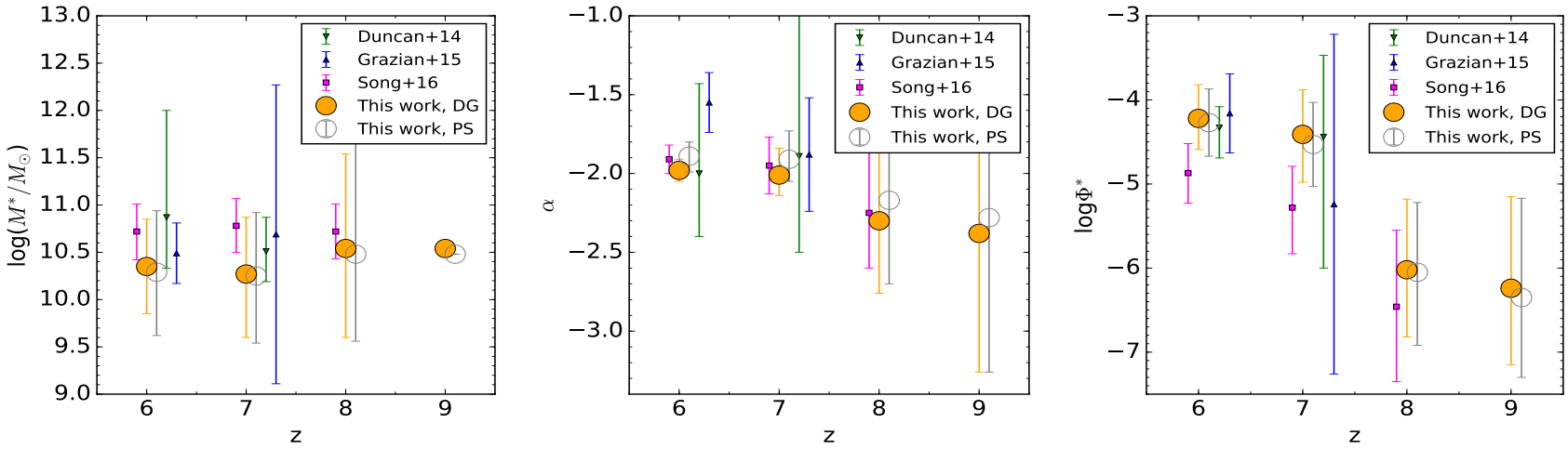


Figure 3.8: Redshift evolution of best fit Schechter function parameters for our stellar mass functions. The solid orange circles represent the best fit Schechter parameters considering disc-like galaxies in our completeness simulations, whereas the open circles are our results considering point sources. The low mass end slope α steepens with increasing redshift, number density Φ^* decreases with increasing redshift, whereas no evolution in the characteristic mass M^* is observed. **Note:** The error bars on characteristic mass M^* at $z \sim 9$ are not shown since we keep the value of M^* fix to the value estimated at $z \sim 8$.

3.3.2 Comparison with previous work

Fig. 3.6 shows the comparison of our GSMF results at $z = 6 - 9$ with previous literature work [9]. The first thing that we notice here is the dissimilarity of normalization values between our work and the literature values at all redshifts. We are finding higher normalization values than González *et al.* (2011), Duncan *et al.* (2014), Grazian *et al.* (2015) and Song *et al.* (2016) at all redshifts, except at $z \sim 6$ where the normalization values of Grazian *et al.* (2015) are higher than ours. The reason for this discrepancy is unclear, however, it could be attributed to the shallower slopes of our best fitted $\log_{10}(\mathrm{M_*/M_\odot}) - \mathrm{M_{UV}}$ relation that we are finding (See Section 3.4) as compared to previous studies (See Table 3.3). A shallower slope of $\mathrm{M_*} - \mathrm{M_{UV}}$ results into higher normalization values and steeper low mass end slope (Song *et al.*, 2016). Although, we do not use our $\mathrm{M_*} - \mathrm{M_{UV}}$ relation to calculate our GSMF, we point out that our results of higher normalization values and steep low mass end slope do strengthen the argument.

Inspecting the high mass end of our GSMFs, we find a deficit of bright/massive galaxies in comparison to the literature, making it difficult for us to put any robust constraints on the high mass end of the GSMF. The lack of brighter galaxies can be attributed to the smaller survey area that we are probing in our work. Interestingly, we notice that the massive galaxies that we find in our study all come from the parallel field alone (considering the relatively larger volume that it allows us to probe as compared to the cluster) i.e., the cluster area is devoid of massive galaxies. At $z \sim 6$, the number densities of our highest mass bin ($\log(M_*/M_\odot) = 9.7 - 10.3$) are in agreement with Duncan *et al.* (2014) and Grazian *et al.* (2015), but higher than Song *et al.* (2016) and González *et al.* (2011). At $z \sim 7$, the number densities in our highest mass bin are in agreement with González *et al.* (2011), are lower than Duncan *et al.* (2014), but once again higher than Song *et al.* (2016).

At the low mass end, even though our survey volume is significantly smaller than those of other studies, the strong gravitational lensing effect allows us to probe masses as low as $10^{6.8} M_\odot$, enabling us to put robust constraints on the low mass end slope α. Since the lowest mass bin of Grazian *et al.* (2015) is $\log(M_*/M_\odot) \sim 9$, we compare our low mass end of the GSMF with González *et al.* (2011), Duncan *et al.* (2014) and Song *et al.* (2016) who are able to reach lower in masses. At $z \sim 6$, our number densities are higher than these studies. We also find a steep faint end slope α of $-1.98^{+0.07}_{-0.07}$, which is steeper than all the literature values except

[9]Note: We restrict the comparison of our results with previous work to the best-fit Schechter parameters derived using disc-galaxies in our completeness simulations, and do not compare our results derived using point sources.

Duncan *et al.* (2014), who are finding a slope of $-2.00^{+0.57}_{-0.40}$, albeit with large error bars. At $z \sim 7$, we are again finding higher number densities and a steeper slope than previous studies. This could be attributed to the shallower slopes of our best fitted $\log_{10}(\mathrm{M_*/M_\odot}) - \mathrm{M_{UV}}$ relation that we are finding as mentioned earlier in this section. Finally, at $z \sim 8$, we are finding higher number densities and steeper slope than Song *et al.* (2016).

3.3.3 Comparison with theoretical predictions

In Fig. 3.9, we compare our measurements of the GSMFs with the theoretical galaxy formation models of semi-analytic models (SAMs) as well as cosmological hydrodynamics simulations. The three SAMS (Croton *et al.* 2006; Lu *et al.* 2011; Somerville *et al.* 2008) are taken from Lu *et al.* (2014), whereas the cosmological hydrodynamics simulations are from the Illustris project (Genel *et al.*, 2014), Choi & Nagamine (2012), Dayal *et al.* (2014) and the FirstLight project (Ceverino, Glover & Klessen, 2017). We refer the reader to the relevant papers for the details of the instructions for the baryonic processes implemented in the SAMs and the hydrodynamics simulations. For consistency, we renormalize their number densities to the comoving volume of the cosmology used in this thesis ($H_0 = 70$ km s^{-1} Mpc^{-1}, $\Omega_M = 0.3$, and $\Omega_\Lambda = 0.7$).

Examining our stellar mass functions at $z \sim 6$, there is an agreement between the measurements of mass functions estimated with point sources in our completeness simulations and the SAMs of Somverville and Lu (which assumes the strongest outflows in low-mass galaxies) at the high-mass end ($8 < \log(M_*/M_\odot) < 10$). However, these models underestimate the abundance of low mass galaxies at stellar mass less than $\log(M_*/M_\odot) < 8$. Of the three SAMs, Croton model (that implements the weakest outflows in low-mass galaxies) exhibits the least agreement with our results. Comparing with the FirstLight simulations of Ceverino, Glover & Klessen (2017), although they exhibit the steepest low-mass end slopes, our observations do not match with their predictions.

At $z \sim 7$, first inspecting the low-mass end, there is an excellent agreement between our results with point sources and the cosmological hydrodynamics simulations of Illustris (Genel *et al.*, 2014). An excellent agreement is also observed between our measurements of GSMFs with disc-like galaxies and the predictions of Dayal *et al.* (2014) along with a lesser agreement to Choi & Nagamine (2012) at this redshift. However, all these models underestimate the abundance of high mass galaxies ($\log(M_*/M_\odot) > 9$) .

Finally, comparing our results at $z \sim 8$, our results estimated with disc-like

galaxies are in general agreement with Choi & Nagamine (2012), except at $\log(M_*/M_\odot) < 9$ where the model exhibits a steeper low-mass end slope. The results also show some agreement with Ceverino, Glover & Klessen (2017) model at masses $\log(M_*/M_\odot) \sim 8$, but the model exhibits a shallower low-mass end slope at $\log(M_*/M_\odot) < 8$. Comparing with Dayal *et al.* (2014), our results do not match due to the overabundance of galaxies predicted by this model across the entire mass range probed. In general, we observe that none of the models match our new measurements of the GSMFs over the entire redshift range.

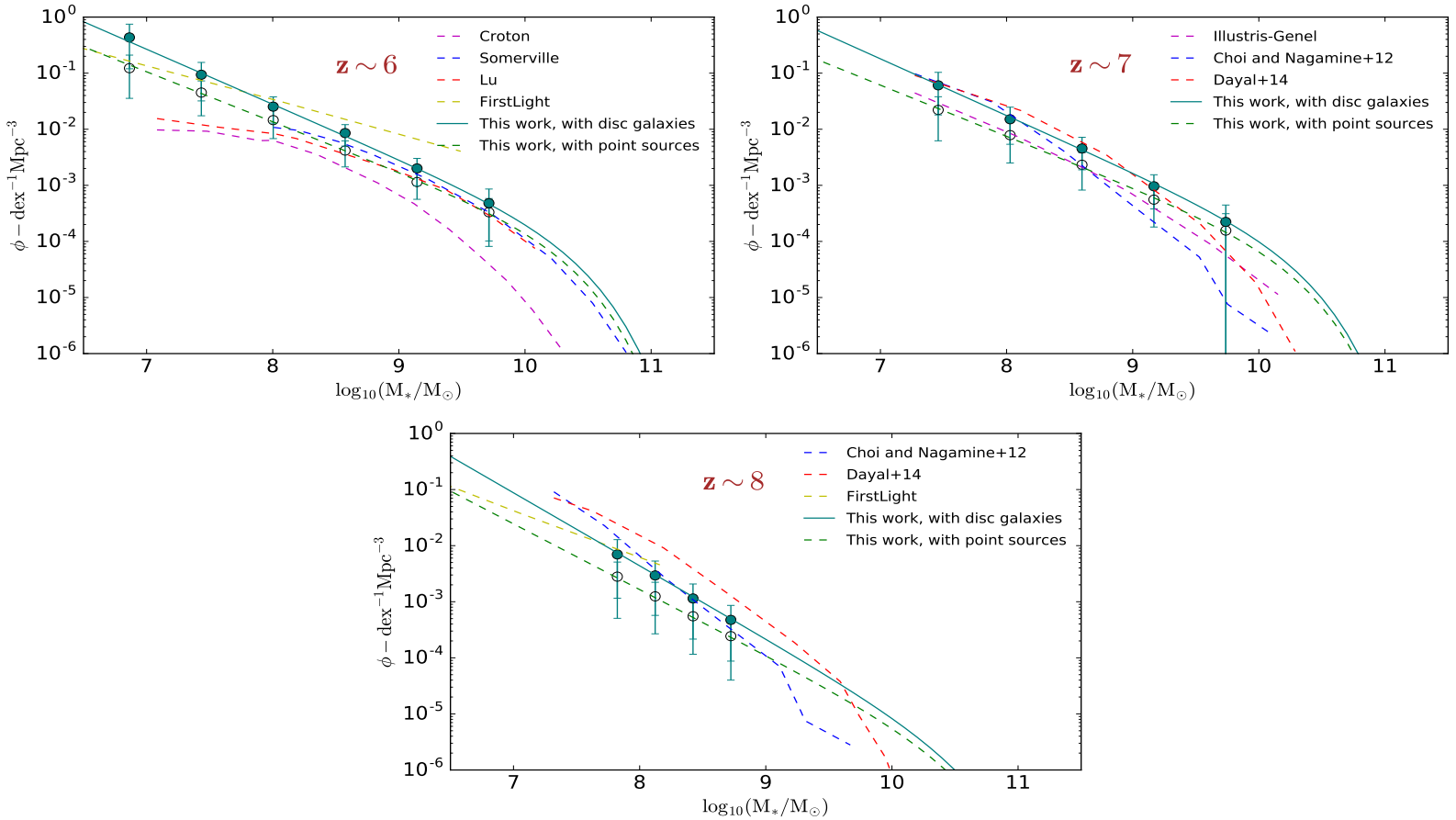


Figure 3.9: Comparison of the observed GSMF at $z = 6 - 8$ in the MACSJ0416 cluster and its parallel field estimated using disc-like galaxies and point sources in completeness simulations with theoretical predictions. We show the results from the SAMs of Croton, Somerville and Lu with stellar mass uncertainties convolved as described in Lu *et al.* (2014), along with the results from cosmological hydrodyamics simulations of Illustris project, FirstLight project, Choi & Nagamine (2012) and Dayal *et al.* (2014).

3.4 $M_* - M_{UV}$ relation

Scaling relations that describe the connection between the physical properties of galaxies such as metallicity, star formation rate, stellar mass, luminosity, etc. provide meaningful insights on galaxy formation and evolution. Using the stellar mass and the rest-frame absolute UV magnitudes estimated in Section 2.3.6.1, we now examine the mass-to-light ratios of our sample for each of our redshift bins to determine the scaling relation between these properties and how it extends to the lowest masses.

For this, we derive the best-fit $\log_{10}(M_*/M_\odot) - M_{UV}$ relation by fitting a linear function to the median masses of the sample in each rest-frame absolute UV magnitude bin of 0.5 mag. Fig. 3.10 shows the best-fit relation and Table 3.3 lists the best fitting values for our sample in each redshift bin. Whilst we notice a few high mass galaxies with faint UV magnitudes, there is a clear positive linear trend of increasing stellar mass with increasing rest-frame absolute magnitude (with a large scatter in all the redshift bins).

At $z \sim 6$, our results are in agreement with Duncan *et al.* (2014) at the bright end ($M_{UV} \leq -20$) when they include nebular emission lines while estimating their masses, but their stellar masses at the faint-end ($M_{UV} \geq -19$) are lower than ours, resulting in a steeper slope. Comparing with Song *et al.* (2016), their estimated masses with the inclusion of nebular emission lines at the bright end ($M_{UV} \leq -20$) are higher than ours, but they are finding lower measurements of stellar masses at the faint-end (($M_{UV} \geq 19$), resulting in a steeper slope than ours. González *et al.* (2011) estimate their masses without the inclusion of nebular emission lines and find higher estimates of stellar masses at $M_{UV} \leq -20$, but obtain lower masses at $M_{UV} \geq -19$, once again resulting in a steeper slope than we find in this study. We discover a similar trend when comparing our results to previous studies at $z \sim 7$ and $z \sim 8$, in that previous studies (e.g., Duncan *et al.* 2014; Song *et al.* 2016) are finding lower masses in faint UV bins at $M_{UV} \geq -19$, resulting in steeper slopes than ours.

In general, we find that at fainter magnitudes, our estimated masses are ~ 0.2 dex higher than previous studies. It is not clear why this is the case but this could be due to a couple of reasons: The discrepancy is likely a result of different fitting methods for stellar masses giving results which can differ by ~ 0.2 dex between otherwise similar methods (e.g., Mobasher *et al.* 2015). The inconsistency could also be a result of IRAC deblending. Although we rule out the possibility of IRAC deblending by carefully inspecting our sample, we do notice that in spite of our deep

IRAC data, the S/N of galaxies in faint UV bins is usually low ($\leq 3\sigma$). A detailed stacking analysis by Song *et al.* (2016) reveals that at faint UV luminosities, the stacked points are usually lower than the median values, reflecting that the stellar masses of low S/N galaxies in the faint UV bins are on average biased towards higher masses. However, see also Behroozi *et al.* (2018) for a further discussion on systematic differences in the UV mass-to-light ratios, where they recalculate the median UV-stellar mass relations from the Song *et al.* (2016) SED stacks for $z = 4 - 8$ galaxies, and argue that the masses found by them are too low, possibly a result of implausibly young ages being fit while estimating the stellar masses.

In order to see the effect of $\leq 3\sigma$ sources in faint UV bins on the best-fit $\log_{10}(\mathrm{M}_*/\mathrm{M}\odot) - \mathrm{M_{UV}}$ relation, we implement two fits to our data. By performing a linear fit to the full luminosity range probed in our study, we find that we are observing shallower slopes in all the redshift bins than previous studies of González *et al.* (2011), Duncan *et al.* (2014) and Song *et al.* (2016). This could be the reason for the higher observed normalization values in our derived GSMFs at all redshifts as mentioned previously in Section 3.3.2. However, by restricting our analysis to brighter magnitudes ($\mathrm{M_{UV}} \leq -16$) at $z \sim 6$, $z \sim 7$ and $z \sim 8$ and excluding the $\leq 3\sigma$ points from our sample, we observe a steepening of slopes in comparison (See Table 3.3), but these are still shallower than previous studies. This furthermore highlights the importance of deeper imaging with JWST to obtain accurate photometry of galaxies at $> 2\mu m$. Nevertheless, in both the cases, we find that the slopes of our best fitted $\log_{10}(\mathrm{M}_*/\mathrm{M}_\odot) - \mathrm{M_{UV}}$ relation are close to a constant mass-to-light ratio of -0.40, suggesting no strong evolution of mass-to-light ratio with luminosity. We notice that normalization, on the other hand, evolves very weakly from $z \sim 6$ to $z \sim 9$, with a decrease in normalization with increasing redshift.

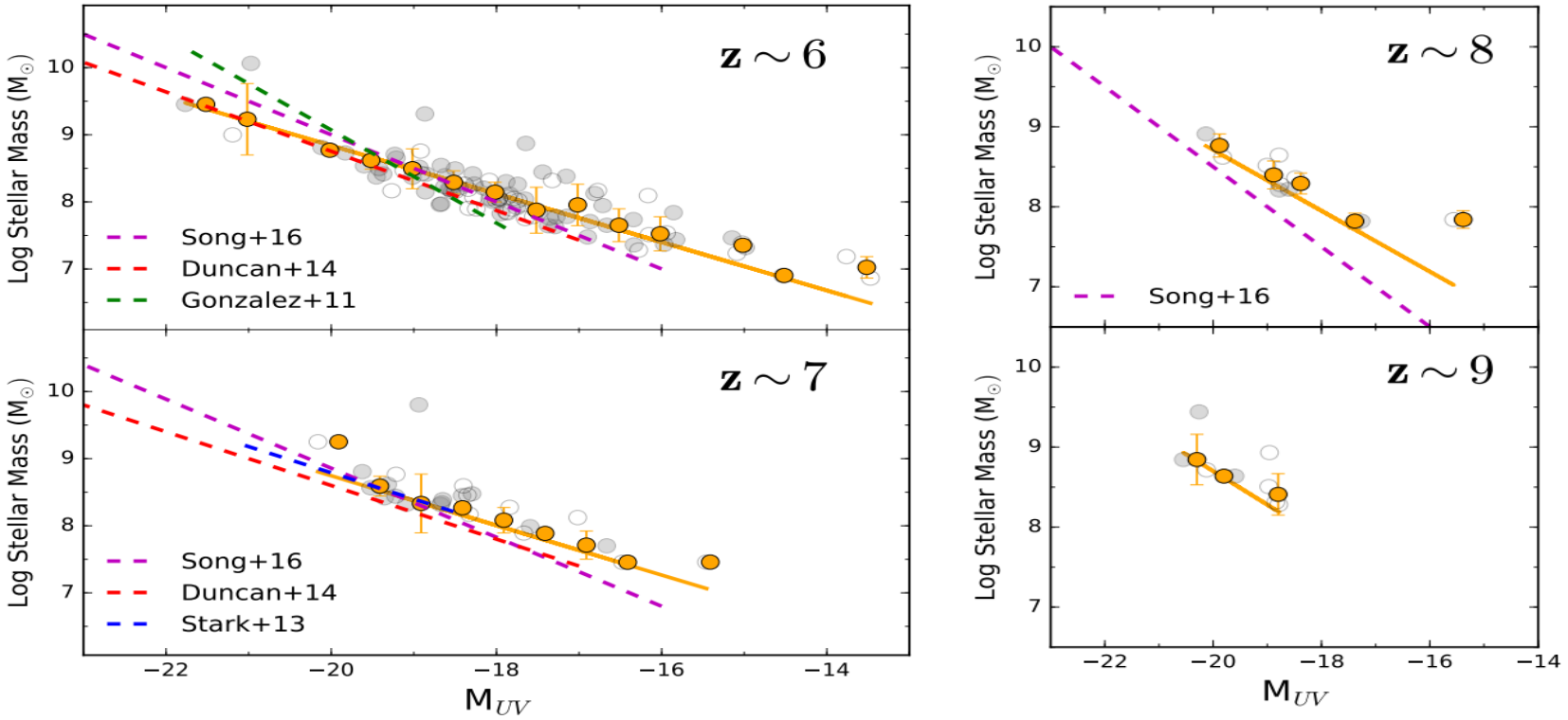


Figure 3.10: Stellar mass as a function of rest-frame absolute UV magnitude at 1500 Angstrom at $z = 6-9$. Grey filled circles represent sources with a S/N ratio $> 3\sigma$ at $3.6\mu m$ in IRAC, whereas grey open circles are those with a S/N ratio $\leq 3\sigma$. Filled yellow circles represent the median stellar masses in each rest-frame absolute UV magnitude bin of 0.5 mag, and the yellow error bars represent the standard deviation in stellar mass in each UV magnitude bin. The best-fit $\log_{10}(M_*/M\odot) - M_{UV}$ relation is shown by solid yellow line in each redshift bin. The best-fit $\log_{10}(M_*/M\odot) - M_{UV}$ lines of González *et al.* (2011), Stark *et al.* (2013), Duncan *et al.* (2014) and Song *et al.* (2016) are also shown by green, blue, red and magenta dashed lines, respectively, for comparison.

Table 3.3: Best-fit $\log_{10}(M_*/M\odot) - M_{UV}$ relation. The values in parentheses are the best-fit values when we restrict our analysis to brighter magnitudes ($M_{UV} \leq -16$). The quoted errors represent the 1σ uncertainties.

z	log $M_{*(M_{UV}=-19.5)}$	slope
6	8.66 ± 0.05	-0.38 ± 0.07
	(8.66 ± 0.07)	(-0.41 ± 0.06)
7	8.56 ± 0.08	-0.37 ± 0.09
	(8.58 ± 0.08)	(-0.40 ± 0.05)
8	8.52 ± 0.18	-0.38 ± 0.14
	(8.50 ± 0.16)	(-0.40 ± 0.15)
9	8.49 ± 0.28	-0.42 ± 0.21

3.5 Stellar mass density

To estimate the total stellar mass density (SMD) at $z = 6-9$, we integrate the best-fit Schechter function in each redshift bin from $M_* = 10^8$ to $10^{13} M_\odot$. These limits were chosen so as to allow us to compare with the SMD values in the literature. We estimate the 1σ uncertainties as the minimum and maximum range of stellar mass densities within the 1σ contours of Schechter parameters obtained from our MCMC analysis in Section 3.3.1. Table 3.4 lists our estimates of SMD along with their 1σ uncertainties and Fig. 3.11 shows the evolution of the SMD. Our results are shown as solid orange points when disc-like galaxies are considered in our completeness simulations, and as open grey circles considering point sources. In Fig. 3.11, we also show the results from the literature for comparison, converted to Chabrier IMF where required.

We find that at $z \sim 6$ and $z \sim 7$, our results are in agreement with González *et al.* (2011) and Duncan *et al.* (2014), but higher than Stark *et al.* (2013), Grazian *et al.* (2015) and Song *et al.* (2016). Similarly, at $z \sim 8$, our SMD estimates are higher than the only estimates of Song *et al.* (2016) at this redshift within error bars.

Our measurements reveal that the integrated stellar mass density has increased from $\log_{10}\rho_* = 5.61^{+0.92}_{-0.90}$ $M_\odot Mpc^{-3}$ at $z = 9$ to $\log_{10}\rho_* = 6.79^{+0.13}_{-0.12}$ $M_\odot Mpc^{-3}$ at $z = 6$, confirming that the process of ongoing star formation and merging increases the total stellar mass in the Universe with time. We also find that there is a surprisingly high amount of stellar mass density for galaxies in the early universe up to $z \sim 9$. This is an indication that galaxies of masses around 10^8 $M_\odot$ have already formed a significant density by this time. This further indicates that the

star formation and assembly history for galaxies is significant in the epochs $z > 9$, which we cannot probe in detail until the launch of JWST.

Table 3.4: Total stellar mass density estimates by integrating the best fit Schechter function from $M_* = 10^8$ to $10^{13} M_\odot$ for our GSMFs. The quoted 1σ error bars represent the minimum and maximum range of stellar mass densities within the 1σ contours of Schechter parameters obtained from our MCMC analysis. Also shown in the table are values of $\rho_{\rm UV}$ and $\rho_{\rm SFR}$. The $\rho_{\rm UV}$ values are integrated down to $M_{\rm UV} = -13.5$, the magnitude of the faintest galaxy in our sample. The SFR densities are calculated using the (Kennicutt, 1998) relation, assuming a Salpeter IMF and a constant SFH over $\geq$100 Myr. The values in the parentheses are computed using point sources in our completeness simulations.

z	log ρ_* ($M_\odot$Mpc^{-3})	log $\rho_{\rm UV}$ (erg s^{-1}Hz^{-1}Mpc^{-3})	log SFR density ($M_\odot$yr^{-1}Mpc^{-3})
6	$6.79^{+0.13}_{-0.12}$	$26.16^{+0.08}_{-0.07}$	$-1.69^{+0.08}_{-0.07}$
	$(6.57^{+0.13}_{-0.14})$	$(25.94^{+0.08}_{-0.07})$	$(-1.91^{+0.08}_{-0.07})$
7	$6.54^{+0.52}_{-0.55}$	$26.09^{+0.08}_{-0.08}$	$-1.76^{+0.08}_{-0.08}$
	$(6.28^{+0.55}_{-0.58})$	$(25.86^{+0.09}_{-0.09})$	$(-1.99^{+0.09}_{-0.09})$
8	$5.69^{+0.83}_{-0.81}$	$25.95^{+0.10}_{-0.09}$	$-1.90^{+0.10}_{-0.09}$
	$(5.38^{+0.84}_{-0.81})$	$(25.71^{+0.12}_{-0.10})$	$(-2.14^{+0.12}_{-0.10})$
9	$5.61^{+0.92}_{-0.90}$	$25.88^{+0.14}_{-0.13}$	$-1.97^{+0.14}_{-0.13}$
	$(5.25^{+0.94}_{-0.91})$	$(25.55^{+0.15}_{-0.14})$	$(-2.30^{+0.15}_{-0.14})$

3.6 Specific star formation rates

Previous studies have shown that the inclusion of emission lines in the estimation of stellar masses results in higher values of specific star formation rates (sSFR) at high redshift (e.g, Stark *et al.* 2013; González *et al.* 2014; Duncan *et al.* 2014; Schaerer & de Barros 2009, 2010). This is in contrast with the results from other studies such as Stark *et al.* (2009), González *et al.* (2010) and Bouwens *et al.* (2012) who show that the sSFR remains constant at $\sim$2 Gyr^{-1} with increasing redshift, and also with theoretical expectations of sSFR evolution (e.g., Davé 2008; Weinmann, Neistein & Dekel 2011). We therefore use our stellar mass and SFR estimates and investigate this further by calculating the sSFR (sSFR = SFR/M$_*$) of our sample in different redshift bins.

In order to compare with previous studies and to avoid incompleteness, we calculate our sSFR in a fixed stellar mass bin of $\log_{10}(M/M_\odot) = 9.7 \pm 0.3$. Fig. 3.12 shows our results along with the values of sSFR estimated in the same mass bin from the literature and show a clear trend of increasing sSFR with redshift. We find that our sSFRs are in good agreement with Duncan *et al.* (2014) and González *et al.* (2014) at $z \sim 6$ and $z \sim 7$, but are lower than Stark *et al.* (2013). However, it turns out that the scatter in the $\log_{10}(\mathrm{M}_*/\mathrm{M}_\odot) - \mathrm{M_{UV}}$ relation plays a crucial role in the estimated values of sSFR, in that the sSFR will be overestimated if only the $\log_{10}(\mathrm{M}_*/\mathrm{M}_\odot) - \mathrm{M_{UV}}$ relation is used without considering the numerous population of lower SFR sources with large mass-to-light ratios. Stark *et al.* (2013) do not take this into account and report their results considering zero scatter. Nevertheless, they discuss this and report that if the scatter of 0.5 dex described by González *et al.* (2012) is included, then this would lower the average sSFR by 2.8$\times$ at $z \sim 4$.

To understand the evolution of sSFR with redshift, we fit a power-law to the observed values of sSFR, giving us sSFR $\propto (1+z)^{2.01 \pm 0.16}$. This is still a weaker trend than the theoretical expectations of Dekel *et al.* (2013), in which the specific accretion rate follows the form sSFR $\propto (1+z)^{2.5}$, but is closer to that observed by Duncan *et al.* (2014) (sSFR $\propto (1+z)^{2.06 \pm 0.25}$).

In general, we find an increase in the sSFR when we probe galaxies at higher redshifts. This implies that there is a decline in the relative formation rate for galaxies at $z < 9$, and that the formation rate, relative to mass, increases at higher look back times.

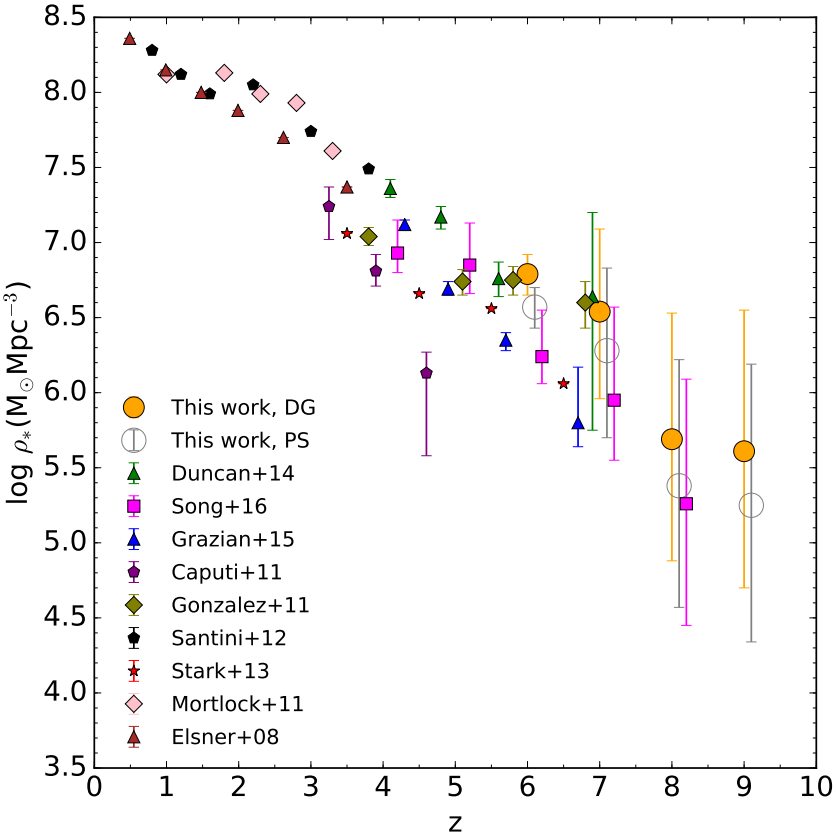


Figure 3.11: Evolution of total SMD as a function of redshift. We calculate the total SMD by integrating the best fit Schechter function from $M_* = 10^8$ to $10^{13} M_\odot$ for our GSMFs. The quoted 1σ error bars represent the minimum and maximum range of stellar mass densities within the 1σ contours of Schechter parameters obtained from our MCMC analysis. Our results are shown as solid orange points when disc-like galaxies are considered in our completeness simulations, and as open grey circles considering point sources. Shown also are the values from the literature converted to a Chabrier IMF, where necessary.

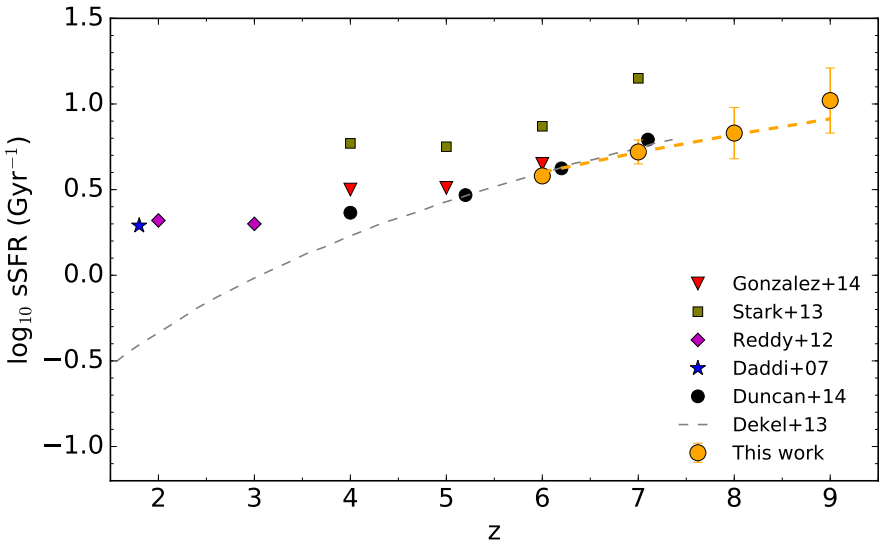


Figure 3.12: Biweight mean sSFR and error on the mean for galaxies in a fixed stellar mass bin of $\log_{10}(M/M_{\odot}) = 9.7 \pm 0.3$ as a function of redshift. The dashed yellow line is the best-fitting power law to the observed values of sSFR from $z \sim 6-9$. The theoretical model of Dekel *et al.* (2013) in which the specific accretion rate follows the form sSFR $\propto (1+z)^{2.5}$ is shown by dashed grey line.

3.7 UV luminosity density

To calculate the UV luminosity density ($\rho_{\rm UV}$) in each redshift bin, we integrate the best-fit Schechter parameters for our UV LFs down to a faint-end magnitude limit of $M_{\rm UV} = -13.5$, which is the magnitude of the faintest galaxy in our sample. Since dust extinction decreases with both redshift and UV luminosity (Bouwens *et al.* 2014a; Finkelstein *et al.* 2015), and hence has a negligible effect on estimated $\rho_{\rm UV}$ values, we do not dust correct the data while calculating the UV luminosity density. We then use the Kennicutt (1998) relation to convert the UV luminosity density values to cosmic star formation rate density (SFRD), assuming a Salpeter IMF and constant SFH over $\geq$100 Myr .

In order to facilitate comparison with other studies such as Bouwens *et al.* (2015b), Finkelstein *et al.* (2015), McLeod, McLure & Dunlop (2016), Ishigaki *et al.* (2018) and Oesch *et al.* (2018), we also estimate $\rho_{\rm UV}$ down to $M_{\rm UV} = -17$. Fig. 3.13 shows the evolution of UV luminosity density as well as SFR density from $z = 6-9$ and Table 3.4 shows the derived values of $\rho_{\rm UV}$ and $\rho_{\rm SFR}$ in each redshift bin. In both the cases ($M_{\rm UV} = -13.5$ and $M_{\rm UV} = -17$) our results support a smooth decline of $\rho_{\rm UV}$ towards high redshifts when disc-like galaxies are considered in our completeness simulations. However, there appears to be a slight accelerated decline of $\rho_{\rm UV}$ and $\rho_{\rm SFR}$ when using completeness results with point sources (See Fig. 3.13).

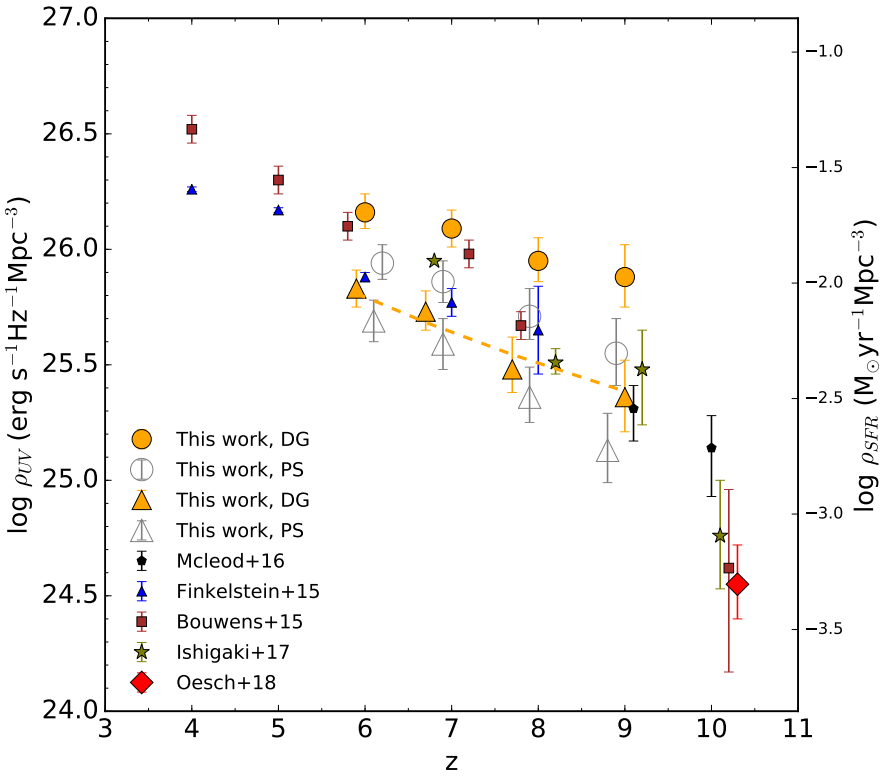


Figure 3.13: Evolution of UV luminosity density as a function of redshift. $\rho_{\rm UV}$ values calculated with a $M_{\rm UV} = -13.5$ limit are shown in orange filled circles and $\rho_{\rm UV}$ calculated using a $M_{\rm UV} = -17$ limit are shown in orange filled triangles. Also shown are the $\rho_{\rm UV}$ estimates considering point sources in our completeness simulations with open grey circles and open grey triangles for $M_{\rm UV} = -13.5$ and $M_{\rm UV} = -17$ respectively. The dashed yellow line is the power-law fit to the data points at $z \sim 6-9$, such that $\rho_{\rm UV} \propto (1+z)^{-2.63}$. Fitting a power-law at $z \geq 8$ values results in $\rho_{\rm UV} \propto (1+z)^{-4.61}$ (not shown).

The values estimated with point sources are shown in parentheses in Table 3.4. The quoted 1σ uncertainties represent the minimum and maximum range of $\rho_{\rm UV}$ and $\rho_{\rm SFR}$ within the 1σ contours of Schechter parameters obtained from our MCMC analysis in Section 3.2.1.

Performing a simple power-law fit to the data points estimated with disc-like galaxies at $z \sim 6-9$, we find that $\rho_{\rm UV} \propto (1+z)^{-2.63}$ (shown by dotted yellow line in Fig. 3.13), whereas fitting a power-law at $z \geq 8$ values results in $\rho_{\rm UV} \propto (1+z)^{-4.61}$. This is even shallower than (McLeod, McLure & Dunlop, 2016) who find that $\rho_{\rm UV} \propto (1+z)^{-5.8}$ beyond $z \simeq 8$, supporting a smooth decline in $\rho_{\rm UV}$. This is in contrast with Oesch *et al.* (2014), Bouwens *et al.* (2015b), Ishigaki *et al.* (2018) and Oesch *et al.* (2018) who find an accelerated decline in $\rho_{\rm UV}$ at $z \geq 8$ when they integrate it down to $M_{\rm UV} = -17$.

3.8 Summary

In this chapter we have exploited the power of gravitational lensing of massive clusters to probe galaxy evolution with galaxy stellar mass functions and UV luminosity functions out to z∼9.

We have used the stellar masses of our high-z sample estimated in Chapter 2 and have derived, for the first time, the GSMF at $z = 6 - 9$ for the HFF program. Using the same sample, we have also derived the UV LF at $z = 6-9$. For our high-z sample, we have utilized the star formation rates estimated in Chapter 2 and have calculated the sSFR and cosmic star formation rate density in the redshift range probed. Our key conclusions are as follows:

1. Our new measurements of the GSMF show an apparent steepening of the low mass end slope α with increasing redshift ($-1.98^{+0.07}_{-0.07}$, $-2.01^{+0.17}_{-0.13}$, $-2.30^{+0.51}_{-0.46}$ and $-2.38^{+0.72}_{-0.88}$ at $z = 6, 7, 8$ and 9 respectively) within the error bars, statistically steeper than previously observed mass functions at slightly lower redshifts, and we find no evidence of a turnover in the mass range probed. We also find a decrease in normalization Φ^* with increasing redshift, but no evolution in characteristic mass M^* is observed.

2. The faint-end slope of the UV LF also exhibit an apparent steepening with increasing redshift (from $-2.03^{+0.12}_{-0.10}$ at $z = 6$ to $-2.20^{+0.51}_{-0.47}$ at $z = 9$), without any evidence of a turnover. These measurements are consistent with a continuation of the trends seen from lower redshift, however more data is needed to confirm the trend at these redshifts. The normalization Φ^* of UV LF decreases with increasing redshift and a weak evolution in $M^*_{\rm UV}$ is also observed, with it decreasing with redshift, implying that the evolution of the UV luminosity function with redshift appears to be more consistent with an evolution of density.

3. The slopes of our best fitted $\log_{10}(\rm M_*/M_\odot) - \rm M_{UV}$ relation are close to a constant mass-to-light ratio of -0.40, suggesting no strong evolution of mass-to-light ratio with luminosity. We notice that normalization, on the other hand, evolves very weakly from $z \sim 6$ to $z \sim 9$, with a decrease in normalization with increasing redshift.

4. From our new measurements of the GSMF, we estimate the stellar mass density and find that the integrated SMD has increased from $\log_{10}\rho_* = 5.61^{+0.92}_{-0.90}$ $\rm M_\odot Mpc^{-3}$ at $z = 9$ to $\log_{10}\rho_* = 6.79^{+0.13}_{-0.12}$ $\rm M_\odot Mpc^{-3}$ at $z = 6$.

5. We estimate the specific star formation rates (sSFR = SFR/M$_*$) of our sample, and find that for a fixed stellar mass of $5 \times 10^9 M_\odot$, sSFR $\propto (1+z)^{2.01 \pm 0.16}$.

6. From our new measurements, we estimate the UV luminosity density ($\rho_{\rm UV}$) and the cosmic star formation rate density ($\rho_{\rm SFR}$), and find that our results support a smooth decline of $\rho_{\rm SFR}$ towards high redshifts.

Chapter 4

Evolution of the Galaxy Rest-frame UV Colours

In this chapter, the evolution of the galaxy rest-frame UV colours is examined for the sample of our high redshift galaxies at $z = 6 - 9$ in the MACSJ0416 cluster and its parallel field. This chapter is, to date, unpublished material.

4.1 Introduction

At the highest redshifts, where only the rest-frame UV (dominated by emission from the most massive, young but short-lived hot stars), is currently accessible at high resolution imaging, one of the few diagnostics of the physical properties of galaxies available is the UV colour, which is sensitive both to dust and metallicity. The investigation of the metallicities of the early galaxies can be carried out through the measurement of the UV spectra slope, β, such that the UV spectral energy distribution has the form $f_\lambda \propto \lambda^\beta$ ((Calzetti, Kinney & Storchi-Bergmann, 1994)). It has been also found that these slopes are strongly correlated with dust extinction in galaxies at low redshift (e.g., Meurer *et al.* 1995, 1997; Meurer, Heckman & Calzetti 1999) as well as at high redshift, at $z \sim 2$ (e.g., Daddi *et al.* 2004; Reddy *et al.* 2012) and therefore can be used to measure dust obscuration at even higher redshifts.

The UV continuum slope β has been extensively studied at high redshift ($z \sim 2 - 6$). For example, Bouwens *et al.* (2009) reported a strong evolution in β from -1.5 at $z \sim 2$ to -2.4 at $z \sim 6$. In their study, they also found that lower luminosity galaxies appeared to be bluer than higher luminosity galaxies. Similarly, Wilkins *et al.* (2011) used single colours to measure the rest-frame UV colours of galaxies at $4.7 < z < 7.7$ and found the mean UV continuum colours to be approximately

equal to zero (AB) for their highest redshift sample. At lower redshift, on the other hand, they find that the mean UV continuum colours of galaxies are redder and also find that galaxies with higher luminosities are also slightly redder on average. At $z \sim 7$, Bouwens *et al.* (2010) measured β for their sample of galaxies, finding that the very low luminosity galaxies exhibited UV continuum slopes as steep as $\beta = -3$. Finkelstein *et al.* (2010) also reported similar steep values of β at $z \sim 6-7$, albeit with larger uncertainties.

Contrary to this, McLure *et al.* (2011) and Dunlop *et al.* (2012) find a variance-weighted mean value of $\beta \sim -2$ at $z \sim 7$, and also find that β shows no significant trend with either redshift or $M_{\rm UV}$. In another study, Bouwens *et al.* (2012) measured UV continuum slopes at $z \sim 4-7$ and found that β measurements for faint sources are likely to suffer large biases if the same passbands are used to select the sources as well as to measure β. They find that their high redshift galaxies show a well-defined rest-frame UV colour–magnitude (CM) relationship that becomes systematically bluer toward fainter UV luminosities and that the dust extinction is zero at low luminosities and at high redshifts. Alternatively, Finkelstein *et al.* (2012) reported no significant evolution of β for galaxies at all luminosities while studying the GOODS-South and HUDF09 surveys at $z = 4-8$. However, they do suggest a significant correlation with stellar mass, in that more massive galaxies appeared redder. More recently, Bouwens *et al.* (2014b) measured a significant colour magnitude relation with the fainter galaxies displaying bluer slopes, and the relation was found to steepen at at $z = 4-8$.

Regardless of the varying results, the general consensus now is that values of $\beta \simeq -2$ are prevalent for even the faintest galaxies detected with *HST*, out to at least $z = 8$, and at high redshift the dust extinction is significantly less than at lower redshift. However, the numbers of such faint sources are still very small (~ 30 in the HUDF plus its two parallel fields), and only exist at $M_{\rm UV} < -18$. The HFF has pushed the limits of current facilities, using gravitational lensing to boost the fluxes of faint galaxies into view, and can offer the first insight into the rest-frame UV colours of galaxies at $-17 < {\rm M_{UV}} < -13$. This is particularly exciting as models predict that galaxies with $\beta \sim -3$ only exist at ${\rm M_{UV}} > -17$ (Dunlop *et al.*, 2013).

Should we detect such blue slopes from these galaxies, we will potentially discover the first evidence for very low-metallicity star-formation in the early Universe. With the subtraction method that we have developed, we have been able to probe magnitudes as faint as $M_{\rm UV} = -13.5$. In this chapter, I will therefore use this data to understand how β is evolving over redshift range $z = 6-9$ and UV luminosity in a reasonably wide range $-22 < {\rm M_{UV}} < -13$.

4.2 Method

4.2.1 Estimating β

The UV continuum, approximately between 1250 Angstrom and 2600 Angstrom, was first parametrized by Calzetti, Kinney & Storchi-Bergmann (1994) as a power law of the form $f_\lambda \propto \lambda^\beta$ to study the effects of dust extinction in galaxies. The UV spectral slope β was designed to be measured from spectra in specified wavelength windows defined by Calzetti, Kinney & Storchi-Bergmann (1994). However, because continuum spectroscopy is extremely difficult at high redshift, β is commonly determined by three main methods, each with its own advantages and disadvantages.

The first method is where one fits a power-law to all the available photometry redward of the Lyman break to measure β (e.g., Bouwens *et al.* 2014a). A direct fit to the photometry can hence allow for measurements of β for faint galaxies that are close to the detection limit. Translating the $f_\lambda \propto \lambda^\beta$ relation into magnitude units gives a linear relationship between β and colours. Therefore, another way of estimating β is via a single colour (e.g., Dunlop *et al.* 2012; Hathi, Malhotra & Rhoads 2008). The third method of calculating β is by performing SED fitting (e.g., Finkelstein *et al.* 2010, 2012). In this method, single stellar population models are first constructed by varying parameters such as age, metallicity, star formation history and dust. The best-fit model is then found via χ^2 minimization, and the value of β is measured directly from this best-fit spectrum by fitting a power law to the spectrum using the 10 wavelength windows specified by Calzetti, Kinney & Storchi-Bergmann (1994). The advantage of this method is that because all the available photometric bands are used, this should yield more robust estimates of β. The disadvantage, however, is that because this method is based on synthetic models, one is confined to a limited range of β allowed by the models. Therefore, this method may not be suitable to the population of objects close to the epoch of first star formation that may have unique spectral features.

In our work, because we have multiple photometric bands, and hence multiple rest-frame UV colours redward of the Lyman break, we choose to use the SED fitting method and follow the procedure described in Finkelstein *et al.* (2012), who show with the help of simulations that SED fitting is a superior choice over the other two methods. Briefly, to measure β, we perform SED fitting on our sample of high redshift galaxies at $z = 6 - 9$ to find the best fitting synthetic stellar population models of Bruzual & Charlot (2003). Single stellar population models of Bruzual & Charlot (2003) are first used to generate synthetic SEDs for a user-

defined combination of parameters such as metallicity, age, dust and star formation history (SFH), assuming a Chabrier IMF (Chabrier, 2003). The ages are allowed to vary from 5 Myr up to the age of the Universe at the redshift step being fit, dust attenuation is varied in the range $0 \leq A_v \leq 2$, and metallicities of 0.02, 0.2 and 1 $Z_\odot$ are used. The widely adopted parametrization of the SFH (SFR $\propto e^{-t/\tau}$) is used with $\tau = 0.05, 0.25, 0.5, 1, 2.5, 5, 10, -0.25, -0.5, -1, -2.5, -5, -10$ and 1000 (constant SFR) Gyr, where negative τ values represent exponentially increasing histories. We also apply nebular emission lines on the model SEDs, assuming an escape fraction of $f_{\rm esc} = 0$ (See Duncan *et al.* 2014 for a detailed description of the method for including nebular emission lines). Dust extinction is then applied using the law described by Calzetti *et al.* (2000).

We then find the best-fit model via χ^2 minimization, and measure the value of β directly from this best-fit spectrum by fitting a power law to the spectrum using the 10 wavelength windows specified by Calzetti, Kinney & Storchi-Bergmann (1994). For each model, we also compute the absolute magnitude at 1500 Angstrom by fitting a 100 Å-wide top-hat filter centered on 1500 Å.

In order to estimate the uncertainty on β, we perform a Monte Carlo analysis in which the observed flux of each source was perturbed by randomly choosing a point from a Gaussian distribution with standard deviation equal to the 1σ uncertainty on the flux in a given filter. The UV slope β for each source is then estimated with the simulated photometry by deriving a best-fit model. This process is repeated 500 times and the final uncertainty is then taken as the standard deviation of the distribution of these 500 values.

Fig. 4.1 shows the estimated values of the UV slope β for each of our high redshift sources at $z = 6 - 9$. Since at fainter magnitudes and at higher redshifts the uncertainty on the value of β for individual galaxy is large, we follow Finkelstein *et al.* (2012) and compute the median values of β in three different bins, separated by 25 per cent and 75 percent of the evolving values of the characteristic magnitude L^*, using our derived luminosity functions. These median values of β are shown by black circles in Fig. 4.1. Similarly, in Table 4.1 we list the median values of β in all three luminosity bins as well as for all the galaxies in each redshift bin, along with the median M_{1500} values.

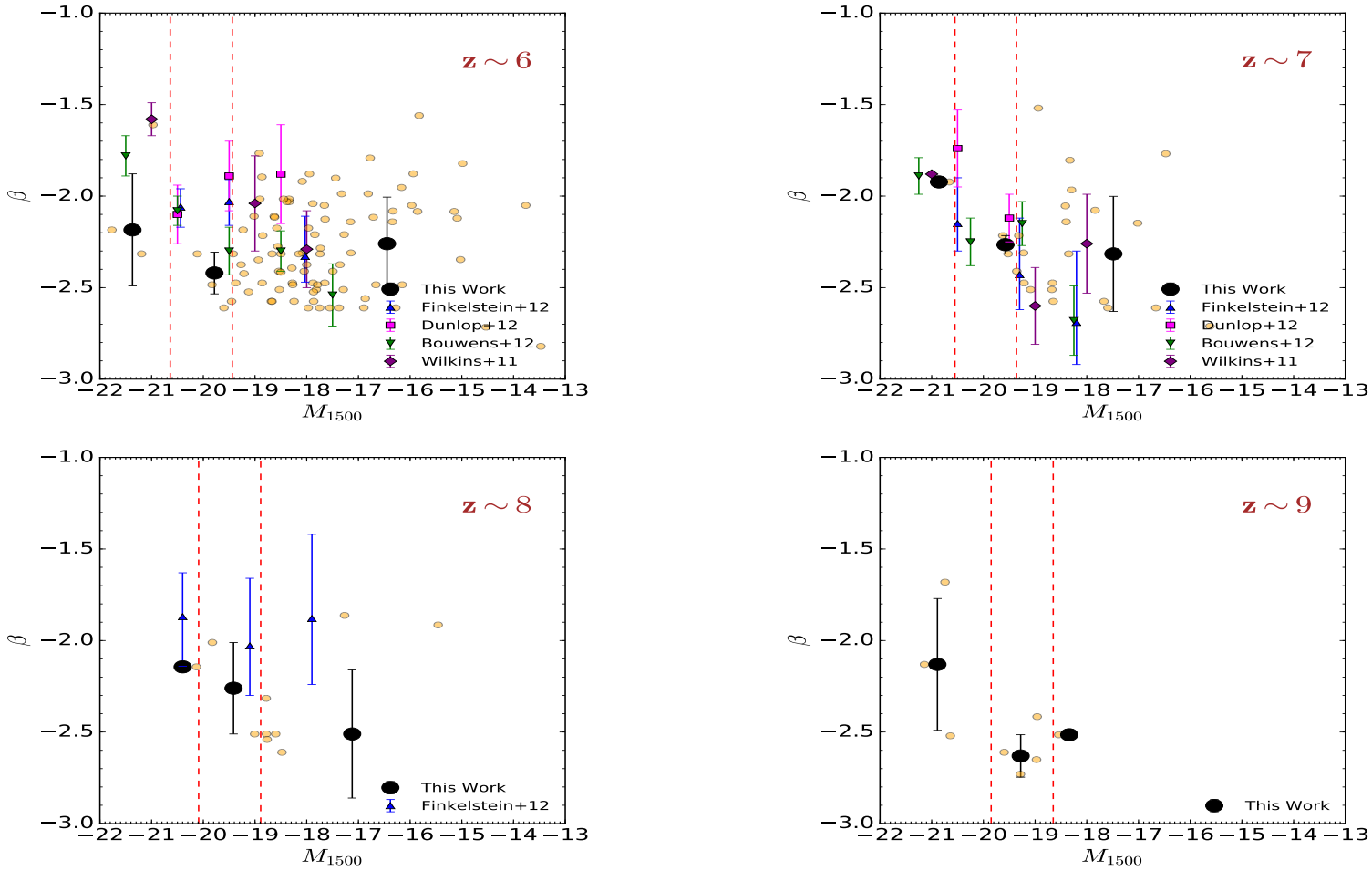


Figure 4.1: The estimated UV slope β vs absolute magnitude at 1500 Angstrom at $z = 6 - 9$. The filled yellow circles show the results for individual galaxies, whereas the black circles show the median value of β measured in three different bins separated by the dashed lines, denoting the evolving values of 0.25 L^* and 0.75 L^*, similar to Finkelstein *et al.* (2012), with the uncertainties being the errors on the median.

Table 4.1: Median values of the UV spectral slope β

z	Median β All galaxies	Median β $L > 0.75L^*$	Median β $0.25L* < L < 0.75L*$	Median β $L < 0.25L^*$	Median M_{1500} All galaxies
6	-2.24 ± 0.18	-2.18 ± 0.30	-2.42 ± 0.11	-2.26 ± 0.25	-17.95
7	-2.31 ± 0.22	-1.92 ± 0.03	-2.26 ± 0.05	-2.31 ± 0.31	-18.53
8	-2.41 ± 0.28	-2.14 ± 0.03	-2.26 ± 0.25	-2.51 ± 0.35	-18.77
9	-2.52 ± 0.34	-2.13 ± 0.36	-2.63 ± 0.21	-2.51 ± 0.03	-19.44

4.2.2 Testing the method

To test the quality of our method of measuring β, we build a custom mock catalog of high redshift galaxies using the Theoretical Astrophysical Observatory (TAO) (Bernyk *et al.*, 2016). To build our mock photometry catalog, we use the existing CANDELS mock cone from redshift $z = 0$ to $z = 9$ on the TAO and generate SEDs from the single stellar populations of Bruzual & Charlot (2003), using the initial mass function of Chabrier (2003) similar to our selection efficiency method in Section 2.3.5.2. Dust is then applied using the dust model of Calzetti *et al.* (2000) and the final catalog is made with a H-band distribution of magnitudes in the range $21 < H_{160} < 35$, such that the magnitudes in the rest of the filters are determined based on the range of H band magnitudes.

In order to generate errors for the mock photometry catalog, we bin the fluxes of sources from our real catalog and calculate the standard deviation and mean of the flux errors in those bins, giving us a Gaussian distribution of the errors. Photometric errors for each filter in the mock catalog were then simulated by picking random errors each time from the Gaussian distribution in the corresponding bins. We then run EAZY on this mock catalog and compute the photometric redshifts.

Finally, we pass the high redshift sources from the mock catalog through the same sample selection criteria (See Section 2.3.4.2) as our real sample. By doing this, we ensure that mock galaxies best match the properties of the galaxies in our true sample. We then perform SED fitting on these mock galaxies in the same way as on our real sample to measure β. Fig. 4.2 shows the results of these simulations at $z = 6-9$, showing the difference between the input value of the UV spectral slope β and that recovered from SED fitting as a function of input H_{160} magnitude. The orange circles represent the mean difference between simulated and observed values of β as well as the scatter in bins of $\Delta m = 1$. As expected, through these simulations we find that the scatter increases at higher redshifts and at faint magnitudes (See Fig. 4.2), but is generally quite good at recovering the correct values of β.

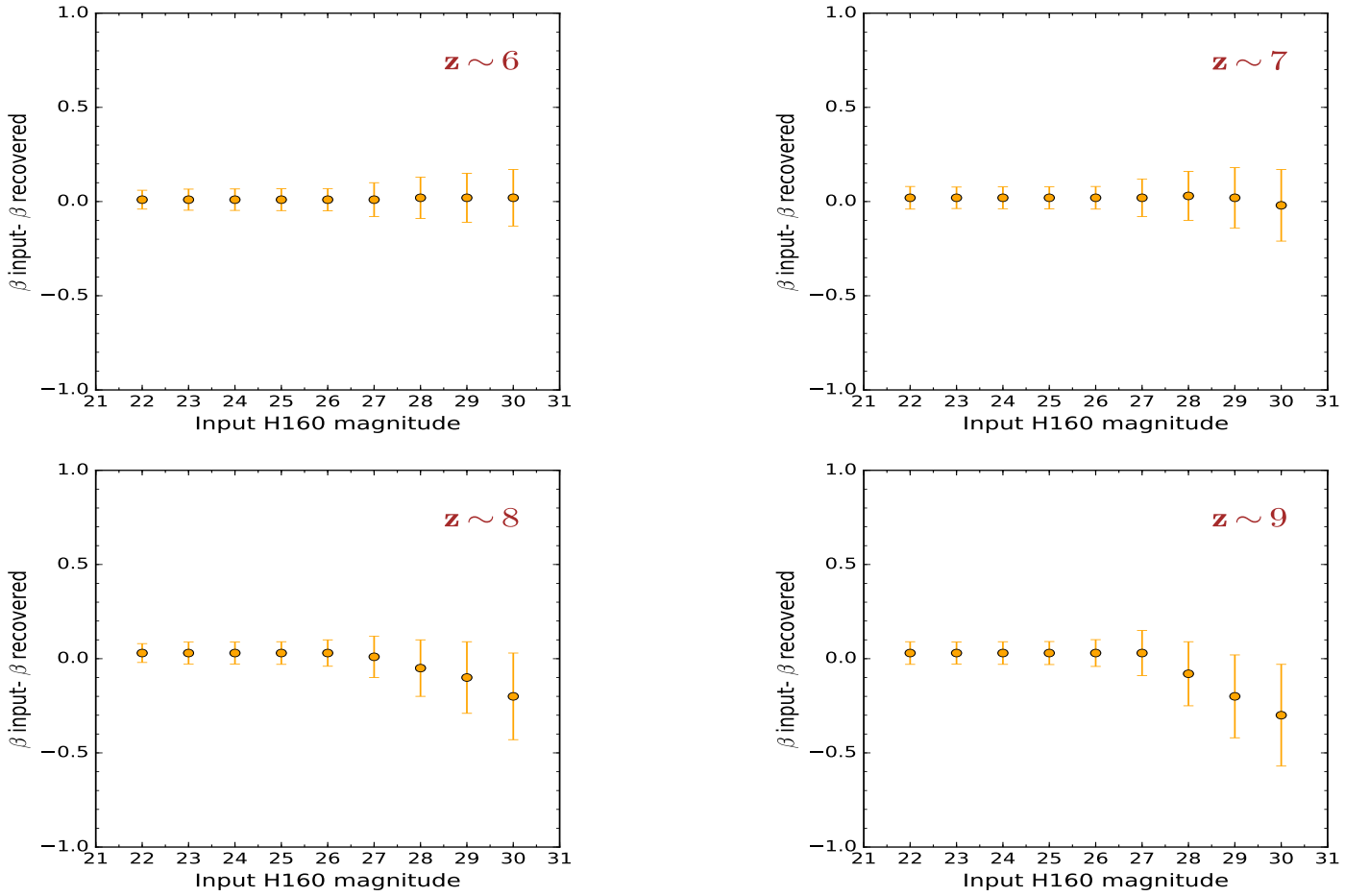


Figure 4.2: Results of our simulations at $z = 6 - 9$, showing the difference between the input value of the UV spectral slope β and that recovered from SED fitting as a function of input H_{160} magnitude. The orange circles represent the mean difference between simulated and observed values of β as well as the scatter in bins of $\Delta m = 1$.

4.3 Results

4.3.1 Correlation of β with M_{1500}

As seen from Fig. 4.1, we do not find a correlation between β and rest-frame UV magnitude M_{1500} at $z = 6$ and $z = 7$ and $z = 9$, but there appears be some correlation at $z = 8$, in that fainter galaxies have bluer values of β. This is in agreement with Dunlop *et al.* (2012) and Finkelstein *et al.* (2012) who also do not find a correlation between β and UV magnitude at $z = 5 - 7$ and $z = 4 - 8$ respectively.

However, the results are in disagreement with previous work of Bouwens *et al.* (2009) who derive their UV slopes β using single-colour and find lower luminosity galaxies to be bluer than higher luminosity galaxies at $z \sim 2.5$ and $z \sim 4$. A similar relation was found by Wilkins *et al.* (2011) who use near-infrared (near-IR) imaging to measure the rest-frame UV continuum colours of galaxies at $4.7 < z < 7.7$ using single-colour technique. Bouwens *et al.* (2012) determined the UV continuum slopes at $z \sim 4 - 7$ by fitting a power law to the observed photometry and report a well-defined rest-frame UV colour–magnitude relationship that becomes systematically bluer towards fainter UV luminosities.

As stated earlier, we follow the method of Finkelstein *et al.* (2012) and derive our UV slopes using an SED fitting method and also measure $M_{\rm UV}$ by fitting a 100 Å-wide top-hat filter centered on 1500 Angstrom (See Section 4.2). Bouwens *et al.* (2012)) probe different parts of the rest-frame UV depending on the redshift, whereas we are always probing rest-frame 1500 Angstroms. As pointed out in Finkelstein *et al.* (2012), the way we measure $M_{\rm UV}$ may have an effect on whether any dependence between β and $M_{\rm UV}$ is observed (Refer Finkelstein *et al.* 2012 for more details). Similarly, the way the colours are estimated in other studies is also likely the reason for the disagreement in the results.

4.3.2 Evolution of β with redshift

From Fig. 4.1, we find that there is no significant correlation of β with UV luminosity. We now therefore proceed to understand if there is any evolution of β with redshift by plotting the median β values of all galaxies as a function of redshift. To do this, we first interpolate the results from previous literature at the median value of M_{1500} for our sample. As seen from Fig. 4.3, β appears to evolve weakly ($\sim 0.7\sigma$) from $\beta = -2.24$ at $z \sim 6$ to $\beta = -2.52$ at $z \sim 9$, presumably due to increased dust extinction. To quantify this evolution, we fit a first-order polynomial through the

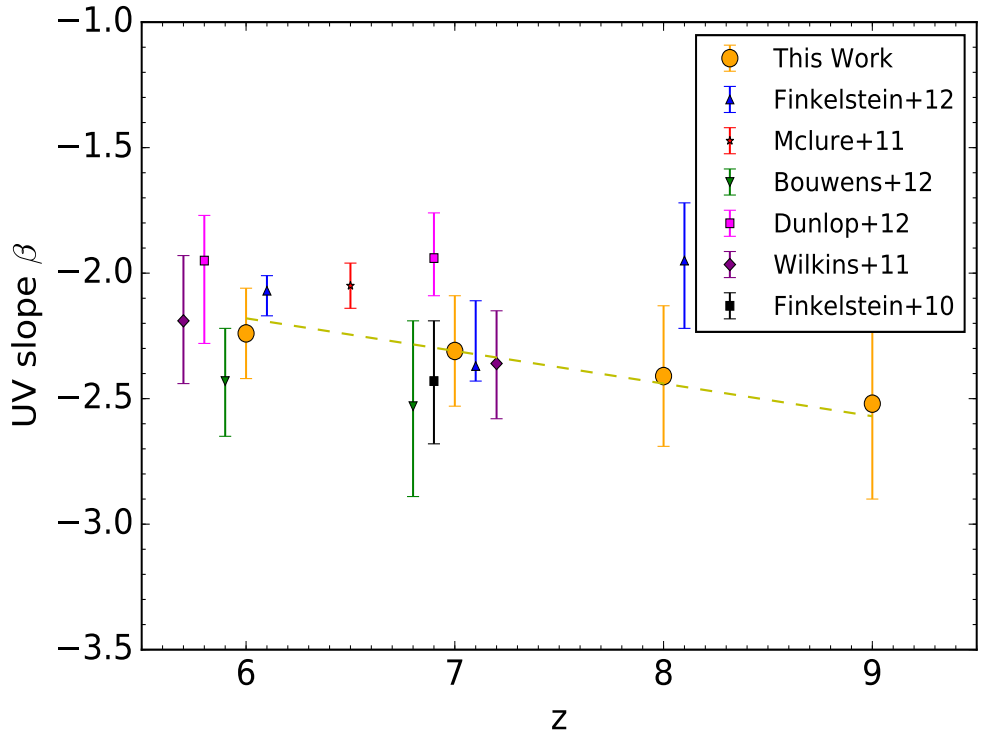


Figure 4.3: The evolution of the median β of all galaxies in each redshift bin, shown in yellow circles. The median M_{1500} for these points are -17.95, -18.53, -18.77, and -19.44 at $z = 6$, $z = 7$, $z = 8$, and $z = 9$ respectively. Shown also are the results from the literature interpolated to represent the results at the median value of M_{1500} for our sample. The dashed yellow shows a linear fit through the median β points. A weak evolution in β from $z = 9$ to $z = 6$ is observed, presumably due to increased dust extinction.

median β data points at each redshift, revealing a slope of -0.13 ± 0.05, shown by dashed yellow line in Fig. 4.3.

Comparing our estimated values of β with previous work, such as Finkelstein *et al.* 2012; Bouwens *et al.* 2009, 2012; Wilkins *et al.* 2011, we find that our results are in agreement with them, in that galaxies get bluer at higher redshift. However, our results are not in agreement with Dunlop *et al.* (2012) who studied the UV colours of galaxies at $z > 6$ in the HUDF, ERS and HUDF09-2 fields, and reported an average value of $\beta = -2.05 \pm 0.1$ at all redshifts. Our β values are bluer than theirs at all redshifts. Although, we note that they apply a stringent selection criteria and restrict their sample to contain objects that have at least one 8σ near-IR detection in the WFC3/IR data, which may have excluded many of the faint galaxies, causing β to have a redder value.

At $z \sim 6$ our β values are bluer than Finkelstein *et al.* (2012) and Wilkins *et al.* (2011), but redder than Bouwens *et al.* (2012). Comparing at ~ 7, our estimated UV

slopes are redder than Finkelstein *et al.* (2010), Finkelstein *et al.* (2012),Bouwens *et al.* (2012), Wilkins *et al.* (2011) and McLure *et al.* (2011). Finally, at $z \sim 8$ the only data point to compare with from the literature is Finkelstein *et al.* (2012), who report a redder value than us. These differing results are likely due to our use of all the photometric bands, including data from VLT and *Spitzer*, yielding more robust estimates of β.

4.3.3 β of faint galaxies

At $z \sim 7$, Bouwens *et al.* (2010) measured β for their sample of galaxies, finding that the very low luminosity galaxies exhibited UV continuum slopes as steep as -3 and argued the likelihood of the presence of extremely metal-poor stars or a top–heavy IMF in these galaxies, supporting that such exotic populations might be crucial to yield such blue values. Finkelstein *et al.* (2010) also reported similar steep values of β at $z \sim 6-7$ by examining the same dataset, albeit with larger uncertainties, and therefore concluded that exotic populations were not necessary for such bluer values of UV slope β. Furthermore, with the help of simulations, Dunlop *et al.* (2012) showed that there is a bias towards artificially blue slopes for faint galaxies and argued that the very blue colours are likely overestimated. To look into this in more detail, with the help of an improved dataset and with SED fitting method, Finkelstein *et al.* (2012) re-examined this and reported a value of $\beta = -2.68^{+0.39}_{-0.24}$ for faint galaxies at $z \sim 7$, redder than their previously reported results.

In this work, we employ the SED fitting method similar to Finkelstein *et al.* (2012) but also use all the photometric bands, including data from VLT and *Spitzer*, to derive the UV slopes for our sample of galaxies. As shown in Table 4.1, $z \sim 7$ the bluest value of our sample is $\beta = -2.31 \pm 0.31$, which is redder than Finkelstein *et al.* (2012) and Bouwens *et al.* (2010). Additionally, with the help of our SED fitting method, we derive the UV slopes for the first time at $z \sim 9$ and find that our bluest data point has a value of $\beta = -2.63 \pm 0.21$ at $z \sim 9$ (See Table 4.1), finding no evidence as yet for extreme stellar populations at $z > 6$.

4.3.4 Correlation of β with stellar mass

From Fig. 4.1 we determine that there is no strong correlation of β with UV luminosity. In this section, we therefore proceed to find whether there exists any trend between β and stellar mass. To do this, we use the stellar masses estimated for our sample of high redshift galaxies at $z = 6-9$ in Chapter 2, and plot β as a

function of redshift, as shown in Fig. 4.4. Here, we compute the median values of β in different mass bins of $6 < \log M/M_{\odot} < 7$, $7 < \log M/M_{\odot} < 8$, $8 < \log M/M_{\odot} < 9$, $9 < \log M/M_{\odot} < 10$ and $10 < \log M/M_{\odot} < 11$, similar to Finkelstein *et al.* (2012). The median values of β are as listed in Table 4.2.

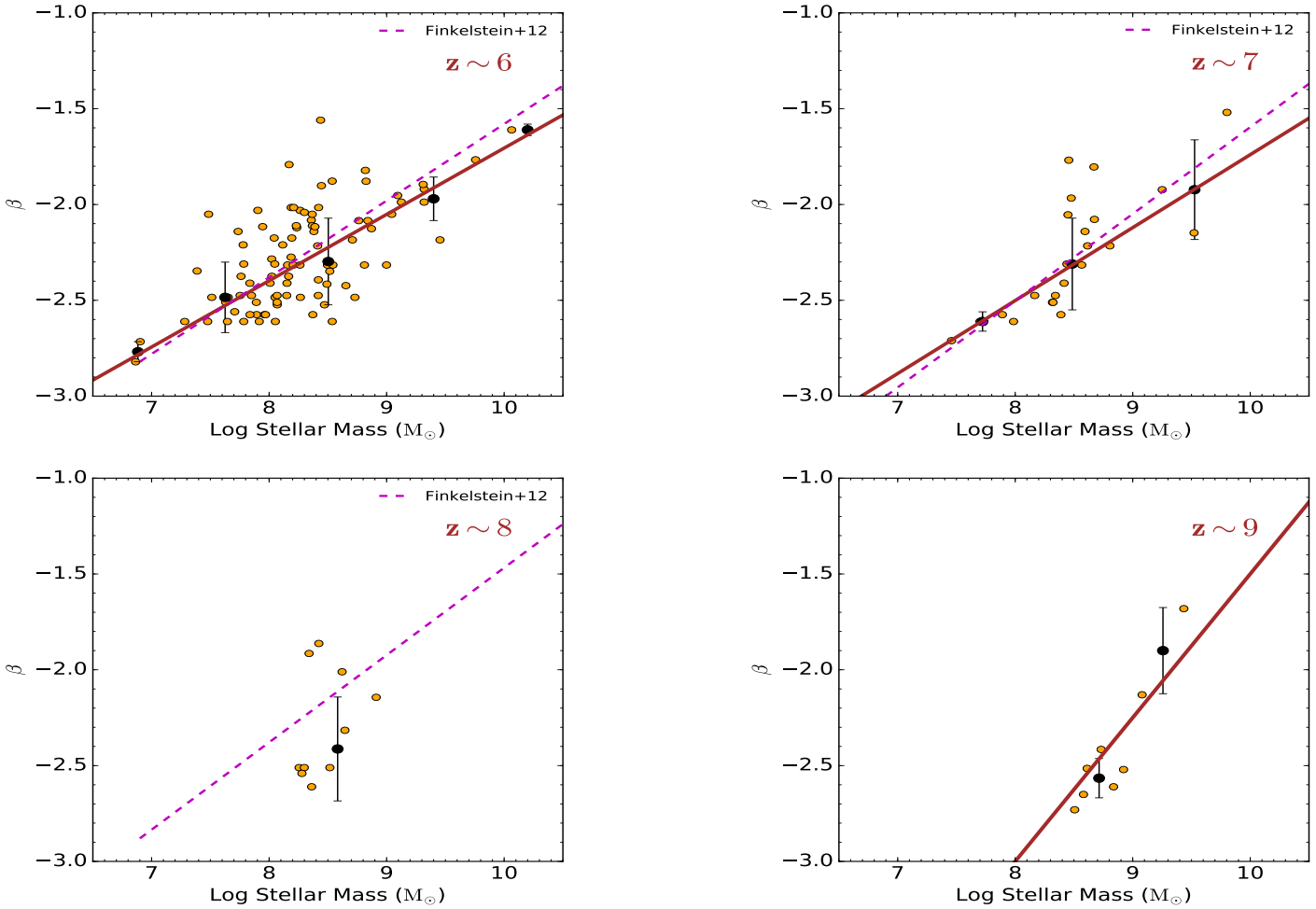


Figure 4.4: Estimated UV slope β vs stellar mass at $z = 6 - 9$. The filled yellow circles show the results for individual galaxies, whereas the black circles show the median value of β in each stellar mass bin of $1M_{\odot}$. The solid red lines shows a linear fit through the median β points. There is a strong correlation between β and stellar mass in all redshift bins, in that lower mass galaxies exhibit bluer UV slopes. The best-fit lines of Finkelstein *et al.* (2012) are also shown by dashed magenta lines for comparison.

Table 4.2: Median values of the UV spectral slope β in different mass bins.

z	Median β $\log M/M_\odot = 6-7$	Median β $\log M/M_\odot = 7-8$	Median β $\log M/M_\odot = 8-9$	Median β $\log M/M_\odot = 9-10$	Median β $\log M/M_\odot = 10-11$	β - stellar Mass slope
6	-2.77 ± 0.05	-2.48 ± 0.18	-2.30 ± 0.23	-1.97 ± 0.11	-1.61 ± 0.03	0.35 ± 0.18
7	..	-2.61 ± 0.05	-2.31 ± 0.24	-1.92 ± 0.26	..	0.38 ± 0.20
8	..	..	-2.41 ± 0.27	..	..	..
9	..	..	-2.56 ± 0.10	-1.90 ± 0.22	..	0.75 ± 0.40

As seen in Fig. 4.4, we observe a strong correlation between β and stellar mass, in that lower mass galaxies exhibit bluer UV slopes. To quantify this, we fit a first-order polynomial through the median data points at each redshift to estimate the slope and its associated uncertainty. The best-fit line at each redshift, except $z = 8$ since there is only one median data point, is shown Fig. 4.4, and the values of the slope along with its uncertainty are listed in Table 4.2. We also show the best-fit lines of Finkelstein *et al.* (2012) in Fig. 4.4 for comparison.

To investigate this further, we once again plot β as a function of redshift, by spliting our sample into the same mass bins; $6 < \log M/M_\odot < 7$, $7 < \log M/M_\odot < 8$, $8 < \log M/M_\odot < 9$, $9 < \log M/M_\odot < 10$ and $10 < \log M/M_\odot < 11$, as shown in Fig. 4.5.

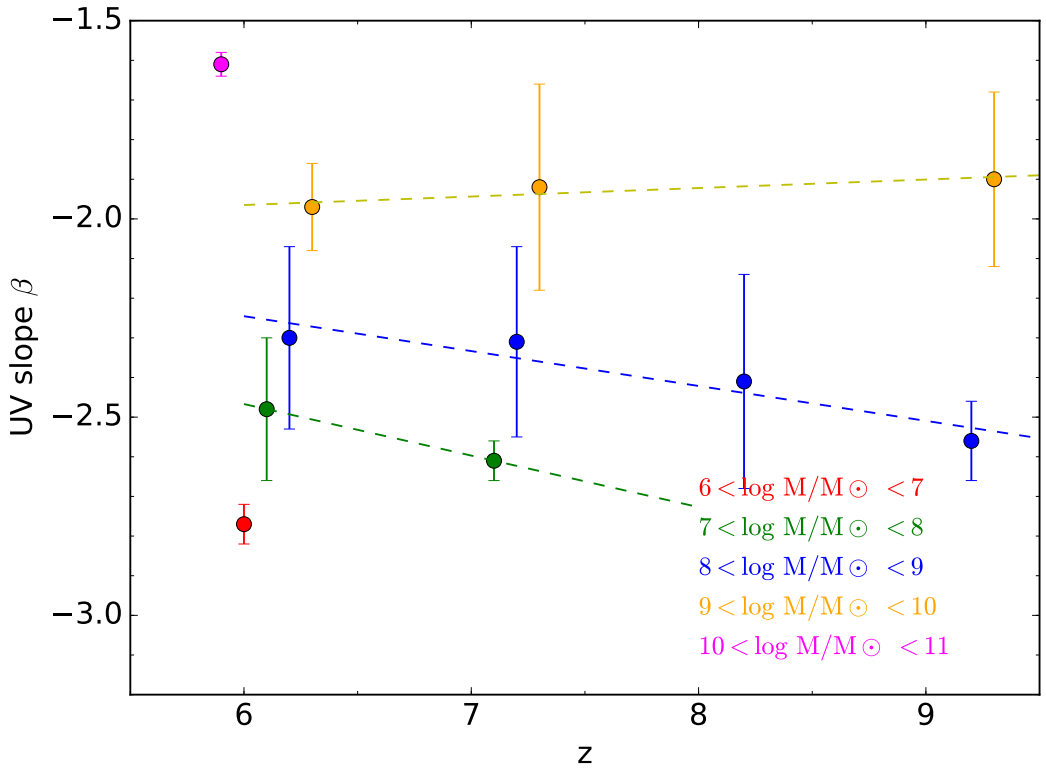


Figure 4.5: Evolution of median value of UV spectral slope β in different mass bins with redshift. The red circle shows the median β in mass bin $6 < \log M/M_\odot < 7$, green circles show the median β in mass bin $7 < \log M/M_\odot < 8$, blue circles show the median β in mass bin $8 < \log M/M_\odot < 9$, yellow circles show the median β in mass bin $9 < \log M/M_\odot < 10$ and finally the magenta circle shows the median β in mass bin $10 < \log M/M_\odot < 11$. It appears that low mass galaxies at $\log M/M_\odot < 9$ become bluer with increasing redshift, whereas the massive galaxies at $\log M/M_\odot > 9$ appear to exhibit a nearly constant β at each redshift.

Examining the plot, it appears that low mass galaxies at $\log M/M_\odot < 9$ become bluer with increasing redshift ($\sim 1\sigma$ correlation), whereas the massive galaxies at

$\log M/M_{\odot} > 9$ appear to exhibit a nearly constant β at each redshift. Finkelstein *et al.* (2012) notice a similar effect and suggest that this is likely because dust can build up fairly rapidly in massive galaxies and that most massive galaxies retain this dust, whereas dust is presumably getting removed from low mass galaxies due to feedback.

We furthermore measure the evolution of the median value of UV spectral slope β by fitting a first-order polynomial through the points in $7 < \log M/M_{\odot} < 8$, $8 < \log M/M_{\odot} < 9$, and $9 < \log M/M_{\odot} < 10$ mass bins (shown by green, blue and orange dashed lines in Fig. 4.5), revealing a slope of -0.18 ± 0.10, -0.13 ± 0.07 and 0.02 ± 0.01 respectively. However, we do note that completeness might be playing a role here, in that low-mass blue galaxies are easier to discover in our data than low-mass red galaxies. These results are in good agreement with Finkelstein *et al.* (2012), but extended to higher redshift.

4.3.5 Correlation of β with SFR

We now investigate if there exists any correlation between β and SFR by plotting β as a function of SFR. To do this, we use the dust corrected star formation rates estimated in Section 2.3.6.2, correct them for magnification using the magnification factor estimated in Section 2.3.7, and compute the median values of β of our sample in bins of $-2.0 < \log \mathrm{SFR} < -1.5$, $-1.5 < \log \mathrm{SFR} < -1.0$, $-1.0 < \log \mathrm{SFR} < 0.0$, $0.0 < \log \mathrm{SFR} < 0.5$ and $0.5 < \log \mathrm{SFR} < 1.5$, shown by black circles in Fig. 4.6. Similarly, in Table 4.3, we list the median values in the mentioned SFR bins.

Inspecting Fig. 4.6, it is clear the there is a strong correlation between β and SFR, in that galaxies with low SFRs exhibit bluer slopes. To quantify this, we fit a first-order polynomial through the median data points at each redshift to estimate the slope and its associated uncertainty. The best-fit line at each redshift is shown in Fig. 4.6 and the values of the slope along with its uncertainty are listed in Table 4.3.

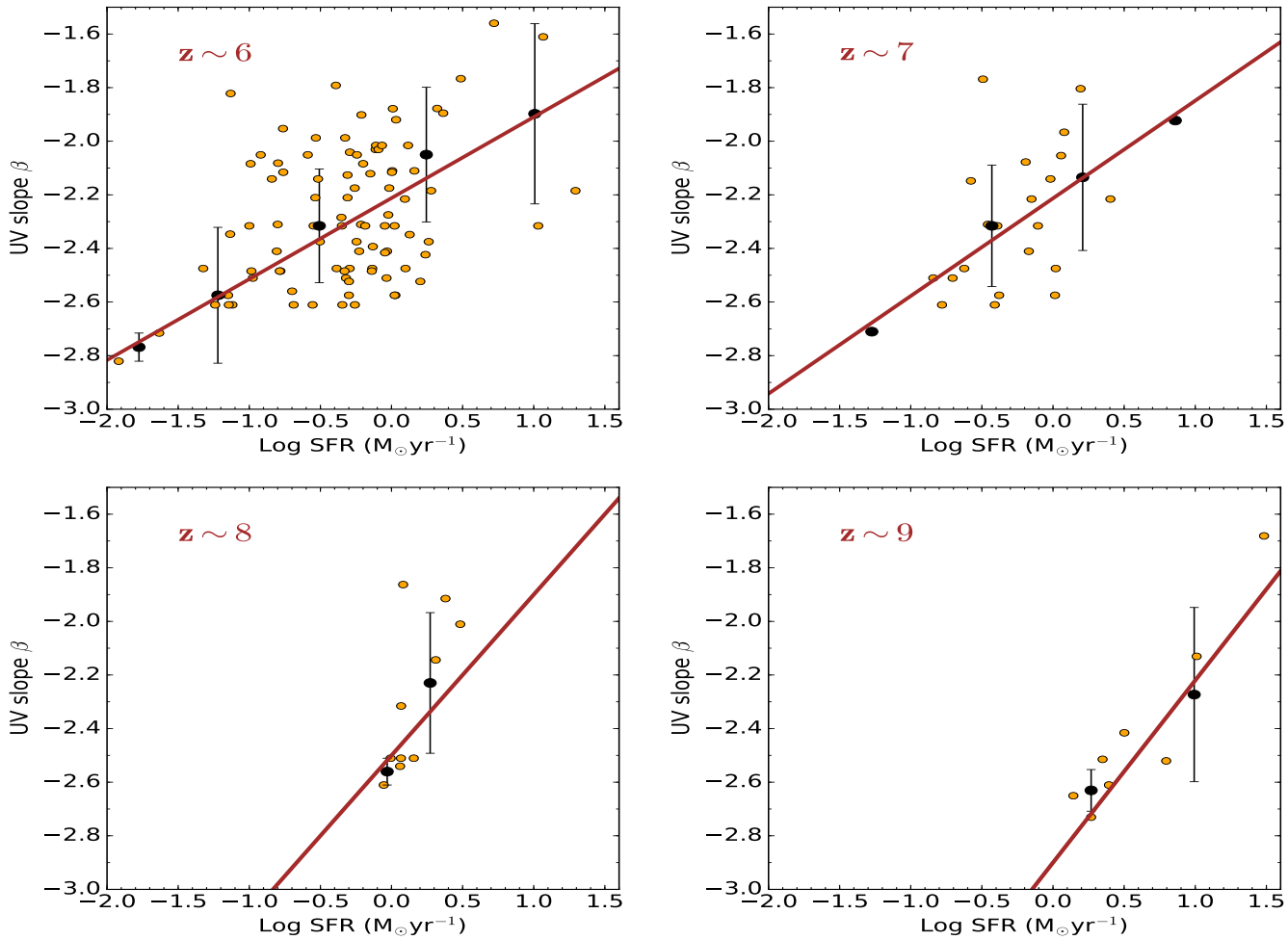


Figure 4.6: Estimated UV slope β vs SFR at $z = 6 - 9$. The filled yellow circles show the results for individual galaxies, whereas the black circles show the median value of β in each SFR bin of $1 M_{\odot} yr^{-1}$. The solid red lines show a linear fit through the median β points. There is a strong correlation between β and SFR, in that galaxies with low SFRs exhibit bluer slopes.

Table 4.3: Median values of the UV spectral slope β in different SFR bins.

z	Median β $-2.0 < \log \mathrm{SFR} < -1.5$	Median β $-1.5 < \log \mathrm{SFR} < -1.0$	Median β $-1.0 < \log \mathrm{SFR} < 0.0$	Median β $0.0 < \log \mathrm{SFR} < 0.5$	Median β $0.5 < \log \mathrm{SFR} < 1.5$	β - SFR slope
6	-2.78 ± 0.05	-2.56 ± 0.25	-2.30 ± 0.20	-2.05 ± 0.25	-1.89 ± 0.36	0.29 ± 0.14
7	..	-2.71 ± 0.03	-2.38 ± 0.23	-2.12 ± 0.27	-1.93 ± 0.04	0.37 ± 0.21
8	..	..	-2.57 ± 0.04	-2.24 ± 0.26	..	0.59 ± 0.35
9	..	..	..	-2.62 ± 0.08	-2.27 ± 0.32	0.67 ± 0.40

To investigate this further, we also plot β as a function of redshift, by spliting our sample into the same SFR bins as above bins; $-2.0 < \log \mathrm{SFR} < -1.5$, $-1.5 < \log \mathrm{SFR} < -1.0$, $-1.0 < \log \mathrm{SFR} < 0.0$, $0.0 < \log \mathrm{SFR} < 0.5$ and $0.5 < \log \mathrm{SFR} < 1.5$, as shown in Fig. 4.7. Inspecting the plot, it appears that galaxies with low SFRs are bluer and they tend to get bluer ($\sim 2\sigma$ correlation) with increasing redshift, which probably is just a result of mass, suggesting that low mass galaxies have low SFRs.

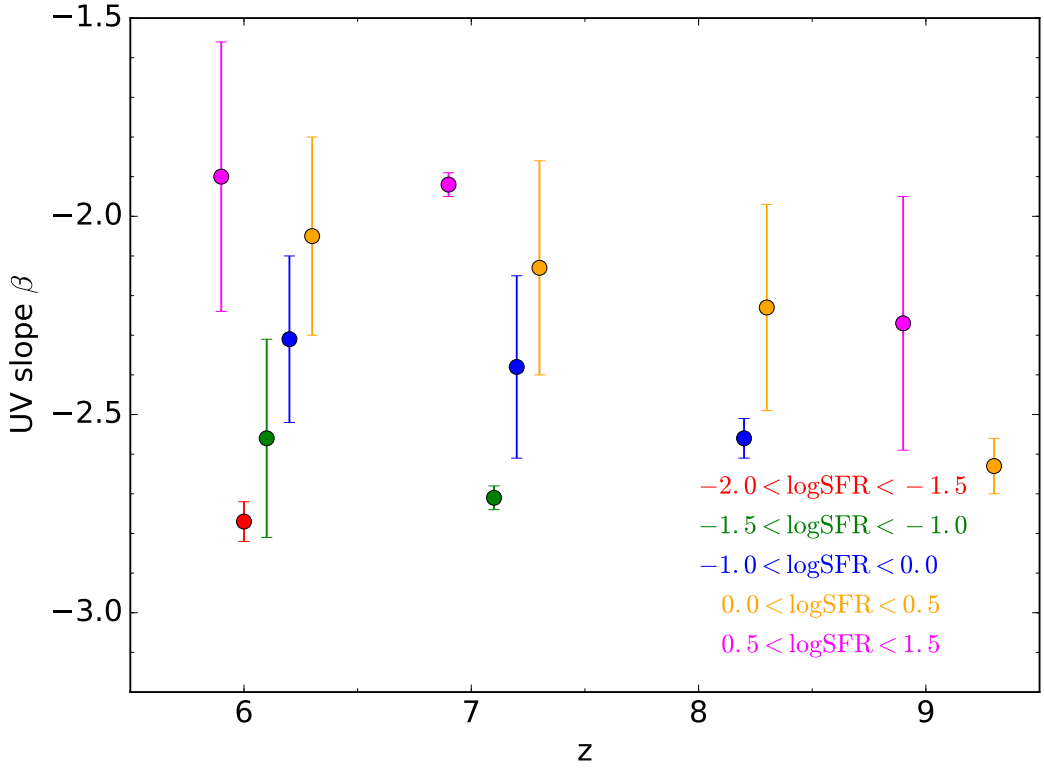


Figure 4.7: Evolution of median value of UV spectral slope β in different SFR bins with redshift. The red circle shows the median β in SFR bin $-2.0 < \log \mathrm{SFR} < -1.5$, green circles show the median β in SFR bin $-1.5 < \log \mathrm{SFR} < -1.0$, blue circles show the median β in SFR bin $-1.0 < \log \mathrm{SFR} < 0.0$, yellow circles show the median β in SFR bin $0.0 < \log \mathrm{SFR} < 0.5$ and finally the magenta circle shows the median β in SFR bin $0.5 < \log \mathrm{SFR} < 1.5$. It appears that galaxies with low SFRs are bluer and they tend to get bluer with increasing redshift.

4.3.6 Physical interpretation of β

As the UV continuum is produced by young and massive but short-lived O and B stars, the dependence of the UV continuum of stars to their surface temperatures, masses and metallicities in turn signifies the dependence of the continuum of a composite stellar population to the distribution of the masses (determined by the

IMF and SFH) and metallicities. The nebular emission also has an impact on the UV continuum in that a very blue slope suggests that the starlight is not significantly contaminated by redder nebular continuum (Dunlop *et al.* 2012; Robertson *et al.* 2010). Finally, the UV continuum is also affected by the distribution of dust with respect to the galaxies.

For example, since the UV continuum is dependent on its initial mass, with massive stars producing bluer slopes than the cooler stars, the IMF of a stellar population can likely affect the slope of a composite stellar population. Thus, an IMF with a larger number of massive stars (top-heavy IMF) will result in a bluer UV continuum slope.

The mass dependency of the lifetime of main-sequence stars means that the UV continuum slope is also affected by the star formation history. For example, with extended periods of star-formation, the massive stars will evolve off the main sequence resulting in a redder slope, while a spontaneous burst of shorter duration will produce a bluer slope.

Similarly, an increase in metallicity in the stellar cores will result in an increase in the opacity and hence lower effective temperatures. Due to this, a star with higher metallicity will not be able to sustain a higher core temperature thus causing inefficient transportation of energy from the stellar core to the surface, resulting in a redder slope and vice-versa.

Finally, since the reddening (caused by extinction due to dust grains) of an object is inversely proportional to the wavelength of optical light, the UV continuum is most affected due to dust. The shape of the dust attenuation curve, on the other hand, is sensitive to the source-dust geometry, grain size distribution etc. Due to these factors, estimating dust attenuation in external galaxies is much more complicated. The "Calzetti attenuation law" (Calzetti, Kinney & Storchi-Bergmann, 1994) is extensively used in the study of high-redshift galaxies, but since the dust attenuation law is derived from a sample of 39 nearby starburst galaxies, to what extent it is applicable to other systems at high redshift is debatable. Nevertheless, the law is still used as a first approximation as the properties of dust in starburst galaxies at high redshift are poorly constrained.

All these factors, the IMF, SFH, metallicity and dust, affect the UV slope β of stellar populations. Establishing the effects of these factors is challenging, particularly at high redshift. With the increase spectral coverage beyond 1.6μm, JWST will provide better constraints on the UV slope β for objects at $z > 8$.

4.4 Summary

In this chapter we have investigated the evolution of the UV spectral slope β for the sample of our high redshift galaxies at $z = 6-9$ in the MACSJ0416 cluster and its parallel field. With this study, we attempted to offer the first insight into the rest-frame UV colours of galaxies in a reasonably wide range of $-22 < \mathrm{M_{UV}} < -13$ with the HFF dataset.

We utilize the galaxy samples at $z = 6-9$ from Chapter 2 and measure the value of UV spectral slope β by fitting a power law to the best-fit model spectrum in the windows defined by (Calzetti, Kinney & Storchi-Bergmann, 1994). We also show with the help of simulations that this method is generally quite effective at recovering the correct values of β with small scatter and that the scatter increases at higher redshifts and at faint magnitudes.

As at fainter magnitudes and higher redshifts the uncertainty on the value of β for individual galaxy is large, we measure the median value of β in each redshift bin, as well as in separate bins split by UV luminosity, stellar mass and star formation rates. Our key conclusions are as follows:

1. We find no correlation between β and rest-frame UV magnitude M_{1500} at all redshifts probed in this work. However, some evidence for a weak evolution of the median β values (from $\beta = -2.24 \pm 0.18$ at $z \sim 6$ to $\beta = -2.52 \pm 0.34$ at $z \sim 9$) for galaxies at all luminosities from $z = 6-9$ is observed, presumably due to increased dust extinction.

2. At $z = 7$, the bluest value of our sample is $\beta = -2.31 \pm 0.31$, which is redder than previously reported values at this redshift in the literature. Similarly, with the help of our SED fitting method, we determine the UV slopes for the first time at $z \sim 9$ and find that our bluest data point has a value of $\beta = -2.63 \pm 0.21$, implying no evidence as yet for extreme stellar populations at $z > 6$.

3. Examining the β to stellar mass relation results in a strong correlation between β with stellar mass, in that lower mass galaxies exhibit bluer UV slopes. It also appears that low mass galaxies at $\log M/M_{\odot} < 9$ become bluer with increasing redshift, whereas the massive galaxies at $\log M/M_{\odot} > 9$ appear to exhibit a nearly constant β at each redshift. This is likely because dust can build up fairly rapidly in massive galaxies, whereas low mass galaxies lose dust due to feedback.

4. We also investigate the correlation between β and SFR and find that there is a strong correlation between β and SFR, in that galaxies with low SFRs exhibit bluer slopes, and they also appear to get bluer with increasing redshift, which presumably is just a result of mass, suggesting that low mass galaxies have low SFRs.

Chapter 5

Conclusions and Future Work

This thesis takes advantage of the power of gravitational lensing of massive clusters in combination with *HST*, VLT and *Spitzer* imaging of the MACSJ0416 cluster and its parallel field to probe the epoch of reionization with the Hubble Frontier Fields to address the question of when and how did the first galaxies form and evolve. Specifically, in Chapter 2, I described the methods used for the construction of our high-redshift sample at $z = 6 - 9$ and the estimation of their stellar masses, rest-frame UV magnitudes as well as star formation rates. In Chapter 3, I presented the results on the UV LF, GSMF, mass-to-light ratio, stellar mass density, UV luminosity density and specific star formation rates for this sample. Finally, in Chapter 4, the investigation of the evolution of the galaxy rest-frame UV colours of our high-z sample at $z = 6 - 9$ was presented.

In the following chapter I will summarize the conclusions of the work presented in this thesis, ending with a discussion on the future work that can build upon these results.

5.1 Exploring high redshift galaxies

Gravitational lensing of massive clusters enable the detection of galaxies fainter than the usual sensitivity limit for blank fields by providing a magnified boost to the light from the background galaxies. However, detection of these faint sources is made difficult by the presence of bright foreground cluster galaxies in the cluster. Particularly, the critical line - a line of theoretically infinite magnification where the most magnified sources are found - lies close to the center of the cluster and thus tends to be highly affected. Due to this, initial studies with the Hubble Frontier Fields did not find the expected population of intrinsically extremely faint galaxies instantly. This motivated us to explore new ways of approaching this problem, to

see if these challenges could be overcome, in order to fully exploit the potential of the Hubble Frontier Fields program.

In Chapter 2, I described the technique we developed to model and subtract the massive foreground galaxies that lie close to the critical line from the MACSJ0416 cluster, allowing for a deeper and cleaner detection of the faintest systems at $z \geq 6$. This method opened up the highly magnified region close to the critical line and enhanced the detection of faint sources in the cluster field by ~ 8 per cent. This subtraction procedure, in combination with the power of gravitational lensing, made it possible to probe magnitudes as faint as $M_{\rm UV} = -13.5$ and masses as low as $10^{6.8} M_{\odot}$.

5.2 Evolution of the GSMF and UV LF

In Chapter 3, I presented the investigation of the evolution of the GSMF and UV LF at $z = 6 - 9$ along with star formation rates in the Hubble Frontier Fields. Our new measurements of the GSMF show an apparent steepening of the low mass end slope α with increasing redshift, steeper than previously observed mass functions at slightly lower redshifts, and we find no evidence of a turnover within the mass range probed. This is the deepest and most distant mass function measured to date and probes down to a level of $\mathrm{M}_* = 10^{6.8} M_{\odot}$. There is also a decrease in normalization Φ^* with increasing redshift, but no evolution in the characteristic mass M^* is observed.

Our measurements of the integrated stellar mass density reveals that there is a surprisingly high amount of stellar mass density for galaxies in the early Universe up to $z \sim 9$. This suggests that galaxies of masses around 10^8 $\mathrm{M}_{\odot}$ have already formed a significant density by this time.

For the high redshift sample studied in this work, the observed mass-to-light ratios are compatible with a constant mass-to-light ratio at all redshifts, suggesting no strong evolution of mass-to-light ratio with luminosity. We notice that normalization, on the other hand, decreases with increasing redshift.

We also examine the star formation rates of our high-z sample in this work and find that in a fixed stellar mass bin of $\log_{10}(M/M_{\odot}) = 9.7 \pm 0.3$, the average specific star-formation rate (sSFR) increases steadily with redshift. This is in good agreement with previous results and also theoretical predictions that imply that the increased accretion of neutral gas upon haloes results in higher sSFR in the early Universe.

In this thesis, we also investigate the evolution of the UV LF at $z = 6 - 9$.

We find that the faint-end slope of our UV LFs also show an apparent steepening with increasing redshift, with no evidence of a turnover. The normalization Φ^* of the UV LF decreases with increasing redshift and a weak evolution in $M^*_{\rm UV}$ is also observed, with it decreasing with redshift. This suggests that the evolution of the UV luminosity function with redshift appears to be more consistent with an evolution of density.

Finally, our new measurements of the UV LF allow us to estimate the UV luminosity density (and hence cosmic star formation rate density) by integrating the UV LFs down to an absolute magnitude of $M_{\rm UV} = -13.5$. These results are quite high and also show an increase from $z = 6 - 9$ and thus support the idea that faint galaxies in the early Universe could have been responsible for reionization.

5.3 Evolution of the rest-frame UV colours

In Chapter 4, the evolution of the galaxy rest-frame UV colours is investigated for the sample of our high redshift galaxies at $z = 6 - 9$ in the MACSJ0416 cluster and its parallel field. The Hubble Frontier Fields has reinforced the number counts of the intrinsically faintest galaxy populations at this epoch. By utilizing this dataset, we therefore attempted to offer the first insight into the rest-frame UV colours of galaxies in a reasonably wide range of $-22 < {\rm M_{UV}} < -13$. In this work, we find no correlation between β and UV luminosity at all redshifts. However, a possible evidence for a weak evolution of the median β values for galaxies at all luminosities from $z = 6 - 9$ is observed, likely due to increased dust extinction.

The value of β ($\beta \sim -3$) at $z = 7$ has been a topic of debate in the literature, suggesting that exotic populations might be necessary to produce such blue values of β. At $z = 7$, the bluest measured value of our sample is $\beta = -2.31 \pm 0.31$, which is redder than previously reported values. Similarly, with our dataset, we have been able to determine the UV slopes for the first time at $z \sim 9$ and find that our bluest data point has a value of $\beta = -2.63 \pm 0.21$ at this redshift, implying no evidence as yet for extreme stellar populations at $z > 6$.

We also compare β to stellar mass relation and find a strong correlation between β and stellar mass, in that lower mass galaxies exhibit bluer UV slopes. We also find that low mass galaxies at $\log M/M_\odot < 9$ appear to become bluer with increasing redshift. The massive galaxies at $\log M/M_\odot > 9$, on the other hand, appear to exhibit a nearly constant β at each redshift. This is presumably because dust can build up fairly rapidly in massive galaxies, whilst low mass galaxies lose dust due to feedback.

Finally, we investigate the relation between β and SFR and find that there is a strong correlation between β and SFR, in that galaxies with low SFRs exhibit bluer slopes, and they also appear to get bluer with increasing redshift, which is likely just a result of mass, suggesting that low mass galaxies have low SFRs.

5.4 Future work

This thesis exhibits the power of gravitational lensing to probe the faintest and earliest galaxies in the early Universe. While the results from this study are very intriguing, the uncertainties are still large due to a small sample size. This necessitates the need for the analysis of the complete Hubble Frontier Fields dataset, comprising six clusters and six associated parallel fields, to robustly constrain the high and low mass end of the GSMF as well as the faint and bright end of the UV LF in the future. This is, however, a significant undertaking as subtracting the foreground galaxies takes up the bulk of the effort when studying nearby massive lensing clusters. On the other hand, to probe even higher redshifts requires the advantage of JWST.

JWST is a state-of-the-art observatory that will answer long standing fundamental questions about galaxy formation and evolution, particularly at the earliest epochs of the first generation of assembly, by providing an unprecedented quality and quantity of spectroscopic and photometric data. The Near-Infrared Camera (NIRCam) and the Mid-Infrared Instrument (MIRI) will provide photometric observations covering the observer-frame range from 0.6 to 29 μm. The Near-Infrared Spectrograph (NIRSpec), MIRI, and the Near-Infrared Imager and Slitless Spectrograph (NIRISS) will provide spectroscopic observations with a sensitivity and a resolution that have never been achieved, especially for galaxies at $z > 2$. As such, observations with this telescope will reveal how the first galaxies formed, what sources reionized the Universe, and how the diverse galaxy population we can study at $z \sim 3$ was established at higher redshifts.

With *HST*, galaxies can be detected up to $z \sim 10$ (i.e. seen ~ 500 Myr after the Big Bang). However, detections at the highest redshifts are uncertain as these sources can only be seen in the one reddest filter available, F160W. Due to the coverage at longer wavelengths, detections at $z \sim 10$ will be more robust with NIRCam, and detections out to $z \sim 15$ will be theoretically possible should sufficiently bright sources exist. Furthermore, JWST will, for the first time, provide rest-frame optical imaging of galaxies during the epoch of reionization with similar spatial resolution to *HST*. This means we can move beyond the UV and explore the build-up

of stellar mass in the early Universe.

The advent of JWST will thus allow us to extend the work in this thesis all the way back to redshift of $z = 12$, if not even earlier as follows:

- **UV LF at** $6 < z < 12$: In this thesis, with the subtraction method that we have developed, in combination with lensing, we have been able to characterize the UV LF to magnitudes as faint as $M_{UV} = -13.5$. With JWST, plus the flux magnification from gravitational lensing, we can push these limits even further towards the faintest magnitudes, measure the UV luminosities of galaxies up to $z = 12$, and consider their evolution in several ways. This will allow us to put better constraints on the faint end slope and understand the galaxies available to power reionization.

- **GSMF at** $6 < z < 12$: In this thesis, we have shown for the first time that the GSMF continues to remain unbroken to masses as low as $10^{6.8}\mathrm{M}_{\odot}$, showing that the low mass end of the stellar mass function becomes increasingly steep at higher redshifts. As the stellar mass function continues to be occupied by increasingly lower mass galaxies, it is worth examining if at some point the mass function turns over. By combining the power of JWST with gravitational lensing, this study can be extended beyond $z = 9$, down to very low masses. The mass function will reveal the integrated star formation and merger history of the first galaxies and dark matter halos. By directly comparing the GSMF and UV LF will thus provide another measure of how assembly has occurred in these early galaxies. The mass function shape and turn over at low-masses, if it exists, is also a powerful method of probing the temperature of the dark matter particle and can rule out specific warm dark matter scenarios (e.g., Menci *et al.* 2017; Villanueva-Domingo, Gnedin & Mena 2018).

- **UV luminosity density and stellar mass density**: As with the UV LF, the studies of UV luminosity density (ρ_{UV}) have conflicting results. Studies like Bouwens *et al.* (2015a), Oesch *et al.* (2014) find an accelerated decline in ρ_{UV} at $z \geq 8$, while results from McLeod, McLure & Dunlop (2016), Ishigaki *et al.* (2018) report a smooth decline towards high redshifts. With our new measurements of the UV LF, we are able to integrate the best-fit Schechter parameters for our UV LFs down to a faint-end magnitude limit of $M_{UV} = -13.5$, and our results support a smooth decline of ρ_{UV} from $z = 6 - 9$. Similarly, integrating our GSMF, we find that there is a surprisingly high amount of stellar mass density for galaxies in the early Universe up to $z \sim 9$. This is an indication that galaxies of masses around 10^8 $\mathrm{M}_{\odot}$ have already

formed a significant density by this time. This further indicates that the star formation and assembly history for galaxies is significant in the epochs $z > 9$, which we cannot probe in detail until the launch of JWST. With JWST this study can be extended beyond $z = 9$, out to the epoch of the first galaxies.

- **UV spectral slope β for low luminous galaxies**: Observations so far show that the UV spectral slope β is consistent with a very low, but still non-zero metallicity, for low luminous galaxies at $z = 6 - 8$, yet the results overall are not entirely consistent (e.g., Dunlop *et al.* 2012; Bouwens *et al.* 2014b; Duncan *et al.* 2014). In this thesis, with the HFF dataset, we have been able to cover a reasonably wide range of $-22 < \mathrm{M_{UV}} < -13$, finding that our bluest data point has a value of $\beta = -2.63 \pm 0.21$. This suggests no evidence as yet for extreme stellar populations at $z > 6$. With JWST, this study can be extended towards the faintest magnitudes and to higher, completely unexplored redshifts. If we detect blue slopes of $\beta \sim -3$ from these galaxies, we will discover the first evidence for very low-metallicity star-formation in the early Universe.

Appendix A

Catalogs

Table A.1: Catalog of the $z \sim 8$ sample. Column (1) lists the source IDs, column (2) and (3) lists their coordinates, column (4) gives the photometric redshift, column (5) lists the median magnification, column (6) is the absolute magnitude at 1500 angstrom and column (7) is the logarithm of the stellar mass. Both absolute magnitude and stellar mass values are corrected for magnification.

ID	RA	Dec.	$z_{\rm phot}$	Magnification	M_{1500}	log M_* ($M_\odot$)
MACS0416 cluster						
2095	64.0342	−24.0699	$8.43^{+0.27}_{-0.66}$	3.12	$-18.78^{+0.45}_{-0.32}$	$8.21^{+0.34}_{-0.24}$
257	64.0336	−24.0900	$7.71^{+0.16}_{-0.71}$	2.21	$-18.60^{+0.28}_{-0.36}$	$8.29^{+0.45}_{-0.29}$
2365	64.0476	−24.0667	$8.06^{+0.18}_{-1.05}$	11.92	$-15.55^{+0.61}_{-0.86}$	$7.84^{+0.79}_{-1.7}$
2613	64.0603	−24.0649	$8.06^{+0.22}_{-0.36}$	1.61	$-18.47^{+0.42}_{-0.31}$	$8.36^{+0.44}_{-0.35}$
1288	64.0327	−24.0790	$8.15^{+0.49}_{-0.36}$	9.67	$-17.26^{+0.29}_{-0.26}$	$7.82^{+0.28}_{-0.25}$
Parallel field						
154	64.1319	−24.1311	$7.71^{+0.10}_{-1.09}$	-	$-18.76^{+0.22}_{-0.56}$	$8.27^{+0.32}_{-0.23}$
2674	64.1268	−24.1000	$8.25^{+0.12}_{-0.62}$	-	$-19.00^{+0.27}_{-0.35}$	$8.51^{+0.49}_{-0.31}$
495	64.1213	−24.1258	$7.88^{+0.10}_{-0.59}$	-	$-19.82^{+0.28}_{-0.32}$	$8.62^{+0.27}_{-0.21}$
1237	64.1196	−24.1169	$7.71^{+0.27}_{-0.66}$	-	$-18.78^{+0.27}_{-0.66}$	$8.64^{+0.27}_{-0.66}$
1084	64.1545	-24.1188	$8.25^{+0.27}_{-0.66}$	-	$-20.13^{+0.27}_{-0.66}$	$8.91^{+0.27}_{-0.66}$

Table A.2: Catalog of the $z \sim 9$ sample. Column (1) lists the source IDs, column (2) and (3) lists their coordinates, column (4) gives the photometric redshift, column (5) lists the median magnification, column (6) is the absolute magnitude at 1500 angstrom and column (7) is the logarithm of the stellar mass. Both absolute magnitude and stellar mass values are corrected for magnification.

ID	RA	Dec.	$z_{\rm phot}$	Magnification	M_{1500}	log M_* ($M_\odot$)
MACS0416 cluster						
126	64.0391	−24.0931	$8.62^{+0.22}_{-0.18}$	1.72	$-20.55^{+0.47}_{-0.36}$	$8.84^{+0.20}_{-0.18}$
1040	64.0479	−24.0816	$8.72^{+0.12}_{-0.23}$	1.61	$-20.12^{+0.27}_{-0.16}$	$8.71^{+0.28}_{-0.21}$
1065	64.0480	−24.0814	$8.72^{+0.52}_{-0.22}$	1.56	$-20.25^{+0.18}_{-0.22}$	$9.44^{+0.42}_{-0.37}$
393	64.0375	−24.0881	$8.62^{+0.14}_{-0.55}$	1.58	$-18.78^{+0.27}_{-0.26}$	$8.28^{+0.42}_{-0.29}$
Parallel field						
1524	64.1498	−24.1133	$9.42^{+0.23}_{-0.76}$	-	$-19.59^{+0.23}_{-0.21}$	$8.63^{+0.51}_{-0.39}$
1957	64.1517	−24.1084	$9.01^{+0.52}_{-0.35}$	-	$-18.96^{+0.20}_{-0.18}$	$8.93^{+0.60}_{-0.48}$
2660	64.1267	−24.1003	$8.53^{+0.17}_{-0.62}$	-	$-18.97^{+0.27}_{-0.32}$	$8.50^{+0.46}_{-0.31}$
1646	64.1479	−24.1117	$8.72^{+0.09}_{-0.94}$	-	$-18.84^{+0.22}_{-0.18}$	$8.31^{+0.51}_{-0.43}$

Bibliography

Arnouts S., Ilbert O., 2011. *LePHARE: Photometric Analysis for Redshift Estimate*, Astrophysics Source Code Library.

Atek H., Richard J., Kneib J.-P., Clement B., Egami E., Ebeling H., Jauzac M., Jullo E., Laporte N., Limousin M., Natarajan P., 2014. ApJ, **786**, 60.

Atek H., Richard J., Kneib J.-P., Schaerer D., 2018. *ArXiv e-prints*.

Avni Y., Bahcall J. N., 1980. ApJ, **235**, 694.

Balestra I., Mercurio A., Sartoris B., Girardi M., Grillo C., Nonino M., Rosati P., Biviano A., Ettori S., Forman W., Jones C., Koekemoer A., Medezinski E., Merten J., Ogrean G. A., Tozzi P., Umetsu K., Vanzella E., van Weeren R. J., Zitrin A., Annunziatella M., Caminha G. B., Broadhurst T., Coe D., Donahue M., Fritz A., Frye B., Kelson D., Lombardi M., Maier C., Meneghetti M., Monna A., Postman M., Scodeggio M., Seitz S., Ziegler B., 2016. ApJS, **224**, 33.

Barden M., Häußler B., Peng C. Y., McIntosh D. H., Guo Y., 2012. MNRAS, **422**, 449.

Becker R. H., Fan X., White R. L., Strauss M. A., Narayanan V. K., Lupton R. H., Gunn J. E., Annis J., Bahcall N. A., Brinkmann J., Connolly A. J., Csabai I., Czarapata P. C., Doi M., Heckman T. M., Hennessy G. S., Ivezić Ž., Knapp G. R., Lamb D. Q., McKay T. A., Munn J. A., Nash T., Nichol R., Pier J. R., Richards G. T., Schneider D. P., Stoughton C., Szalay A. S., Thakar A. R., York D. G., 2001. AJ, **122**, 2850.

Beckwith S. V. W., Stiavelli M., Koekemoer A. M., Caldwell J. A. R., Ferguson H. C., Hook R., Lucas R. A., Bergeron L. E., Corbin M., Jogee S., Panagia N., Robberto M., Royle P., Somerville R. S., Sosey M., 2006. AJ, **132**, 1729.

Behroozi P., Wechsler R., Hearin A., Conroy C., 2018. *ArXiv e-prints*.

Benitez N., Ford H., Bouwens R., Menanteau F., Blakeslee J., Gronwall C., Illingworth G., Meurer G., Broadhurst T. J., Clampin M., Franx M., Hartig G. F., Magee D., Sirianni M., Ardila D. R., Bartko F., Brown R. A., Burrows C. J., Cheng E. S., Cross N. J. G., Feldman P. D., Golimowski D. A., Infante L., Kimble R. A., Krist J. E., Lesser M. P., Levay Z., Martel A. R., Miley G. K., Postman M., Rosati P., Sparks W. B., Tran H. D., Tsvetanov Z. I., White R. L., Zheng W., 2004. ApJS, **150**, 1.

Benitez N., 2000. ApJ, **536**, 571.

Bernyk M., Croton D. J., Tonini C., Hodkinson L., Hassan A. H., Garel T., Duffy A. R., Mutch S. J., Poole G. B., Hegarty S., 2016. ApJS, **223**, 9.

Bertin E., Arnouts S., 1996. A&AS, **117**, 393.

Bertin E., Mellier Y., Radovich M., Missonnier G., Didelon P., Morin B., 2002. *The TERAPIX Pipeline*, In: *Astronomical Data Analysis Software and Systems XI*, 228, eds Bohlender D. A., Durand D., Handley T. H.

Bolzonella M., Miralles J.-M., Pelló R., 2000. A&A, **363**, 476.

Bouwens R. J., Illingworth G. D., Rosati P., Lidman C., Broadhurst T., Franx M., Ford H. C., Magee D., Benítez N., Blakeslee J. P., Meurer G. R., Clampin M., Hartig G. F., Ardila D. R., Bartko F., Brown R. A., Burrows C. J., Cheng E. S., Cross N. J. G., Feldman P. D., Golimowski D. A., Gronwall C., Infante L., Kimble R. A., Krist J. E., Lesser M. P., Martel A. R., Menanteau F., Miley G. K., Postman M., Sirianni M., Sparks W. B., Tran H. D., Tsvetanov Z. I., White R. L., Zheng W., 2003. ApJ, **595**, 589.

Bouwens R. J., Illingworth G. D., Franx M., Ford H., 2007. ApJ, **670**, 928.

Bouwens R. J., Illingworth G. D., Bradley L. D., Ford H., Franx M., Zheng W., Broadhurst T., Coe D., Jee M. J., 2009. ApJ, **690**, 1764.

Bouwens R. J., Illingworth G. D., Oesch P. A., Trenti M., Stiavelli M., Carollo C. M., Franx M., van Dokkum P. G., Labbé I., Magee D., 2010. ApJ, **708**, L69.

Bouwens R. J., Illingworth G. D., Labbe I., Oesch P. A., Trenti M., Carollo C. M., van Dokkum P. G., Franx M., Stiavelli M., González V., Magee D., Bradley L., 2011. Nature, **469**, 504.

Bouwens R. J., Illingworth G. D., Oesch P. A., Franx M., Labbé I., Trenti M., van Dokkum P., Carollo C. M., González V., Smit R., Magee D., 2012. ApJ, **754**, 83.

Bouwens R. J., Bradley L., Zitrin A., Coe D., Franx M., Zheng W., Smit R., Host O., Postman M., Moustakas L., Labbé I., Carrasco M., Molino A., Donahue M., Kelson D. D., Meneghetti M., Benítez N., Lemze D., Umetsu K., Broadhurst T., Moustakas J., Rosati P., Jouvel S., Bartelmann M., Ford H., Graves G., Grillo C., Infante L., Jimenez-Teja Y., Lahav O., Maoz D., Medezinski E., Melchior P., Merten J., Nonino M., Ogaz S., Seitz S., 2014a. ApJ, **795**, 126.

Bouwens R. J., Illingworth G. D., Oesch P. A., Labbé I., van Dokkum P. G., Trenti M., Franx M., Smit R., Gonzalez V., Magee D., 2014b. ApJ, **793**, 115.

Bouwens R. J., Illingworth G. D., Oesch P. A., Caruana J., Holwerda B., Smit R., Wilkins S., 2015a. ApJ, **811**, 140.

Bouwens R. J., Illingworth G. D., Oesch P. A., Trenti M., Labbé I., Bradley L., Carollo M., van Dokkum P. G., Gonzalez V., Holwerda B., Franx M., Spitler L., Smit R., Magee D., 2015b. ApJ, **803**, 34.

Bouwens R. J., Oesch P. A., Labbé I., Illingworth G. D., Fazio G. G., Coe D., Holwerda B., Smit R., Stefanon M., van Dokkum P. G., Trenti M., Ashby M. L. N., Huang J.-S., Spitler L., Straatman C., Bradley L., Magee D., 2016. ApJ, **830**, 67.

Bouwens R. J., Illingworth G. D., Oesch P. A., Atek H., Lam D., Stefanon M., 2017a. ApJ, **843**, 41.

Bouwens R. J., Oesch P. A., Illingworth G. D., Ellis R. S., Stefanon M., 2017b. ApJ, **843**, 129.

Bower R. G., Benson A. J., Malbon R., Helly J. C., Frenk C. S., Baugh C. M., Cole S., Lacey C. G., 2006. MNRAS, **370**, 645.

Bowler R. A. A., Dunlop J. S., McLure R. J., McCracken H. J., Milvang-Jensen B., Furusawa H., Taniguchi Y., Le Fèvre O., Fynbo J. P. U., Jarvis M. J., Häußler B., 2015. MNRAS, **452**, 1817.

Bradač M., Treu T., Applegate D., Gonzalez A. H., Clowe D., Forman W., Jones C., Marshall P., Schneider P., Zaritsky D., 2009. ApJ, **706**, 1201.

Bradley L. D., Zitrin A., Coe D., Bouwens R., Postman M., Balestra I., Grillo C., Monna A., Rosati P., Seitz S., Host O., Lemze D., Moustakas J., Moustakas L. A., Shu X., Zheng W., Broadhurst T., Carrasco M., Jouvel S., Koekemoer A., Medezinski E., Meneghetti M., Nonino M., Smit R., Umetsu K., Bartelmann M.,

Benítez N., Donahue M., Ford H., Infante L., Jimenez-Teja Y., Kelson D., Lahav O., Maoz D., Melchior P., Merten J., Molino A., 2014. ApJ, **792**, 76.

Brammer G. B., Marchesini D., Labbé I., Spitler L., Lange-Vagle D., Barker E. A., Tanaka M., Fontana A., Galametz A., Ferré-Mateu A., Kodama T., Lundgren B., Martis N., Muzzin A., Stefanon M., Toft S., van der Wel A., Vulcani B., Whitaker K. E., 2016. ApJS, **226**, 6.

Brammer G. B., van Dokkum P. G., Coppi P., 2008. ApJ, **686**, 1503.

Bruzual G., Charlot S., 2003. MNRAS, **344**, 1000.

Bunker A. J., Stanway E. R., Ellis R. S., McMahon R. G., McCarthy P. J., 2003. MNRAS, **342**, L47.

Bunker A. J., Wilkins S., Ellis R. S., Stark D. P., Lorenzoni S., Chiu K., Lacy M., Jarvis M. J., Hickey S., 2010. MNRAS, **409**, 855.

Calzetti D., Armus L., Bohlin R. C., Kinney A. L., Koornneef J., Storchi-Bergmann T., 2000. ApJ, **533**, 682.

Calzetti D., Kinney A. L., Storchi-Bergmann T., 1994. ApJ, **429**, 582.

Caminha G. B., Grillo C., Rosati P., Balestra I., Mercurio A., Vanzella E., Biviano A., Caputi K. I., Delgado-Correal C., Karman W., Lombardi M., Meneghetti M., Sartoris B., Tozzi P., 2017. A&A, **600**, A90.

Casertano S., de Mello D., Dickinson M., Ferguson H. C., Fruchter A. S., Gonzalez-Lopezlira R. A., Heyer I., Hook R. N., Levay Z., Lucas R. A., Mack J., Makidon R. B., Mutchler M., Smith T. E., Stiavelli M., Wiggs M. S., Williams R. E., 2000. AJ, **120**, 2747.

Castellano M., Amorín R., Merlin E., Fontana A., McLure R. J., Mármol-Queraltó E., Mortlock A., Parsa S., Dunlop J. S., Elbaz D., Balestra I., Boucaud A., Bourne N., Boutsia K., Brammer G., Bruce V. A., Buitrago F., Capak P., Cappelluti N., Ciesla L., Comastri A., Cullen F., Derriere S., Faber S. M., Giallongo E., Grazian A., Grillo C., Mercurio A., Michałowski M. J., Nonino M., Paris D., Pentericci L., Pilo S., Rosati P., Santini P., Schreiber C., Shu X., Wang T., 2016. A&A, **590**, A31.

Ceverino D., Glover S. C. O., Klessen R. S., 2017. MNRAS, **470**, 2791.

Chabrier G., 2003. PASP, **115**, 763.

Choi J.-H., Nagamine K., 2010. MNRAS, **407**, 1464.

Choi J.-H., Nagamine K., 2012. MNRAS, **419**, 1280.

Coe D., Zitrin A., Carrasco M., Shu X., Zheng W., Postman M., Bradley L., Koekemoer A., Bouwens R., Broadhurst T., Monna A., Host O., Moustakas L. A., Ford H., Moustakas J., van der Wel A., Donahue M., Rodney S. A., Benítez N., Jouvel S., Seitz S., Kelson D. D., Rosati P., 2013. ApJ, **762**, 32.

Conselice C. J., Wilkinson A., Duncan K., Mortlock A., 2016. ApJ, **830**, 83.

Croton D. J., Springel V., White S. D. M., De Lucia G., Frenk C. S., Gao L., Jenkins A., Kauffmann G., Navarro J. F., Yoshida N., 2006. MNRAS, **365**, 11.

Daddi E., Cimatti A., Renzini A., Fontana A., Mignoli M., Pozzetti L., Tozzi P., Zamorani G., 2004. ApJ, **617**, 746.

Dahlen T., Mobasher B., Faber S. M., Ferguson H. C., Barro G., Finkelstein S. L., Finlator K., Fontana A., Gruetzbauch R., Johnson S., Pforr J., Salvato M., Wiklind T., Wuyts S., Acquaviva V., Dickinson M. E., Guo Y., Huang J., Huang K.-H., Newman J. A., Bell E. F., Conselice C. J., Galametz A., Gawiser E., Giavalisco M., Grogin N. A., Hathi N., Kocevski D., Koekemoer A. M., Koo D. C., Lee K.-S., McGrath E. J., Papovich C., Peth M., Ryan R., Somerville R., Weiner B., Wilson G., 2013. ApJ, **775**, 93.

Davé R., 2008. MNRAS, **385**, 147.

Dayal P., Ferrara A., Dunlop J. S., Pacucci F., 2014. MNRAS, **445**, 2545.

Dekel A., Zolotov A., Tweed D., Cacciato M., Ceverino D., Primack J. R., 2013. MNRAS, **435**, 999.

Dey A., Spinrad H., Stern D., Graham J. R., Chaffee F. H., 1998. ApJ, **498**, L93.

Duncan K., Conselice C. J., 2015. MNRAS, **451**, 2030.

Duncan K., Conselice C. J., Mortlock A., Hartley W. G., Guo Y., Ferguson H. C., Davé R., Lu Y., Ownsworth J., Ashby M. L. N., Dekel A., Dickinson M., Faber S., Giavalisco M., Grogin N., Kocevski D., Koekemoer A., Somerville R. S., White C. E., 2014. MNRAS, **444**, 2960.

Dunlop J. S., McLure R. J., Robertson B. E., Ellis R. S., Stark D. P., Cirasuolo M., de Ravel L., 2012. MNRAS, **420**, 901.

Dunlop J. S., Rogers A. B., McLure R. J., Ellis R. S., Robertson B. E., Koekemoer A., Dayal P., Curtis-Lake E., Wild V., Charlot S., Bowler R. A. A., Schenker M. A., Ouchi M., Ono Y., Cirasuolo M., Furlanetto S. R., Stark D. P., Targett T. A., Schneider E., 2013. MNRAS, **432**, 3520.

Eales S., 1993. ApJ, **404**, 51.

Ellis R. S., McLure R. J., Dunlop J. S., Robertson B. E., Ono Y., Schenker M. A., Koekemoer A., Bowler R. A. A., Ouchi M., Rogers A. B., Curtis-Lake E., Schneider E., Charlot S., Stark D. P., Furlanetto S. R., Cirasuolo M., 2013. ApJ, **763**, L7.

Erb D. K., Pettini M., Shapley A. E., Steidel C. C., Law D. R., Reddy N. A., 2010. ApJ, **719**, 1168.

Ferguson H. C., Dickinson M., Williams R., 2000. ARA&A, **38**, 667.

Ferguson H. C., Dickinson M., Giavalisco M., Kretchmer C., Ravindranath S., Idzi R., Taylor E., Conselice C. J., Fall S. M., Gardner J. P., Livio M., Madau P., Moustakas L. A., Papovich C. M., Somerville R. S., Spinrad H., Stern D., 2004. ApJ, **600**, L107.

Finkelstein S. L., Papovich C., Giavalisco M., Reddy N. A., Ferguson H. C., Koekemoer A. M., Dickinson M., 2010. ApJ, **719**, 1250.

Finkelstein S. L., Papovich C., Salmon B., Finlator K., Dickinson M., Ferguson H. C., Giavalisco M., Koekemoer A. M., Reddy N. A., Bassett R., Conselice C. J., Dunlop J. S., Faber S. M., Grogin N. A., Hathi N. P., Kocevski D. D., Lai K., Lee K.-S., McLure R. J., Mobasher B., Newman J. A., 2012. ApJ, **756**, 164.

Finkelstein S. L., Ryan, Jr. R. E., Papovich C., Dickinson M., Song M., Somerville R. S., Ferguson H. C., Salmon B., Giavalisco M., Koekemoer A. M., Ashby M. L. N., Behroozi P., Castellano M., Dunlop J. S., Faber S. M., Fazio G. G., Fontana A., Grogin N. A., Hathi N., Jaacks J., Kocevski D. D., Livermore R., McLure R. J., Merlin E., Mobasher B., Newman J. A., Rafelski M., Tilvi V., Willner S. P., 2015. ApJ, **810**, 71.

Finlator K., Oppenheimer B. D., Davé R., 2011. MNRAS, **410**, 1703.

Fioc M., Rocca-Volmerange B., 1997. A&A, **326**, 950.

Foreman-Mackey D., Hogg D. W., Lang D., Goodman J., 2013. PASP, **125**, 306.

Franceschini A., Silva L., Fasano G., Granato G. L., Bressan A., Arnouts S., Danese L., 1998. ApJ, **506**, 600.

Galametz A., Grazian A., Fontana A., Ferguson H. C., Ashby M. L. N., Barro G., Castellano M., Dahlen T., Donley J. L., Faber S. M., Grogin N., Guo Y., Huang K.-H., Kocevski D. D., Koekemoer A. M., Lee K.-S., McGrath E. J., Peth M., Willner S. P., Almaini O., Cooper M., Cooray A., Conselice C. J., Dickinson M., Dunlop J. S., Fazio G. G., Foucaud S., Gardner J. P., Giavalisco M., Hathi N. P., Hartley W. G., Koo D. C., Lai K., de Mello D. F., McLure R. J., Lucas R. A., Paris D., Pentericci L., Santini P., Simpson C., Sommariva V., Targett T., Weiner B. J., Wuyts S., the CANDELS Team, 2013. ApJS, **206**, 10.

Genel S., Vogelsberger M., Springel V., Sijacki D., Nelson D., Snyder G., Rodriguez-Gomez V., Torrey P., Hernquist L., 2014. MNRAS, **445**, 175.

Giavalisco M., Dickinson M., Ferguson H. C., Ravindranath S., Kretchmer C., Moustakas L. A., Madau P., Fall S. M., Gardner J. P., Livio M., Papovich C., Renzini A., Spinrad H., Stern D., Riess A., 2004. ApJ, **600**, L103.

Gnedin N. Y., 2016. ApJ, **825**, L17.

González V., Labbé I., Bouwens R. J., Illingworth G., Franx M., Kriek M., Brammer G. B., 2010. ApJ, **713**, 115.

González V., Labbé I., Bouwens R. J., Illingworth G., Franx M., Kriek M., 2011. ApJ, **735**, L34.

González V., Bouwens R. J., Labbé I., Illingworth G., Oesch P., Franx M., Magee D., 2012. ApJ, **755**, 148.

González V., Bouwens R., Illingworth G., Labbé I., Oesch P., Franx M., Magee D., 2014. ApJ, **781**, 34.

Goodman J., Weare J., 2010. *Communications in Applied Mathematics and Computational Science, Vol. 5, No. 1, p. 65-80, 2010*, **5**, 65.

Graham A. W., Driver S. P., 2005. , **22**, 118.

Grazian A., Fontana A., de Santis C., Nonino M., Salimbeni S., Giallongo E., Cristiani S., Gallozzi S., Vanzella E., 2006. A&A, **449**, 951.

Grazian A., Castellano M., Koekemoer A. M., Fontana A., Pentericci L., Testa V., Boutsia K., Giallongo E., Giavalisco M., Santini P., 2011. A&A, **532**, A33.

Grazian A., Castellano M., Fontana A., Pentericci L., Dunlop J. S., McLure R. J., Koekemoer A. M., Dickinson M. E., Faber S. M., Ferguson H. C., Galametz A., Giavalisco M., Grogin N. A., Hathi N. P., Kocevski D. D., Lai K., Newman J. A., Vanzella E., 2012. A&A, **547**, A51.

Grazian A., Fontana A., Santini P., Dunlop J. S., Ferguson H. C., Castellano M., Amorin R., Ashby M. L. N., Barro G., Behroozi P., Boutsia K., Caputi K. I., Chary R. R., Dekel A., Dickinson M. E., Faber S. M., Fazio G. G., Finkelstein S. L., Galametz A., Giallongo E., Giavalisco M., Grogin N. A., Guo Y., Kocevski D., Koekemoer A. M., Koo D. C., Lee K.-S., Lu Y., Merlin E., Mobasher B., Nonino M., Papovich C., Paris D., Pentericci L., Reddy N., Renzini A., Salmon B., Salvato M., Sommariva V., Song M., Vanzella E., 2015. A&A, **575**, A96.

Grillo C., Suyu S. H., Rosati P., Mercurio A., Balestra I., Munari E., Nonino M., Caminha G. B., Lombardi M., De Lucia G., Borgani S., Gobat R., Biviano A., Girardi M., Umetsu K., Coe D., Koekemoer A. M., Postman M., Zitrin A., Halkola A., Broadhurst T., Sartoris B., Presotto V., Annunziatella M., Maier C., Fritz A., Vanzella E., Frye B., 2015. ApJ, **800**, 38.

Grogin N. A., Kocevski D. D., Faber S. M., Ferguson H. C., Koekemoer A. M., Riess A. G., Acquaviva V., Alexander D. M., Almaini O., Ashby M. L. N., Barden M., Bell E. F., Bournaud F., Brown T. M., Caputi K. I., Casertano S., Cassata P., Castellano M., Challis P., Chary R.-R., Cheung E., Cirasuolo M., Conselice C. J., Roshan Cooray A., Croton D. J., Daddi E., Dahlen T., Davé R., de Mello D. F., Dekel A., Dickinson M., Dolch T., Donley J. L., Dunlop J. S., Dutton A. A., Elbaz D., Fazio G. G., Filippenko A. V., Finkelstein S. L., Fontana A., Gardner J. P., Garnavich P. M., Gawiser E., Giavalisco M., Grazian A., Guo Y., Hathi N. P., Häussler B., Hopkins P. F., Huang J.-S., Huang K.-H., Jha S. W., Kartaltepe J. S., Kirshner R. P., Koo D. C., Lai K., Lee K.-S., Li W., Lotz J. M., Lucas R. A., Madau P., McCarthy P. J., McGrath E. J., McIntosh D. H., McLure R. J., Mobasher B., Moustakas L. A., Mozena M., Nandra K., Newman J. A., Niemi S.-M., Noeske K. G., Papovich C. J., Pentericci L., Pope A., Primack J. R., Rajan A., Ravindranath S., Reddy N. A., Renzini A., Rix H.-W., Robaina A. R., Rodney S. A., Rosario D. J., Rosati P., Salimbeni S., Scarlata C., Siana B., Simard L., Smidt J., Somerville R. S., Spinrad H., Straughn A. N., Strolger L.-G., Telford O., Teplitz H. I., Trump J. R., van der Wel A., Villforth C., Wechsler R. H., Weiner B. J., Wiklind T., Wild V., Wilson G., Wuyts S., Yan H.-J., Yun M. S., 2011. ApJS, **197**, 35.

Gu M., Ho L. C., Peng C. Y., Huang S., 2013. ApJ, **773**, 34.

Guhathakurta P., Tyson J. A., Majewski S. R., 1990. ApJ, **357**, L9.

Guo Y., Ferguson H. C., Giavalisco M., Barro G., Willner S. P., Ashby M. L. N., Dahlen T., Donley J. L., Faber S. M., Fontana A., Galametz A., Grazian A., Huang K.-H., Kocevski D. D., Koekemoer A. M., Koo D. C., McGrath E. J., Peth M., Salvato M., Wuyts S., Castellano M., Cooray A. R., Dickinson M. E., Dunlop J. S., Fazio G. G., Gardner J. P., Gawiser E., Grogin N. A., Hathi N. P., Hsu L.-T., Lee K.-S., Lucas R. A., Mobasher B., Nandra K., Newman J. A., van der Wel A., 2013. ApJS, **207**, 24.

Hathi N. P., Malhotra S., Rhoads J. E., 2008. ApJ, **673**, 686.

Henriques B. M. B., White S. D. M., Lemson G., Thomas P. A., Guo Q., Marleau G.-D., Overzier R. A., 2012. MNRAS, **421**, 2904.

Ilbert O., Tresse L., Zucca E., Bardelli S., Arnouts S., Zamorani G., Pozzetti L., Bottini D., Garilli B., Le Brun V., Le Fèvre O., Maccagni D., Picat J.-P., Scaramella R., Scodeggio M., Vettolani G., Zanichelli A., Adami C., Arnaboldi M., Bolzonella M., Cappi A., Charlot S., Contini T., Foucaud S., Franzetti P., Gavignaud I., Guzzo L., Iovino A., McCracken H. J., Marano B., Marinoni C., Mathez G., Mazure A., Meneux B., Merighi R., Paltani S., Pello R., Pollo A., Radovich M., Bondi M., Bongiorno A., Busarello G., Ciliegi P., Lamareille F., Mellier Y., Merluzzi P., Ripepi V., Rizzo D., 2005. A&A, **439**, 863.

Illingworth G. D., Magee D., Oesch P. A., Bouwens R. J., Labbé I., Stiavelli M., van Dokkum P. G., Franx M., Trenti M., Carollo C. M., Gonzalez V., 2013. ApJS, **209**, 6.

Ishigaki M., Kawamata R., Ouchi M., Oguri M., Shimasaku K., Ono Y., 2015. ApJ, **799**, 12.

Ishigaki M., Kawamata R., Ouchi M., Oguri M., Shimasaku K., Ono Y., 2018. ApJ, **854**, 73.

Jaacks J., Choi J.-H., Nagamine K., Thompson R., Varghese S., 2012. MNRAS, **420**, 1606.

Jauzac M., Clément B., Limousin M., Richard J., Jullo E., Ebeling H., Atek H., Kneib J.-P., Knowles K., Natarajan P., Eckert D., Egami E., Massey R., Rexroth M., 2014. MNRAS, **443**, 1549.

Johnson T. L., Sharon K., Bayliss M. B., Gladders M. D., Coe D., Ebeling H., 2014. ApJ, **797**, 48.

Jullo E., Kneib J.-P., 2009. MNRAS, **395**, 1319.

Jullo E., Kneib J.-P., Limousin M., Elíasdóttir Á., Marshall P. J., Verdugo T., 2007. *New Journal of Physics*, **9**, 447.

Kawamata R., Ishigaki M., Shimasaku K., Oguri M., Ouchi M., 2015. ApJ, **804**, 103.

Kennicutt, Jr. R. C., 1998. ARA&A, **36**, 189.

Kneib J.-P., Natarajan P., 2011. A&A Rev., **19**, 47.

Kneib J.-P., 1993. *PhD thesis*, Ph. D. thesis, Université Paul Sabatier, Toulouse, (1993).

Koekemoer A. M., Faber S. M., Ferguson H. C., Grogin N. A., Kocevski D. D., Koo D. C., Lai K., Lotz J. M., Lucas R. A., McGrath E. J., Ogaz S., Rajan A., Riess A. G., Rodney S. A., Strolger L., Casertano S., Castellano M., Dahlen T., Dickinson M., Dolch T., Fontana A., Giavalisco M., Grazian A., Guo Y., Hathi N. P., Huang K.-H., van der Wel A., Yan H.-J., Acquaviva V., Alexander D. M., Almaini O., Ashby M. L. N., Barden M., Bell E. F., Bournaud F., Brown T. M., Caputi K. I., Cassata P., Challis P. J., Chary R.-R., Cheung E., Cirasuolo M., Conselice C. J., Roshan Cooray A., Croton D. J., Daddi E., Davé R., de Mello D. F., de Ravel L., Dekel A., Donley J. L., Dunlop J. S., Dutton A. A., Elbaz D., Fazio G. G., Filippenko A. V., Finkelstein S. L., Frazer C., Gardner J. P., Garnavich P. M., Gawiser E., Gruetzbauch R., Hartley W. G., Häussler B., Herrington J., Hopkins P. F., Huang J.-S., Jha S. W., Johnson A., Kartaltepe J. S., Khostovan A. A., Kirshner R. P., Lani C., Lee K.-S., Li W., Madau P., McCarthy P. J., McIntosh D. H., McLure R. J., McPartland C., Mobasher B., Moreira H., Mortlock A., Moustakas L. A., Mozena M., Nandra K., Newman J. A., Nielsen J. L., Niemi S., Noeske K. G., Papovich C. J., Pentericci L., Pope A., Primack J. R., Ravindranath S., Reddy N. A., Renzini A., Rix H.-W., Robaina A. R., Rosario D. J., Rosati P., Salimbeni S., Scarlata C., Siana B., Simard L., Smidt J., Snyder D., Somerville R. S., Spinrad H., Straughn A. N., Telford O., Teplitz H. I., Trump J. R., Vargas C., Villforth C., Wagner C. R., Wandro P., Wechsler R. H., Weiner B. J., Wiklind T., Wild V., Wilson G., Wuyts S., Yun M. S., 2011. ApJS, **197**, 36.

Labbé I., Bouwens R., Illingworth G. D., Franx M., 2006. ApJ, **649**, L67.

Labbé I., González V., Bouwens R. J., Illingworth G. D., Franx M., Trenti M., Oesch P. A., van Dokkum P. G., Stiavelli M., Carollo C. M., Kriek M., Magee D., 2010. ApJ, **716**, L103.

Laidler V. G., Papovich C., Grogin N. A., Idzi R., Dickinson M., Ferguson H. C., Hilbert B., Clubb K., Ravindranath S., 2007. PASP, **119**, 1325.

Laporte N., Streblyanska A., Kim S., Pelló R., Bauer F. E., Bina D., Brammer G., De Leo M. A., Infante L., Pérez-Fournon I., 2015. A&A, **575**, A92.

Laporte N., Infante L., Troncoso Iribarren P., Zheng W., Molino A., Bauer F. E., Bina D., Broadhurst T., Chilingarian I., Huang X., Garcia S., Kim S., Marques-Chaves R., Moustakas J., Pelló R., Pérez-Fournon I., Shu X., Streblyanska A., Zitrin A., 2016. ApJ, **820**, 98.

Livermore R. C., Finkelstein S. L., Lotz J. M., 2017. ApJ, **835**, 113.

Lotz J. M., Koekemoer A., Coe D., Grogin N., Capak P., Mack J., Anderson J., Avila R., Barker E. A., Borncamp D., Brammer G., Durbin M., Gunning H., Hilbert B., Jenkner H., Khandrika H., Levay Z., Lucas R. A., MacKenty J., Ogaz S., Porterfield B., Reid N., Robberto M., Royle P., Smith L. J., Storrie-Lombardi L. J., Sunnquist B., Surace J., Taylor D. C., Williams R., Bullock J., Dickinson M., Finkelstein S., Natarajan P., Richard J., Robertson B., Tumlinson J., Zitrin A., Flanagan K., Sembach K., Soifer B. T., Mountain M., 2017. ApJ, **837**, 97.

Lu Y., Mo H. J., Weinberg M. D., Katz N., 2011. MNRAS, **416**, 1949.

Lu Y., Wechsler R. H., Somerville R. S., Croton D., Porter L., Primack J., Behroozi P. S., Ferguson H. C., Koo D. C., Guo Y., Safarzadeh M., Finlator K., Castellano M., White C. E., Sommariva V., Moody C., 2014. ApJ, **795**, 123.

Madau P., Ferguson H. C., Dickinson M. E., Giavalisco M., Steidel C. C., Fruchter A., 1996. MNRAS, **283**, 1388.

Madau P., 1995. ApJ, **441**, 18.

McLeod D. J., McLure R. J., Dunlop J. S., 2016. MNRAS, **459**, 3812.

McLure R. J., Cirasuolo M., Dunlop J. S., Sekiguchi K., Almaini O., Foucaud S., Simpson C., Watson M. G., Hirst P., Page M. J., Smail I., 2006. MNRAS, **372**, 357.

McLure R. J., Dunlop J. S., Cirasuolo M., Koekemoer A. M., Sabbi E., Stark D. P., Targett T. A., Ellis R. S., 2010. MNRAS, **403**, 960.

McLure R. J., Dunlop J. S., de Ravel L., Cirasuolo M., Ellis R. S., Schenker M., Robertson B. E., Koekemoer A. M., Stark D. P., Bowler R. A. A., 2011. MNRAS, **418**, 2074.

McLure R. J., Dunlop J. S., Bowler R. A. A., Curtis-Lake E., Schenker M., Ellis R. S., Robertson B. E., Koekemoer A. M., Rogers A. B., Ono Y., Ouchi M., Charlot S., Wild V., Stark D. P., Furlanetto S. R., Cirasuolo M., Targett T. A., 2013. MNRAS, **432**, 2696.

Menci N., Merle A., Totzauer M., Schneider A., Grazian A., Castellano M., Sanchez N. G., 2017. ApJ, **836**, 61.

Merlin E., Fontana A., Ferguson H. C., Dunlop J. S., Elbaz D., Bourne N., Bruce V. A., Buitrago F., Castellano M., Schreiber C., Grazian A., McLure R. J., Okumura K., Shu X., Wang T., Amorín R., Boutsia K., Cappelluti N., Comastri A., Derriere S., Faber S. M., Santini P., 2015. A&A, **582**, A15.

Merlin E., Amorín R., Castellano M., Fontana A., Buitrago F., Dunlop J. S., Elbaz D., Boucaud A., Bourne N., Boutsia K., Brammer G., Bruce V. A., Capak P., Cappelluti N., Ciesla L., Comastri A., Cullen F., Derriere S., Faber S. M., Ferguson H. C., Giallongo E., Grazian A., Lotz J., Michałowski M. J., Paris D., Pentericci L., Pilo S., Santini P., Schreiber C., Shu X., Wang T., 2016. A&A, **590**, A30.

Merten J., Coe D., Dupke R., Massey R., Zitrin A., Cypriano E. S., Okabe N., Frye B., Braglia F. G., Jiménez-Teja Y., Benítez N., Broadhurst T., Rhodes J., Meneghetti M., Moustakas L. A., Sodré, Jr. L., Krick J., Bregman J. N., 2011. MNRAS, **417**, 333.

Meurer G. R., Heckman T. M., Leitherer C., Kinney A., Robert C., Garnett D. R., 1995. AJ, **110**, 2665.

Meurer G. R., Heckman T. M., Lehnert M. D., Leitherer C., Lowenthal J., 1997. AJ, **114**, 54.

Meurer G. R., Heckman T. M., Calzetti D., 1999. ApJ, **521**, 64.

Mobasher B., Dahlen T., Ferguson H. C., Acquaviva V., Barro G., Finkelstein S. L., Fontana A., Gruetzbauch R., Johnson S., Lu Y., Papovich C. J., Pforr J., Salvato

M., Somerville R. S., Wiklind T., Wuyts S., Ashby M. L. N., Bell E., Conselice C. J., Dickinson M. E., Faber S. M., Fazio G., Finlator K., Galametz A., Gawiser E., Giavalisco M., Grazian A., Grogin N. A., Guo Y., Hathi N., Kocevski D., Koekemoer A. M., Koo D. C., Newman J. A., Reddy N., Santini P., Wechsler R. H., 2015. ApJ, **808**, 101.

Oesch P. A., Bouwens R. J., Carollo C. M., Illingworth G. D., Trenti M., Stiavelli M., Magee D., Labbé I., Franx M., 2010. ApJ, **709**, L21.

Oesch P. A., Bouwens R. J., Illingworth G. D., Labbé I., Trenti M., Gonzalez V., Carollo C. M., Franx M., van Dokkum P. G., Magee D., 2012. ApJ, **745**, 110.

Oesch P. A., Bouwens R. J., Illingworth G. D., Labbé I., Franx M., van Dokkum P. G., Trenti M., Stiavelli M., Gonzalez V., Magee D., 2013. ApJ, **773**, 75.

Oesch P. A., Bouwens R. J., Illingworth G. D., Labbé I., Smit R., Franx M., van Dokkum P. G., Momcheva I., Ashby M. L. N., Fazio G. G., Huang J.-S., Willner S. P., Gonzalez V., Magee D., Trenti M., Brammer G. B., Skelton R. E., Spitler L. R., 2014. ApJ, **786**, 108.

Oesch P. A., Brammer G., van Dokkum P. G., Illingworth G. D., Bouwens R. J., Labbé I., Franx M., Momcheva I., Ashby M. L. N., Fazio G. G., Gonzalez V., Holden B., Magee D., Skelton R. E., Smit R., Spitler L. R., Trenti M., Willner S. P., 2016. ApJ, **819**, 129.

Oesch P. A., Bouwens R. J., Illingworth G. D., Labbé I., Stefanon M., 2018. ApJ, **855**, 105.

Oguri M., 2010. PASJ, **62**, 1017.

Oke J. B., Gunn J. E., 1983. ApJ, **266**, 713.

Ono Y., Ouchi M., Shimasaku K., Dunlop J., Farrah D., McLure R., Okamura S., 2010. ApJ, **724**, 1524.

Ono Y., Ouchi M., Curtis-Lake E., Schenker M. A., Ellis R. S., McLure R. J., Dunlop J. S., Robertson B. E., Koekemoer A. M., Bowler R. A. A., Rogers A. B., Schneider E., Charlot S., Stark D. P., Shimasaku K., Furlanetto S. R., Cirasuolo M., 2013. ApJ, **777**, 155.

Partridge R. B., Peebles P. J. E., 1967. ApJ, **147**, 868.

Peng C. Y., Ho L. C., Impey C. D., Rix H.-W., 2002. AJ, **124**, 266.

Planck Collaboration, Aghanim N., Akrami Y., Ashdown M., Aumont J., Baccigalupi C., Ballardini M., Banday A. J., Barreiro R. B., Bartolo N., Basak S., Battye R., Benabed K., Bernard J. P., Bersanelli M., Bielewicz P., Bock J. J., Bond J. R., Borrill J., Bouchet F. R., Boulanger F., Bucher M., Burigana C., Butler R. C., Calabrese E., Cardoso J. F., Carron J., Challinor A., Chiang H. C., Chluba J., Colombo L. P. L., Combet C., Contreras D., Crill B. P., Cuttaia F., de Bernardis P., de Zotti G., Delabrouille J., Delouis J. M., Di Valentino E., Diego J. M., Doré O., Douspis M., Ducout A., Dupac X., Dusini S., Efstathiou G., Elsner F., Enßlin T. A., Eriksen H. K., Fantaye Y., Farhang M., Fergusson J., Fernandez-Cobos R., Finelli F., Forastieri F., Frailis M., Franceschi E., Frolov A., Galeotta S., Galli S., Ganga K., Génova-Santos R. T., Gerbino M., Ghosh T., González-Nuevo J., Górski K. M., Gratton S., Gruppuso A., Gudmundsson J. E., Hamann J., Hand ley W., Herranz D., Hivon E., Huang Z., Jaffe A. H., Jones W. C., Karakci A., Keihänen E., Keskitalo R., Kiiveri K., Kim J., Kisner T. S., Knox L., Krachmalnicoff N., Kunz M., Kurki-Suonio H., Lagache G., Lamarre J. M., Lasenby A., Lattanzi M., Lawrence C. R., Le Jeune M., Lemos P., Lesgourgues J., Levrier F., Lewis A., Liguori M., Lilje P. B., Lilley M., Lindholm V., López-Caniego M., Lubin P. M., Ma Y. Z., Macías-Pérez J. F., Maggio G., Maino D., Mandolesi N., Mangilli A., Marcos-Caballero A., Maris M., Martin P. G., Martinelli M., Martínez-González E., Matarrese S., Mauri N., McEwen J. D., Meinhold P. R., Melchiorri A., Mennella A., Migliaccio M., Millea M., Mitra S., Miville-Deschênes M. A., Molinari D., Montier L., Morgante G., Moss A., Natoli P., Nørgaard-Nielsen H. U., Pagano L., Paoletti D., Partridge B., Patanchon G., Peiris H. V., Perrotta F., Pettorino V., Piacentini F., Polastri L., Polenta G., Puget J. L., Rachen J. P., Reinecke M., Remazeilles M., Renzi A., Rocha G., Rosset C., Roudier G., Rubiño-Martín J. A., Ruiz-Granados B., Salvati L., Sandri M., Savelainen M., Scott D., Shellard E. P. S., Sirignano C., Sirri G., Spencer L. D., Sunyaev R., Suur-Uski A. S., Tauber J. A., Tavagnacco D., Tenti M., Toffolatti L., Tomasi M., Trombetti T., Valenziano L., Valiviita J., Van Tent B., Vibert L., Vielva P., Villa F., Vittorio N., Wand elt B. D., Wehus I. K., White M., White S. D. M., Zacchei A., Zonca A., 2018. *arXiv e-prints*.

Postman M., Coe D., Benítez N., Bradley L., Broadhurst T., Donahue M., Ford H., Graur O., Graves G., Jouvel S., Koekemoer A., Lemze D., Medezinski E., Molino A., Moustakas L., Ogaz S., Riess A., Rodney S., Rosati P., Umetsu K., Zheng W., Zitrin A., Bartelmann M., Bouwens R., Czakon N., Golwala S., Host O., Infante L., Jha S., Jimenez-Teja Y., Kelson D., Lahav O., Lazkoz R., Maoz D., McCully C., Melchior P., Meneghetti M., Merten J., Moustakas J., Nonino

M., Patel B., Regös E., Sayers J., Seitz S., Van der Wel A., 2012. ApJS, **199**, 25.

Ravindranath S., Giavalisco M., Ferguson H. C., Conselice C., Katz N., Weinberg M., Lotz J., Dickinson M., Fall S. M., Mobasher B., Papovich C., 2006. ApJ, **652**, 963.

Reddy N., Dickinson M., Elbaz D., Morrison G., Giavalisco M., Ivison R., Papovich C., Scott D., Buat V., Burgarella D., Charmandaris V., Daddi E., Magdis G., Murphy E., Altieri B., Aussel H., Dannerbauer H., Dasyra K., Hwang H. S., Kartaltepe J., Leiton R., Magnelli B., Popesso P., 2012. ApJ, **744**, 154.

Robertson B. E., Ellis R. S., Dunlop J. S., McLure R. J., Stark D. P., 2010. Nature, **468**, 49.

Robertson B. E., Ellis R. S., Furlanetto S. R., Dunlop J. S., 2015. ApJ, **802**, L19.

Schaerer D., de Barros S., 2009. A&A, **502**, 423.

Schaerer D., de Barros S., 2010. A&A, **515**, A73.

Schaerer D., de Barros S., 2012. *The importance of nebular emission for SED modeling of distant star-forming galaxies*, In: *The Spectral Energy Distribution of Galaxies - SED 2011*, p. 20, eds Tuffs R. J., Popescu C. C.

Schechter P., 1976. ApJ, **203**, 297.

Schenker M. A., Robertson B. E., Ellis R. S., Ono Y., McLure R. J., Dunlop J. S., Koekemoer A., Bowler R. A. A., Ouchi M., Curtis-Lake E., Rogers A. B., Schneider E., Charlot S., Stark D. P., Furlanetto S. R., Cirasuolo M., 2013. ApJ, **768**, 196.

Schmidt K. B., Treu T., Trenti M., Bradley L. D., Kelly B. C., Oesch P. A., Holwerda B. W., Shull J. M., Stiavelli M., 2014. ApJ, **786**, 57.

Schmidt M., 1968. ApJ, **151**, 393.

Sersic J. L., 1968. *Atlas de Galaxias Australes.*

Shipley H. V., Lange-Vagle D., Marchesini D., Brammer G. B., Ferrarese L., Stefanon M., Kado-Fong E., Whitaker K. E., Oesch P. A., Feinstein A. D., Labbé I., Lundgren B., Martis N., Muzzin A., Nedkova K., Skelton R., van der Wel A., 2018. ApJS, **235**, 14.

Sobral D., Matthee J., Darvish B., Schaerer D., Mobasher B., Röttgering H. J. A., Santos S., Hemmati S., 2015. ApJ, **808(2)**, 139.

Somerville R. S., Hopkins P. F., Cox T. J., Robertson B. E., Hernquist L., 2008. MNRAS, **391**, 481.

Song M., Finkelstein S. L., Ashby M. L. N., Grazian A., Lu Y., Papovich C., Salmon B., Somerville R. S., Dickinson M., Duncan K., Faber S. M., Fazio G. G., Ferguson H. C., Fontana A., Guo Y., Hathi N., Lee S.-K., Merlin E., Willner S. P., 2016. ApJ, **825**, 5.

Spergel D. N., Bean R., Doré O., Nolta M. R., Bennett C. L., Dunkley J., Hinshaw G., Jarosik N., Komatsu E., Page L., Peiris H. V., Verde L., Halpern M., Hill R. S., Kogut A., Limon M., Meyer S. S., Odegard N., Tucker G. S., Weiland J. L., Wollack E., Wright E. L., 2007. ApJS, **170**, 377.

Stanway E. R., Bunker A. J., McMahon R. G., 2003. MNRAS, **342**, 439.

Stanway E. R., Bremer M. N., Lehnert M. D., Eldridge J. J., 2008. MNRAS, **384**, 348.

Stark D. P., Bunker A. J., Ellis R. S., Eyles L. P., Lacy M., 2007. ApJ, **659**, 84.

Stark D. P., Ellis R. S., Bunker A., Bundy K., Targett T., Benson A., Lacy M., 2009. ApJ, **697**, 1493.

Stark D. P., Schenker M. A., Ellis R., Robertson B., McLure R., Dunlop J., 2013. ApJ, **763**, 129.

Steidel C. C., Hamilton D., 1992. AJ, **104**, 941.

Steidel C. C., Giavalisco M., Dickinson M., Adelberger K. L., 1996a. AJ, **112**, 352.

Steidel C. C., Giavalisco M., Pettini M., Dickinson M., Adelberger K. L., 1996b. ApJ, **462**, L17.

Steidel C. C., Giavalisco M., Pettini M., Dickinson M., Adelberger K. L., 1996c. ApJ, **462**, L17.

Thompson R. I., 2003. ApJ, **596**, 748.

Trenti M., Stiavelli M., 2008. ApJ, **676**, 767.

Trenti M., Bradley L. D., Stiavelli M., Oesch P., Treu T., Bouwens R. J., Shull J. M., MacKenty J. W., Carollo C. M., Illingworth G. D., 2011. ApJ, **727**, L39.

Villanueva-Domingo P., Gnedin N. Y., Mena O., 2018. ApJ, **852**, 139.

Vogelsberger M., Nelson D., Pillepich A., Shen X., Marinacci F., Springel V., Pakmor R., Tacchella S., Weinberger R., Torrey P., Hernquist L., 2019. *arXiv e-prints*.

Weinmann S. M., Neistein E., Dekel A., 2011. MNRAS, **417**, 2737.

Wilkins S. M., Bunker A. J., Stanway E., Lorenzoni S., Caruana J., 2011. MNRAS, **417**, 717.

Williams R. E., Blacker B., Dickinson M., Dixon W. V. D., Ferguson H. C., Fruchter A. S., Giavalisco M., Gilliland R. L., Heyer I., Katsanis R., Levay Z., Lucas R. A., McElroy D. B., Petro L., Postman M., Adorf H.-M., Hook R., 1996. AJ, **112**, 1335.

Williams R. E., Baum S., Bergeron L. E., Bernstein N., Blacker B. S., Boyle B. J., Brown T. M., Carollo C. M., Casertano S., Covarrubias R., de Mello D. F., Dickinson M. E., Espey B. R., Ferguson H. C., Fruchter A., Gardner J. P., Gonnella A., Hayes J., Hewett P. C., Heyer I., Hook R., Irwin M., Jones D., Kaiser M. E., Levay Z., Lubenow A., Lucas R. A., Mack J., MacKenty J. W., Madau P., Makidon R. B., Martin C. L., Mazzuca L., Mutchler M., Norris R. P., Perriello B., Phillips M. M., Postman M., Royle P., Sahu K., Savaglio S., Sherwin A., Smith T. E., Stiavelli M., Suntzeff N. B., Teplitz H. I., van der Marel R. P., Walker A. R., Weymann R. J., Wiggs M. S., Williger G. M., Wilson J., Zacharias N., Zurek D. R., 2000. AJ, **120**, 2735.

Zheng W., Postman M., Zitrin A., Moustakas J., Shu X., Jouvel S., Høst O., Molino A., Bradley L., Coe D., Moustakas L. A., Carrasco M., Ford H., Benítez N., Lauer T. R., Seitz S., Bouwens R., Koekemoer A., Medezinski E., Bartelmann M., Broadhurst T., Donahue M., Grillo C., Infante L., Jha S. W., Kelson D. D., Lahav O., Lemze D., Melchior P., Meneghetti M., Merten J., Nonino M., Ogaz S., Rosati P., Umetsu K., van der Wel A., 2012. Nature, **489**, 406.

Zitrin A., Meneghetti M., Umetsu K., Broadhurst T., Bartelmann M., Bouwens R., Bradley L., Carrasco M., Coe D., Ford H., Kelson D., Koekemoer A. M., Medezinski E., Moustakas J., Moustakas L. A., Nonino M., Postman M., Rosati P., Seidel G., Seitz S., Sendra I., Shu X., Vega J., Zheng W., 2013. ApJ, **762**, L30.

Zitrin A., Zheng W., Broadhurst T., Moustakas J., Lam D., Shu X., Huang X., Diego J. M., Ford H., Lim J., Bauer F. E., Infante L., Kelson D. D., Molino A., 2014. ApJ, **793**, L12.

Zwicky F., 1933. *Helvetica Physica Acta*, **6**, 110.